Applied Catalysis B: Environmental 206 (2017) 556–588

Contents lists available at ScienceDirect

Applied Catalysis B: Environmental

journal homepage: www.elsevier.com/locate/apcatb

Review Article

Graphitic C_3N_4 based noble-metal-free photocatalyst systems: A review

Dilshad Masih, Yuanyu Ma, Sohrab Rohani*

Department of Chemical and Biochemical Engineering, University of Western Ontario, London, Ontario, Canada

ARTICLE INFO

Article history:
Received 8 December 2016
Received in revised form 5 January 2017
Accepted 10 January 2017
Available online 26 January 2017

Keywords:
g-C_3N_4
Noble-metal-free
Nanomaterials
Photocatalysis

ABSTRACT

Many reviews are written on this interesting visible light active polymeric semiconductor material, the graphitic carbon nitride (g-C_3N_4). Yet the ever-expanding volume of the ongoing research on this materials has inspired us to compile this review, especially on its nanoscale architectures of noble-metal-free photocatalyst systems. From the viewpoint of sustainable development, an economical photocatalyst which is made up of abundant elements e. g. C and N has a good prospect for large scale applications. Stability of the photocatalyst material under the experimental conditions is essential for its repeated usage, however, many semiconductors sought for visible-light-driven reaction, particularly sulfides and nitrides are in a compromising situation. However, g-C_3N_4 has high chemical- and photo-stability besides its high activity under visible light irradiation. Furthermore, solely semiconductor materials have the intrinsic problem of recombination of photogenerated electron-hole pairs. To overcome this problem, loading of the semiconductor with a co-catalyst, usually a noble metal is a common practice for transfer of electron and thus avoiding the recombination. Development of a noble-metal-free photocatalyst systems is essentially important for sustainable applications. Hence, the construction of a hybrid composite structure is interesting in the separation of photogenerated charge carriers. Besides diminishing the rate of recombination, the heterostructures are constructed for harnessing a wider spectrum of sunlight. In contrast to bulk semiconductors, their nanoscale counterpart offers a larger number of active sites along with interesting electrical and optical properties. Importantly, construction of extensive junctions between nanomaterials greatly enhance the separation of charges and consequently improve their photocatalytic efficiency. Usually, the stability of materials is compromised with the reduction of size to nano level, however, g-C_3N_4 and its nanomaterials demonstrate exceptional recycling in photocatalytic testing. One of the most important interests in controlling nanoparticle size, shape and composition is to develop noble-metal-free photocatalyst systems. Here in this review, we have compiled research on all the various applications of noble-metal-free nanoscale photocatalyst systems based on g-C_3N_4. By the end, we conclude the research topic and put forward future perspectives for further developments in designing practicable photocatalyst systems.

Contents

* Corresponding author.
E-mail addresses: dilshadmasih@yahoo.com (D. Masih), srohani@uwo.ca (S. Rohani).

http://dx.doi.org/10.1016/j.apcatb.2017.01.061

1. Introduction

Graphitic carbon nitride (g-C_3N_4) is a polymeric layered material, structurally analogous to graphene [1]. In contrast to the pure C constituent of graphene, g-C_3N_4 is composed of C and N with some impurity of H, which all are abundant raw materials. Semiconducting properties of g-C_3N_4 also drastically distinguish it from graphene. The band gap of bulk g-C_3N_4 is ~2.7 eV, and it is a medium band gap semiconductor. Pertaining to its yellow color the optical absorption of g-C_3N_4 lies around 460 nm making it an interesting material for harvesting solar energy. Furthermore, the thermal and chemical stability of g-C_3N_4 in an aqueous suspension phase and under photocatalytic reaction condition makes it an interesting material [2].

This g-C_3N_4 is regarded as the oldest synthetic polymer first reported by Berzelius and Liebig in the year 1834 and named as 'melon' [1]. A flow sheet diagram is provided in Fig. 1 showing a summary of historic developments in understanding g-C_3N_4 and its application in photocatalysis. In 1922, Franklin found the empirical composition of 'melon' to be C_3N_4. Next, Pauling and Sturdivant derived tri-s-triazine type structure of C_3N_4 in the year 1937. By 1940 it was known that this material 'melon' has a graphite structure as reported by Redemann and Lucas [2]. Photocatalysis received enormous attention after Fujishima and Honda reported photolysis of water on TiO_2 in 1972 [3]. A wide variety of materials, mainly inorganic semiconductors were evaluated for photocatalytic application. However, nobody paid attention to making use of g-C_3N_4 in photocatalysis until Wang et al. first reported in 2009 [4].

Since the pioneering photocatalytic studies by Wang et al. in 2009 [4,5], g-C_3N_4 has become the focus of research on photocatalytic materials. Lately, a comprehensive review article is presented by Ong et al. [2]. Besides some other relevant reviews, feature articles and perspectives on g-C_3N_4 are important to read [6–15]. A record of yearly publications on photoactive applications of g-C_3N_4 elucidates the magnitude of research interest in this material (Fig. 2). Wang et al. put forward this polymeric material essentially as a metal-free visible-light active photocatalyst [4]. An efficient overall water splitting ability using solar energy is considered a Holy Grail of photocatalysis. Once this is realized, a commercial scale production of green and renewable chemical fuel will become a viable process. There are several requirements for developing an efficient photocatalyst for water splitting under solar irradiation: (1) good properties for harvesting solar light, (2) a band gap of suitable energy with valence and conduction band appropriately positioned for the desired reactions, and (3) good stability of the photocatalyst under experimental conditions. In principal, this thermally and chemically stable polymeric semiconductor g-C_3N_4 fulfills the band gap requirement for harvesting solar energy with a band structure suitable for both water oxidation and reduction reactions. At present, there are a lot many ongoing efforts on the development of efficient and sustainable noble-metal-free photocatalyst systems.

Environmental pollution and sustainable supply of greener energy are two of the main global challenges of the current era. Considering the Sun as an almost inexhaustible and primary source of energy, lately, there are many interests in developing semiconductor materials for harvesting solar energy to produce cleaner fuels and resolve the environmental issues. Lately, visible light active photocatalysts are getting enormous attention for applications to environment and energy sectors. Production of green and renewable energy carrier, H_2 from water, reduction of CO_2, synthesis of fine chemicals and remediation of environmental pollutants are the main explored reactions.

Polymeric g-C_3N_4 is a metal-free medium band gap *p*-type semiconductor with a reliable chemical and thermal stability. Furthermore, its versatile optical and electronic properties with a band gap ~2.7 eV make it an attractive candidate for harvesting solar energy. TiO_2 is the most popular photocatalyst material due to its robust reactivity, availability, and chemical stability, however, it absorbs only UV light that limits its application [16]. Among various photoactive applications, g-C_3N_4 have been widely employed as a visible light active photocatalyst for degradation of organic pollutants, H_2/O_2 evolution half reactions, complete water splitting, reduction of CO_2 and organic synthesis (Fig. 3). The semiconductor, g-C_3N_4 is composed of earth-abundant elements. However, the noble/precious metals which are mainly loaded as a co-catalyst e. g. Pt, to avoid the recombination of photogenerated electron-hole pairs are the costly constituents. A photocatalyst system is comprised of a semiconductor or a junction of semiconductors along with a sensitizer and/or a co-catalyst. Here in this review we will discuss g-C_3N_4 based photocatalyst systems which are altogether free from noble-metals and important for sustainable development.

Visible-light-driven photocatalyst systems are interesting for efficient harvesting of the solar spectrum. The band gap of pure g-C_3N_4 (~2.7 eV) corresponds to absorption of blue-light up to 450 nm, hence inactive towards major part of the solar radiation comping to the earth. Furthermore, this relatively large band gap of the pure g-C_3N_4 over-energizes the ideally required potential (1.23 eV) for the most desired water splitting reaction. Wang et al. applied various methods of doping [17,18], copolymerization [19,20], and dye sensitization [21] to modify g-C_3N_4 for an optimum utilization of solar spectrum for a specific photoactive reaction. Next, the development of a noble-metal-free or precious-metal-free photocatalyst system is important for making it sustainable.

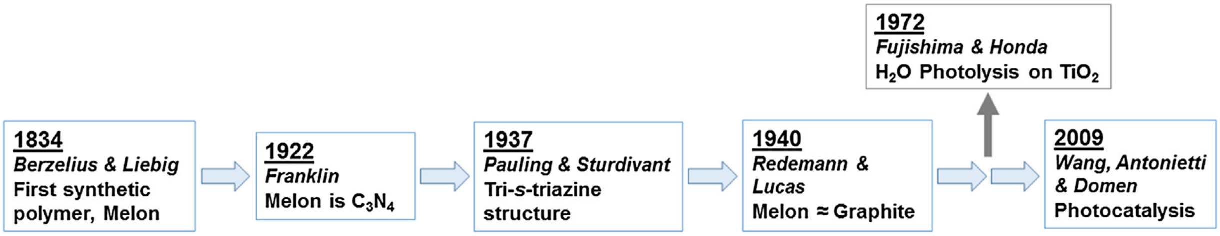

Fig. 1. Historic developments on understanding g-C_3N_4 and photocatalysis over it.

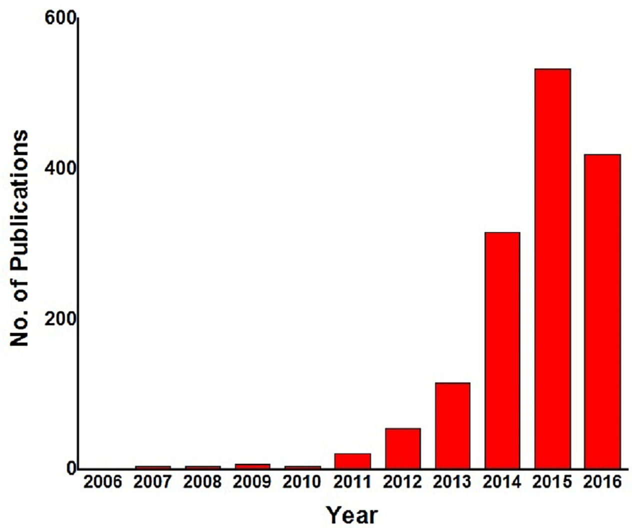

Fig. 2. Year-by-year publications on photoactive properties of g-C_3N_4. Data from the Web of Science.

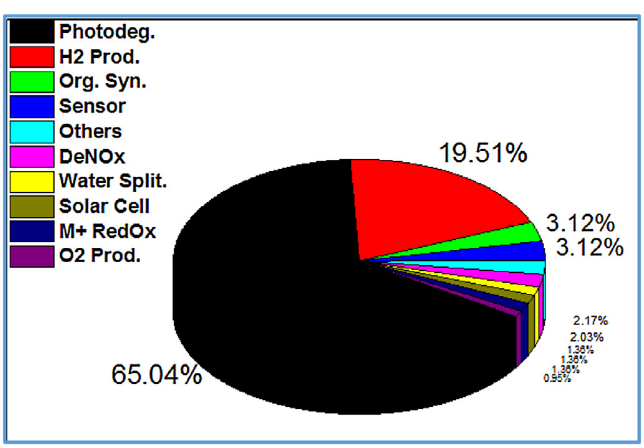

Fig. 3. Pie chart distribution of various photoactive applications of g-C_3N_4.

Intrinsically, g-C_3N_4 is a layered material in which C_3N_4 sheets are connected by Van der Waal forces. Hence single and a few layer sheets of g-C_3N_4 are obtained upon the breakdown of these weak forces. Nanoscale materials offer unique regime of catalysis in between homogeneous catalysis and heterogeneous catalysis. However, the stability of nanoscale materials is challenging and needs attention for the important recycling of the material. Furthermore, nanomaterials based photocatalysts are more effective with the greatly enhanced availability of active surface sites [22]. Wang et al. have done extensive research on the development of g-C_3N_4 based nanoscale materials for photocatalytic applications e. g. H_2 evolution [22–28], O_2 evolution [29,30], and CO_2 reduction [31].

In this review, we are summarizing g-C_3N_4 based nanomaterials for all the various noble-metal-free applications in photocatalysis.

2. Photocatalysis over noble-metal-free g-C_3N_4 based nanomaterials

2.1. Overall water splitting

To mimic the natural photosynthesis, a semiconductor-based photocatalytic water splitting into H_2 and O_2 has been the focus of many researchers. However, the bottleneck of overall water splitting is the formation of oxygen–oxygen bond that requires the transfer of four electrons in a single step. The separation of photocatalytically cogenerated H_2 and O_2 is yet another challenging task. There are only a few studies on overall water splitting over g-C_3N_4 based noble-metal-free photocatalyst systems and summarized here. However, a vast majority of researchers have studied the half reaction of water splitting, mainly for H_2 evolution only.

A composite structure of NiFe-layered double hydroxide and g-C_3N_4 was investigated for overall water splitting under visible light irradiation [32]. Remarkably, a high rate of production of H_2 (744 μmol h^{-1} g^{-1}) and O_2 (443 μmol h^{-1} g^{-1}) was found over optimized composite. A synergy in the composite of two layered materials as indicated by tuned-in band gap, quenching of photoluminescence (PL), and prolonged lifetime of charge carrier was assigned for this enhanced photocatalytic activity. However, the rate of evolution of both H_2 and O_2 was severely deteriorated with a repeated usage of the photocatalyst.

A composite structure comprising of carbon nanodots and g-C_3N_4 was fabricated by Liu et al. as a metal-free photocatalyst for overall water splitting [33]. An optimized nanocomposite demonstrated impressive performance and stability with a quantum efficiency of 16% under visible-light irradiation. The rate of H_2 (8.4 μmol h^{-1}) and O_2 (4.1 μmol h^{-1}) evolution was maintained in 200 runs of recycling use of the photocatalyst over 200 days. Contrary to the conventional belief of one-step four-electron process for photocatalytic water splitting, this study put forward a new hypothesis of two-step process; photocatalysis (two-electron) and chemical catalysis (two-electron). Carbon nanodots were recognized for extending the absorption of visible light in the nanocomposite and assigned a center for the chemical catalysis step.

2.2. H_2 evolution reaction

In contrast to overall water splitting, H_2 and/or O_2 evolution half reactions at the expense of a sacrificial reagent are widely studied via photocatalysis. An efficient production of H_2 gas from water over a suspended photocatalyst material using solar energy is considered an ideal reaction for the supply of green and renewable energy. Antonietti and Domen groups did the pioneering work on g-C_3N_4 towards the development of a stable, inexpensive and abundant photocatalyst material [4]. And since then, more than 150 papers on H_2 and/or O_2 evolution half reactions over g-C_3N_4

based materials have appeared in the journals. Only a couple of publications reported on both of the H_2 and O_2 evolution half reactions, under varying conditions. In fewer than 10 papers, research was attempted on O_2 evolution half reaction only. In comparison to overall water splitting and O_2 evolution half reaction, extensive research (more than 130 papers) has been carried out on H_2 evolution half reaction.

2.2.1. Metal-free photocatalyst system

From the beginning of the research on g-C_3N_4 as a photocatalyst, it became known that this material has a potential for H_2 evolution from water. The rate of H_2 evolution was varying from batch to batch, in the range of 0.1–4 μmol h^{-1} under visible-light irradiation [4]. Under the experimental conditions, even a mesoporous structure of g-C_3N_4 remained inefficient for H_2 evolution from water, the rate of H_2 evolution reaction drastically increased with the loading of Pt onto g-C_3N_4.

To extend the research on sustainable metal-free g-C_3N_4 photocatalyst, Cui et al. synthesized various conjugated nanostructures via solution processing [34]. Physicochemical properties and bandgap size of the carbon nitride nanostructures were dependent upon synthesis conditions. Nanobelts with a moderate specific surface area (30 m^2 g^{-1}) and the band gap of 1.78 eV demonstrated the highest stability and rate of H_2 evolution (6.1 μmol h^{-1}) under visible light irradiation, amongst all the various conjugated carbon nitrides. Suryawanshi et al. investigated on the nanocomposite with nanotubes to understand the electronic and morphological changes in g-C_3N_4 [35]. Various concentrations of multiwall carbon nanotubes (MWCNT) were mixed with g-C_3N_4 for the synthesis of an all-carbon photocatalyst. A twofold increase in H_2 evolution activity was observed under visible-light irradiation for the optimized metal-free photocatalyst system, 0.5% MWCNT/g-C_3N_4.

Lately, further progress towards the development of a metal-free photocatalyst was made by functionalization of g-C_3N_4 with electron acceptor carbon nanoparticles derived from zeolitic imidazolate framework (ZIF). A metal-free bifunctional catalyst system of carbon nanoparticles decorated on g-C_3N_4 was reported recently by He et al. [36]. Precursors for both the carbon nanoparticles and the g-C_3N_4 were mixed together and treated in one-step at 650 °C under N_2 flow to obtain the composite photocatalyst. Carbon nanoparticle of about 60 nm size was in-situ derived from a zeolitic imidazolate framework during the thermal conversion of melamine into g-C_3N_4. A TEM image of the composite with encircled carbon nanoparticles grown on sheets of g-C_3N_4 is provided in Fig. 4A. Before photocatalytic testing, the composite was washed with HCl solution to remove the residual Zn, and to make sure it is an all-carbon system. In comparison with the pristine and Pt loaded g-C_3N_4, all the composites with various concentrations of carbon nanoparticles displayed better activity towards H_2 evolution (Fig. 4B). The rate of H_2 evolution over 1 wt.% carbon nanoparticle functionalized g-C_3N_4 (32.6 μmol h^{-1}) was 36 times higher than that of the pure g-C_3N_4 (0.9 μmol h^{-1}), under visible-light irradiation. Interestingly, under the experimental conditions this metal-free carbon composite performed 2.8 times better than 3% Pt loaded g-C_3N_4 (11.6 μmol h^{-1}). The PL spectra provided in the inset in Fig. 4B exhibited a small quenching upon loading of g-C_3N_4 with Pt metal. However, a significant decrease in the PL intensity was observed for the optimized composite with C nanoparticles, suggesting an improved efficiency for separation of charge carriers. This trend of the charge carrier dynamics was consistent with the photocatalytic activity. Besides the photocatalytic reduction of water, this g-C_3N_4 composite with C nanoparticles was functioning as an efficient electrocatalyst for hydrogen evolution reaction. Fang et al. prepared carbon dots (C-dots) modified g-C_3N_4 hybrid by a novel strategy using C-dots and dicyandiamide as starting materials [37]. The rate of H_2 evolution over the pure g-C_3N_4 was

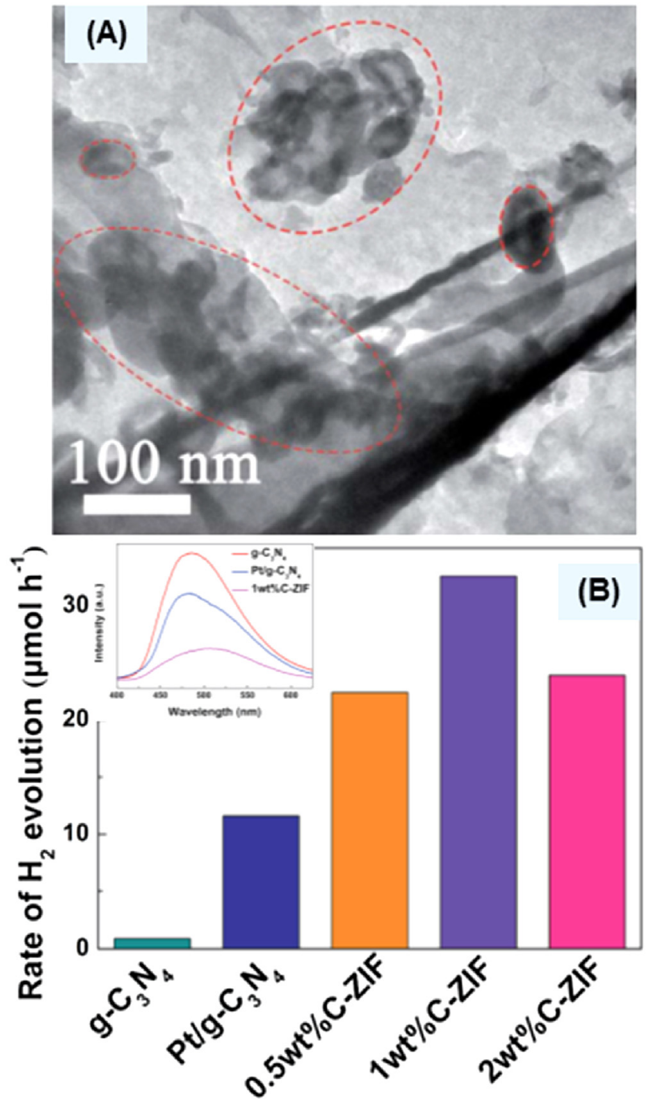

Fig. 4. (A) TEM image of ZIF derived C nanoparticles grown on g-C_3N_4 sheets, and (B) Photocatalytic H_2 evolution rate of pure g-C_3N_4, 3 wt.% Pt/g-C_3N_4 and g-C_3N_4 composites with different amounts of ZIF derived C nanoparticles. Inset in (B) provides PL spectra.

91 μmol g^{-1} h^{-1} that sharply increased by a factor of 2.4 times (218 μmol g^{-1} h^{-1}) for the sample optimized with C-dots.

A simple process of acid treatment and sonication for the synthesis of few-layer nanosheets of g-C_3N_4 was put forward by Ma et al. [38]. In comparison with the bulk g-C_3N_4, the absorption edge showed a blue shift and the corresponding emission peak also shifted towards lower wavelength. Hence, the band gap was decreased. For the visible-light-induced H_2 evolution reaction, the results showed a comparable activity and rate (110.68 μmol g^{-1} h^{-1}) over a few-layer nanosheet of g-C_3N_4. A further modification of nanosheets was made by Liang et al. through the development of a holey structure [39]. Thermal treatment of bulk g-C_3N_4 under NH_3 atmosphere converted it to holey nanosheets with self-modified carbon vacancies, and an enlarged band gap (2.95 eV). As expected for a porous structure, specific surface area of the holey nanosheets (196 m^2 g^{-1}) was higher than non-porous nanosheets (179 m^2 g^{-1}). In comparison to the photocatalysis over bulk g-C_3N_4, a good improvement in photocatalytic efficiency was demonstrated by the porous nanosheets. The rate

of H_2 production from water under visible-light irradiation was 20 times faster on the holey nanosheets of g-C_3N_4 (82.9 μmol h^{-1}) compared to that of the bulk material (4.2 μmol h^{-1}). Furthermore, the holey nanosheets were stable under the experimental conditions.

Xia et al. explored the spectral and electronic synergistic effects by integrating g-C_3N_4 nanosheets with carbon quantum dots (CQDs) via a one-step hydrothermal method [40]. XRD patterns and TEM images showed the presence of CQDs in the composite structure. DR-UV–vis spectra demonstrated extended absorption in the visible-to-near infrared (NIR) region. Besides H_2 evolution under UV and UV–vis light irradiations, this half-reaction by a metal-free photocatalyst was also realized under NIR-light for the first time. For a composite photocatalyst with optimized (10%) CQDs, the rate of H_2 production was slow, 6.76 μmol g^{-1} h^{-1} upon irradiation with a laser beam of NIR-light (808 nm). The rate of H_2 production was increased to 50.5 μmol g^{-1} h^{-1} under visible-light, and it was found the highest upon illumination with UV–vis, to 219.5 μmol g^{-1} h^{-1}.

2.2.2. Binary hybrid system

While many researchers were focusing on modifications of g-C_3N_4 and loading it with noble metal nanoparticles for H_2 evolution from water, Hou et al. prepared layered nanojunctions of MoS_2 and mesoporous g-C_3N_4 for noble-metal-free catalysis [41]. The rate of H_2 production over the nanojunction increased first until loading 0.2 wt.% MoS_2 and then decreased with further loadings. On the other hand, for the Pt-loaded sample, the rate of H_2 production kept on increasing from 0.1 wt.% to 2.0 wt.%. For intermediate loadings of 0.5 wt.% of MoS_2 (20.6 μmol h^{-1}) and Pt (4.8 μmol h^{-1}) loaded samples, the rate of H_2 evolution on the noble-metal-free system was more than 4 times higher. The optimized system showed an apparent quantum yield of 2.1% at 420 nm. However, the cyclic runs for H_2 production over the optimized MoS_2 system showed deactivation. Yu et al. loaded nanoparticles of $Ni(OH)_2$ onto g-C_3N_4 by a simple precipitation method [42]. TEM analysis showed that some nanoparticles of $Ni(OH)_2$ in the range of 10–20 nm were deposited on the surface of g-C_3N_4 nanosheets. Visible-light-driven photocatalytic production of H_2 was enhanced with this low-cost $Ni(OH)_2$ co-catalyst. Among various forms of nickel, $Ni(OH)_2$ co-catalyst was found better for H_2 production, in comparison with pure Ni and NiO. Under the experimental conditions, the rate of H_2 production over the optimal $Ni(OH)_2$/g-C_3N_4 (7.6 μmol h^{-1}) photocatalyst was approaching that of a noble metal loaded g-C_3N_4 (8.2 μmol h^{-1}). For repeated use of photocatalyst, a decrease in the activity was noticed after the first run and then was maintained for H_2 production. The apparent quantum efficiency was 1.1% and after the second cycle, the H_2 production remained stable over the $Ni(OH)_2$-modified g-C_3N_4 system. The noble-metal-free system of 10–20 nm $Ni(OH)_2$ precipitated on g-C_3N_4 nanosheets showed comparable photocatalytic activity with Pt/g-C_3N_4.

In an effort to develop an understanding of a noble-metal-free photocatalyst, Bi et al. studied the changes in the surface band bending upon composite formation of g-C_3N_4 with Ni metal via a solvothermal method [43]. About 30 nm metallic Ni nanoparticle were loaded on g-C_3N_4 and characterized by XRD and TEM analysis. Mott-Schottky plots showed a deeper band bending for the optimized Ni/g-C_3N_4 composite, and demonstrated a higher efficiency in the separation of photogenerated electron-hole pairs. Under the experimental conditions, pure g-C_3N_4 without Ni co-catalyst was almost inactive. The rate of H_2 production steadily increased with Ni metal loading onto g-C_3N_4 and reached a maximum of 8.41 μmol h^{-1} for about 10% Ni/g-C_3N_4 (under full light) which was comparable with that of the one modified with $Ni(OH)_2$, 7.6 μmol h^{-1} (under visible light) [42]. Many researchers investigated Ni as a noble-metal alternate in learning from nature, as nickel is found in the hydrogenase enzymes that regulate hydrogen in biological systems.

Lately, Kong et al. reported light-assisted rapid preparation of Ni-based robust photocatalyst, a magnetic composite of Ni/g-C_3N_4 [44]. Uniformly dispersed metallic Ni nanoparticles with diameters of 30–80 nm were photodeposited on the surface of g-C_3N_4. Under full light, an extremely high rate of H_2 evolution, 4318 μmol g^{-1} h^{-1} was obtained for the optimized system containing 7.4% Ni. The apparent quantum yield of H_2 at 400 nm was 2.01%, and the catalyst was durable after 48 h of recycling tests.

Another sulfur-based low-cost material, WS_2 was decorated onto g-C_3N_4 as a noble-metal-free co-catalyst. Akple et al. constructed a heterojunction between WS_2 loaded onto g-C_3N_4 through a gas-solid reaction under an inert atmosphere [45]. The composite structure was prepared by a gas-solid reaction under an inert atmosphere. The crystalline structures of both semiconductors in the composite were identified with TEM analysis (Fig. 5A & B) and XRD patterns (Fig. 5C). Under the experimental conditions, both g-C_3N_4 and WS_2 were individually inactive for the photocatalytic H_2 evolution from water. The rate of H_2 production over the optimized composite with a very small loading of WS_2 (nominal 0.01 wt.%) onto g-C_3N_4 was 101 μmol g^{-1} h^{-1} under visible-light irradiation, which was even better than that of the sample with the same amount of Pt co-catalyst (72 μmol g^{-1} h^{-1}). As shown in Fig. 5D, the cyclic photocatalysis runs demonstrated a stable production of H_2 over this noble-metal-free WS_2/g-C_3N_4. Furthermore, the photoelectrochemical measurements confirmed the stability of the binary hybrid system.

Towards the development of a noble-metal-free photocatalyst for H_2 generation from water, Chen et al. designed a novel strategy to fabricate homogeneously distributed nanoparticles of C and N co-doped TiO_2 on ultrathin nanosheets of g-C_3N_4 by a simple one-pot solvothermal route [46]. As learned from the synergistic combination TiO_2/g-C_3N_4, a superior photocatalytic ability was expected for this composite pertaining to its improved optical, electrical and physicochemical properties. Under visible light illumination, the nanocomposite exhibited superior H_2 generation comparing with the individual components of the heterojunction. The rate of H_2 evolution over the optimized composite with 3 wt.% C and N co-doped TiO_2 reached to 39.2 μmol g^{-1} h^{-1} which was 10.9 and 21.3 times higher than the sole C,N-TiO_2 nanoparticles, and pure g-C_3N_4 nanosheets, respectively. Furthermore, the optimized catalyst remained stable in recycling tests. Liu et al. hydrothermally hybridized well dispersed 10–20 nm CdZnS with g-C_3N_4 nanosheets for visible-light-driven H_2 evolution and degradation of organic pollutants [47]. Over the optimized composite, the rate of H_2 evolution from water was 208 μmol h^{-1} that showed a slight decrease in cyclic runs. Recently, ∼25 nm size CoP nanoparticle modified g-C_3N_4 nanostructures were prepared by Yi et al. using a simple grinding of the precursors [48]. Visible-light-driven rate of H_2 generation over this noble-metal-free 0.25 wt.% CoP loaded g-C_3N_4 reached to ∼475 μmol g^{-1} h^{-1}. The rate was ∼131 times higher than that of the pure g-C_3N_4 and even better comparing with the optimized Pt/g-C_3N_4. The noble-metal-free nanostructure demonstrated no loss of H_2 production activity in repeated runs.

Recently, Wang et al. prepared heterostructure of μ-oxo dimeric iron(III) porphyrin, $(FeTPP)_2O$ and g-C_3N_4 through a solution phase chemical reaction [49]. Sole $(FeTTP)_2O$ and its physical mixture with g-C_3N_4 were not active for photocatalytic H_2 production. Formation of heterostructure was sought to be important for a photocatalytic activity where $(FeTTP)_2O$ acted not just as a photosensitizer, but also helped with separation of charges. Full UV–vis light irradiation stimulated the $(FeTTP)_2O$/g-C_3N_4 photocatalyst to produce H_2 at a rate of about 40 μmol h^{-1}. While under visible-light irradiation, the rate of H_2 production was 11 μmol h^{-1} [49].

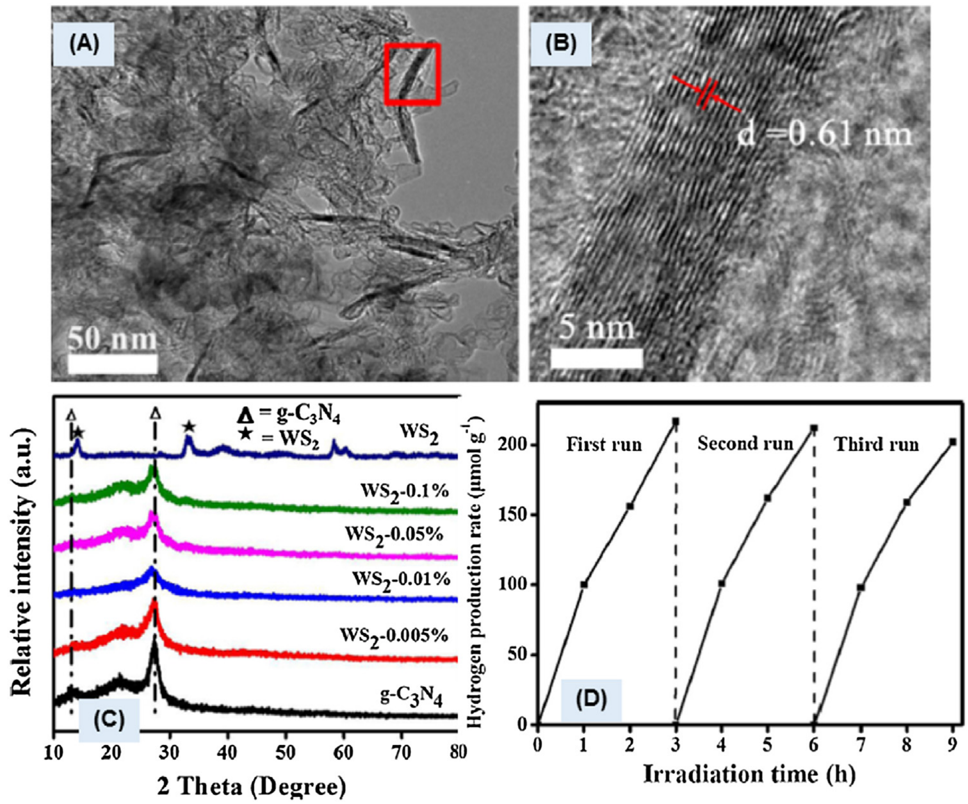

Fig. 5. (A) TEM and (B) HR-TEM image of g-C_3N_4/WS_2 (0.01%) sample, (C) XRD patterns of g-C_3N_4, WS_2 and various samples of g-C_3N_4/WS_2, and (D) Cyclic runs for the photocatalytic H_2 production on g-C_3N_4/WS_2 (0.01%) sample.
Reproduced with permission from the Ref. [45]. Copyright (2015) Elsevier.

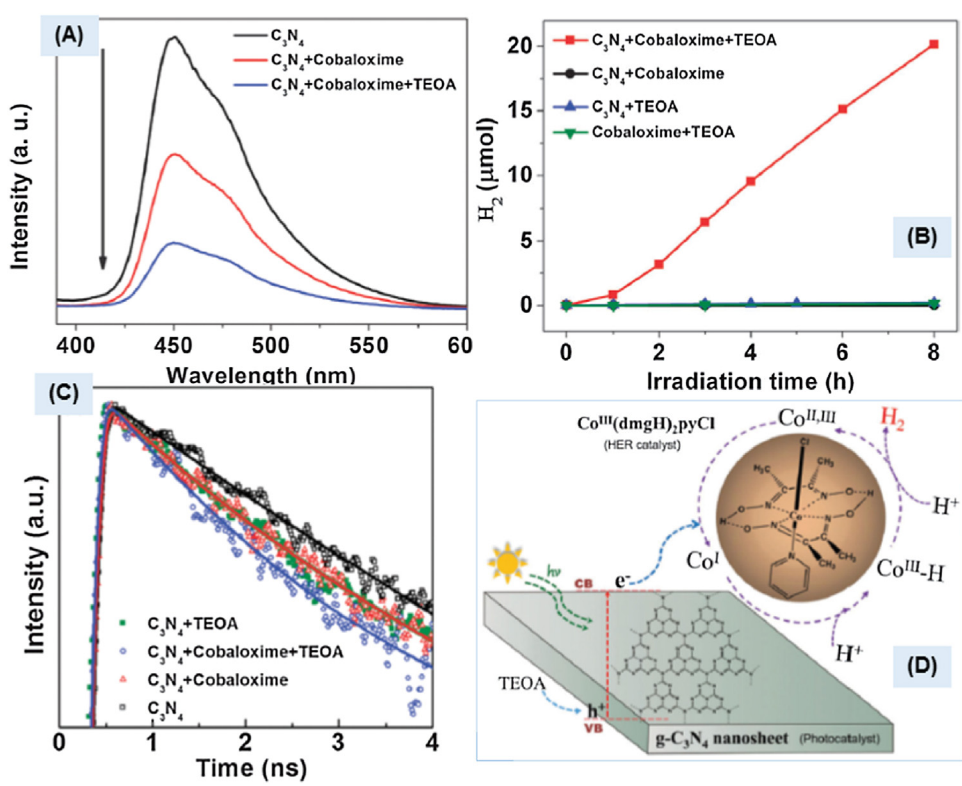

Fig. 6. (A) Steady-state PL spectra for different components in H_2O, the concentrations are the same as those in photocatalytic reaction, (B) Photocatalytic H_2 evolution amount obtained from water reduction in the presence of different components, (C) Transient fluorescence decay for different components in H_2O, the concentrations are the same as those in photocatalytic reaction, and (D) Schematic illustration of the photocatalytic process for H_2 evolution.
Reproduced with permission from the Ref. [51]. Copyright (2013) Royal Society of Chemistry.

Next, studies on Ni-dimethylglyoxime (dmgH) based molecular catalyst combined with g-C_3N_4 were continued by Cao et al. in order to prepare a noble-metal-free photocatalyst system [50]. The particle size of the sub-microwires of Ni-dmgH was smaller (~230 nm) when grown in the presence of g-C_3N_4. A steady rate of H_2 generation (1.18 μmol h^{-1}) was found for the optimal coupling of Ni-dmgH with g-C_3N_4 and maintained in cycling tests. Abnormally a prolonged induction time period was noticed for the onset of the photocatalytic H_2 evolution reaction over Ni-dmgH/g-C_3N_4. Cobaloxime was also explored by Cao et al. as an organometallic co-catalyst to fabricate an economical and a noble-metal-free photocatalyst system [51]. The importance of the sacrificial reagent, triethanolamine (TEOA) was established by the spectroscopic investigations and observed in the photocatalytic production of H_2. Quenching of the PL intensity was noted with the construction of a hybrid system of cobaloxime and g-C_3N_4, and further enhanced in the presence of TEOA (Fig. 6A). None of the combinations was active except for g-C_3N_4 loaded with cobaloxime and in the presence of TEOA (Fig. 6B). After an early induction period, the steady-state rate of H_2 production was about 2.6 μmol h^{-1}. Transient fluorescence studies revealed the separation and transfer of photoexcited electrons from g-C_3N_4 to cobaloxime in the presence of TEOA (Fig. 6C). A schematic illustration of the role of cobaloxime and TEOA in the separation of photogenerated charges on g-C_3N_4 nanosheet, and thus the production of H_2 is given in Fig. 6D.

Hong et al. prepared a noble-metal-free, NiS loaded g-C_3N_4 binary system by a simple hydrothermal method [52]. Mesoporous g-C_3N_4 was prepared using SiO_2 nanosphere (12 nm) as a template and loaded with NiS nanoparticles by hydrothermal method. The optimized composite photocatalyst, ca. 1.25 wt.% NiS/g-C_3N_4 showed an efficient rate of H_2 evolution (48.2 μmol h^{-1}) upon visible-light irradiation which is around 70% that of the Pt/C_3N_4 under the same experimental conditions. Time course of H_2 production over NiS/g-C_3N_4 in the recycle study showed a gradual decrease in the activity. The apparent quantum efficiency of 1.9% was recorded at 440 nm.

Recently, Lu et al. also worked on the same system, NiS/g-C_3N_4, in an effort to develop a visible-light-driven noble-metal-free photocatalyst [53]. In contrast to the mesoporous g-C_3N_4 used by Hong et al. [52], a liquid phase exfoliated g-C_3N_4 nanosheets were decorated with the co-catalyst NiS by precipitation and hydrothermal method. The thickness of the exfoliated nanosheets of g-C_3N_4 was ~3 nm. In the composite structure, nanoparticles of NiS are well anchored onto g-C_3N_4 nanosheets as shown in the TEM images (Fig. 7A & B). As noticed in other Ni-based photocatalyst systems, an initial induction time period for the photocatalytic H_2 evolution reactions over NiS/g-C_3N_4 under visible-light irradiation. The production of H_2 over nanosheet g-C_3N_4 loaded with noble-metal-free co-catalyst, NiS was 25% less efficient than that with Pt (5.6 μmol h^{-1}). However, under the optimized experimental conditions when equating with Pt loaded g-C_3N_4 photocatalyst, the working efficiency of NiS/nanosheet g-C_3N_4 (75%) was better than NiS/mesoporous g-C_3N_4 (70%) composite. The rate of photocatalytic H_2 production was correlated with the wavelength it was exposed to, and the behavior was parallel to the optical absorbance properties (Fig. 7C). Comparing with bulk NiS/bulk g-C_3N_4 (1.6 μmol h^{-1}) composite, about 2.6 times enhancement in the rate of H_2 evolution was observed over NiS/nanosheet g-C_3N_4 (4.2 μmol h^{-1}). A relationship of bulk and nanosheet structure with the photocatalytic performance is illustrated in the schematic (Fig. 7D).

Raziq et al. synthesized B-doped g-C_3N_4 nanosheets and fabricated their composite with a nanocrystalline anatase TiO_2 [54]. TEM images showed that nanocrystalline TiO_2 with 5 nm diameter was well-dispersed on the surface of B-doped g-C_3N_4. All the various photocatalytic applications of the nanocomposite, TiO_2/B-doped g-C_3N_4 in H_2 evolution, CO_2 reduction and degradation of environmental pollutants exhibited rather high activities compared to those of bare g-C_3N_4, under visible-light irradiation. In this co-catalyst-free system, B-induced surface state near the valence band top was suggested to trap holes and hence enhance the separation of charges. Under the experimental conditions, the photocatalytic H_2 production over bare g-C_3N_4 (0.52 μmol h^{-1}) was negligible. The rate of H_2 evolution increased 21 times with B-doping of the g-C_3N_4 (11 μmol h^{-1}). Comparing with bare g-C_3N_4, a very high 29 times enhancement of H_2 production was observed for the optimized nanocomposite of TiO_2/B-doped g-C_3N_4 (15 μmol h^{-1}). Though the overall rate of H_2 evolution over TiO_2/B-doped g-C_3N_4 was not good amongst similar TiO_2 based composite systems, this nanocomposite demonstrated a relatively great increase in efficiency when comparing with pristine g-C_3N_4.

A visible-light active, highly efficient and stable composite of $Cd_{0.5}Zn_{0.5}S$ nanoparticles of smaller than 100 nm and g-C_3N_4 was prepared by the solvothermal method [55]. Without any co-catalyst, the hybrid heterojunction $Cd_{0.5}Zn_{0.5}S$/g-C_3N_4 photocatalyst demonstrated improved rate of H_2 production of 20.8 mL h^{-1} as compared with 13.6 mL h^{-1} that of the pure $Cd_{0.5}Zn_{0.5}S$. For the optimized system, the photocatalytic activity was maintained by over 95% in the cyclic production of H_2. In an effort to prepare a noble-metal-free photocatalyst, Liu et al. fabricated composites of $Mn_{0.8}Cd_{0.2}S$ and g-C_3N_4 nanosheets by a facile hydrothermal method [56]. TEM analysis depicted 50 nm nanoparticles of multi-metal sulfide well-dispersed on the surface of g-C_3N_4. Under visible-light irradiation, the rate of H_2 production over pure $Mn_{0.8}Cd_{0.2}S$ was 1.2 mmol h^{-1} g^{-1} that increased about 3.4 times after formation of its composite, $Mn_{0.8}Cd_{0.2}S$/g-C_3N_4 (4.0 mmol h^{-1} g^{-1}). Cyclic runs for photocatalytic H_2 production over the optimized composite demonstrated its good stability under experimental conditions. Research on Cd-based sulfide composites of g-C_3N_4 was continued by Liu et al., and a mesoporous g-C_3N_4 was obtained by using a hard-template loaded with $CdLa_2S_4$ nanoparticles via a hydrothermal method [57]. TEM analysis showed an intimate interfacial contact between 50 nm spherical nanoparticles $CdLa_2S_4$ and nanosheets of g-C_3N_4. For the optimized composite of $CdLa_2S_4$/g-C_3N_4, the rate of H_2 evolution reach to 5.98 mmol h^{-1} g^{-1} under visible light irradiation, which was about 7.7 times higher than pure $CdLa_2S_4$ (0.77 mmol h^{-1} g^{-1}). The apparent quantum efficiency of the optimized heterojunction was 7.1% at 420 nm.

Besides Cd-based sulfide materials, Liu et al. also reported on the noble-metal-free fabrication of g-C_3N_4 composite with another bimetallic sulfide via a facile hydrothermal method [58]. Hexagonal $ZnIn_2S_4$ was chosen for it has a layered structure similar to g-C_3N_4. Sheet-on-sheet nanocomposites of $ZnIn_2S_4$/g-C_3N_4 were prepared with various compositions, and optimal content of g-C_3N_4 was 40 wt.% for an efficient photocatalytic activity. The thickness of $ZnIn_2S_4$ sheets was about 10 nm. A gradual increase in photocatalytic activity was observed with increasing mass ratio of g-C_3N_4 onto $ZnIn_2S_4$ that started to decrease beyond 40 wt.% loading. An enhanced photocatalytic activity of the optimized nanocomposite was ascribed to efficient separation and transfer of charges at the interface between $ZnIn_2S_4$ and g-C_3N_4 rather than physicochemical properties. Under visible-light irradiation, the rate of H_2 production over pure $ZnIn_2S_4$ was 500 μmol h^{-1} g^{-1} that increased about 1.91 times upon formation of its nanocomposite with g-C_3N_4 (953.5 μmol h^{-1} g^{-1}). Cyclic photocatalytic runs demonstrated a stable production of H_2 over $ZnIn_2S_4$/g-C_3N_4 under visible-light illumination. However, comparing with $ZnIn_2S_4$/g-C_3N_4 the composites of Cd-based S materials with g-C_3N_4 were more efficient for the photocatalytic production of H_2. Interestingly, around the same time period Zhang et al. also reported on photocatalytic activity

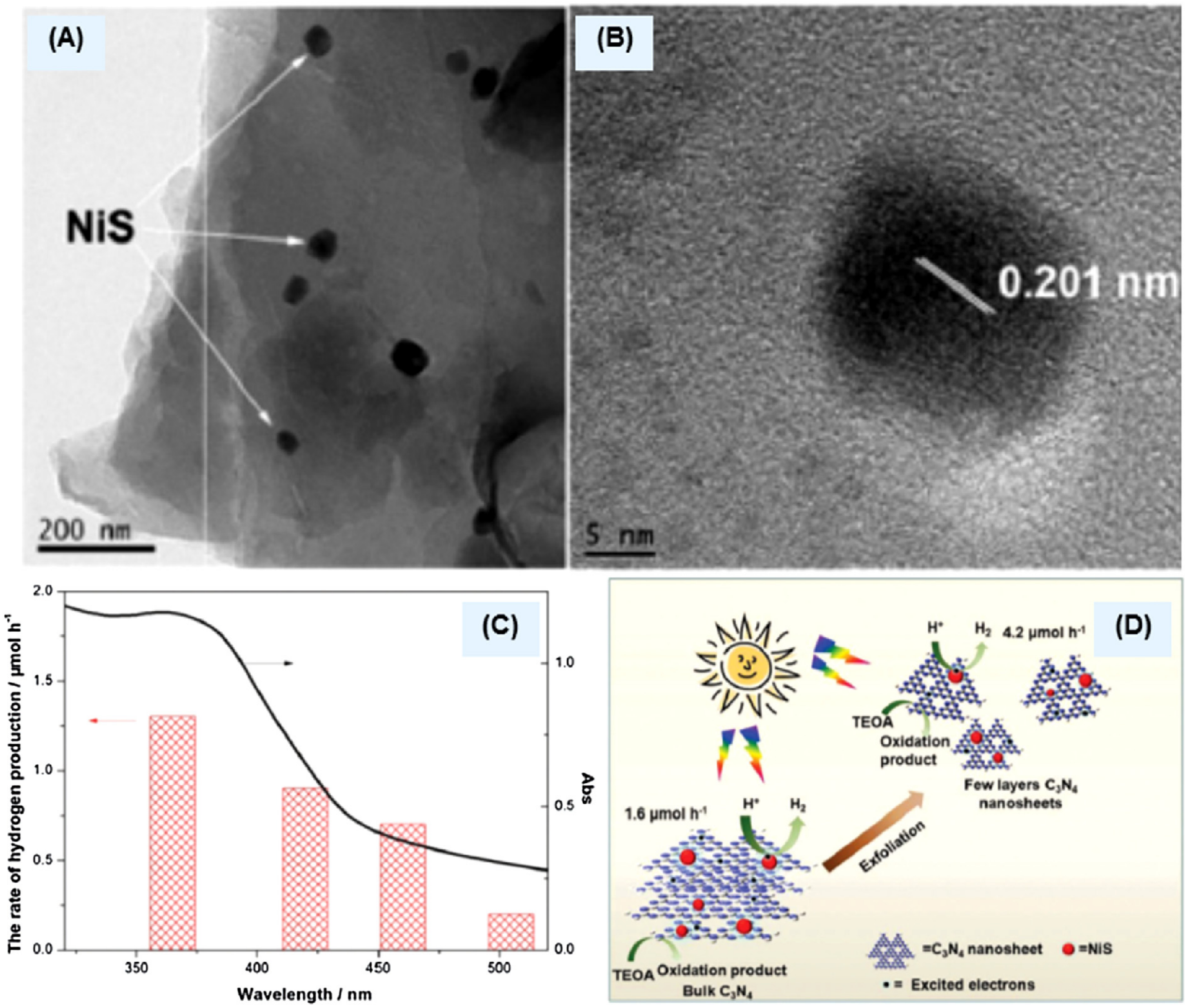

Fig. 7. (A) TEM and (B) HR-TEM image of g-C_3N_4/NiS sample, (C) Dependence of photocatalytic hydrogen production rate on the wavelengths and optical spectrum of the g-C_3N_4/NiS-1.0 sample, and (D) Schematic illustration of the visible light photocatalytic performance of NiS loaded on to bulk g-C_3N_4 and nanosheets of g-C_3N_4. Reproduced with permission from the Ref. [53]. Copyright (2015) Royal Society of Chemistry.

of sheet-on-sheet heterostructure of $ZnIn_2S_4$/g-C_3N_4 with various compositions [59]. TEM images of the heterostructure showed that 4–9 nm thick sheets of $ZnIn_2S_4$ were vertically grown onto the nanosheets of g-C_3N_4 and built a hierarchical structure. Similar to the method adopted by Liu et al. [58], $ZnIn_2S_4$ nanosheets were in-situ grown onto g-C_3N_4 nanosheets through a facile hydrothermal route. Contrary to the composite compositions studied by Liu et al. [58], when $ZnIn_2S_4$ was fixed while loading of g-C_3N_4 was varied from 0 to 50 wt.%, here in this study g-C_3N_4 was taken as a reference material and modified with various amounts of $ZnIn_2S_4$, 0–20 wt.%. Under visible-light irradiation, the H_2 production rate for the optimized photocatalyst system with 15 wt.% $ZnIn_2S_4$ loaded onto g-C_3N_4 was 14.1 μmol h^{-1} which was very low compared to the one reported by Liu et al. (953.5 μmol h^{-1} g^{-1}) [58]. On the other hand, under the experimental conditions a relative improvement in the optimized photocatalytic system against the reference material $ZnIn_2S_4$ was reported at nearly 4 times and 1.91 times by Zhang et al. [59] and Liu et al. [58], respectively. Recycling photocatalytic tests demonstrated good stability for the production of H_2 over $ZnIn_2S_4$/g-C_3N_4 under visible-light irradiation. Regarding the enhancement of photocatalytic activity, in addition to the extended absorption of light by the composite structure of nanosheets, it was mainly attributed to efficient separation and transfer of charges at the interface between $ZnIn_2S_4$ and g-C_3N_4. The optimum $ZnIn_2S_4$/g-C_3N_4 ratios found for photocatalytic H_2 production were quite different for both the research groups, specifically at 60/40 and at 15/85 by Liu et al. [58] and Zhang et al. [59], respectively.

In the search for an economically viable photocatalyst material, a noble-metal-free heterojunction of ZnS and g-C_3N_4 was constructed by Suyana et al. using a one-pot co-pyrolysis synthesis protocol [60]. TEM studies indicated 4–7 nm size ZnS nanoparticles in the composite. Transient spectroscopic and photocurrent measurements along with PL spectra revealed a reduction in recombination of charges in the ZnS/g-C_3N_4 composite. Under visible-light irradiation, an overall rate of H_2 production over the optimized composite 14 wt.% ZnS/g-C_3N_4 (871 μmol g^{-1} h^{-1}) was only about 25% higher than pure g-C_3N_4 (670 μmol g^{-1} h^{-1}). The heterojunction was active in dye degradation and organic synthesis too.

2.2.3. Ternary and complex hybrid system

A g-C_3N_4 based complex system comprising of earth-abundant elements, nickel, thiourea, and trimethylamine was in-situ constructed during the photocatalytic process [197]. This complex but low-cost photocatalyst system was highly efficient in the production of H_2 from water reduction. Under the solar light, the rate of H_2 production over this complex system was 51 μmol h^{-1}, and that

was comparable with Pt co-catalyst loaded g-C_3N_4 (59 μmol h^{-1}). Amongst other transition metal (Fe, Cu, and Co) based complex systems, only Co based photocatalyst showed some activity, but less than half that of the Ni comprising catalyst.

A ternary nanocomposite of mesoporous g-C_3N_4, multi-walled carbon nanotubes (MWCNT), and a metal sulfide co-catalyst was prepared by Zhong et al. via sol-gel followed directing precipitation [61]. At first, a nanocomposite of 40–60 nm diameter MWCNT was constructed with mesoporous g-C_3N_4 which was prepared with SiO_2 (12 nm) hard template. Three sulfides of different transition metals (Cu, Co, and Ni) were investigated as a co-catalysts to replace the noble metal, Pt. TEM images showed nicely formed ternary hybrid structure, and other characterizations illustrated accordingly favorable optical, and electronic properties. Among the nanocomposites with the same co-catalyst loadings (3 wt.%), the one with NiS demonstrated the best photocatalytic activity under visible-light irradiation. TEM studies showed that 5–20 nm size fine nanoparticles of NiS were strongly coupled with the surface of the flakes of mesoporous g-C_3N_4. The average rate of H_2 production over the nanocomposite with NiS co-catalyst reached 378 μmol g^{-1} h^{-1}, and that was 1.37 times and 12.2 times higher than with CoS and CuS co-catalysts, respectively. The amount of loading for the best performing NiS co-catalyst was optimized at 1 wt.%, and the corresponding rate of H_2 production reached to 521 μmol g^{-1} h^{-1} which was 148 times higher than that for the mpg-C_3N_4/MWCNT. A significant loss of H_2 production activity was observed in the second run. However photocatalytic activity in later cycle did not decrease drastically, and H_2 production became stable after three cycles. In search of a noble-metal-free photocatalyst, Yuan et al. loaded NiS co-catalyst onto heterojunction of CdS nanorods and g-C_3N_4 nanosheets via two-step wet chemistry method [62]. In-situ grown CdS nanorods of about 10 nm diameter and 100 nm length were uniformly distributed on the surface of g-C_3N_4 nanosheets. The size of NiS nanoparticles was ranging from 10 to 40 nm and HR-TEM exhibited clear lattice fringes of NiS and CdS on g-C_3N_4 nanosheets. The average rate of H_2 evolution under visible-light was increasing with the amount of the co-catalyst, and the optimized loading of NiS was 9 wt.%. Over the optimized nanocomposite, the rate of H_2 production reached to 2563 μmol g^{-1} h^{-1} that was 1582 times higher comparing with pure g-C_3N_4. In the repeated time courses for photocatalytic H_2 evolution, the decrease in activity was prominent after the first run and maintained in the next cycles.

Instead of a single co-catalyst, Wen et al. loaded dual co-catalyst comprising of NiS and carbon black onto g-C_3N_4 nanosheets to develop a noble-metal-free photocatalyst system [63]. A heterojunction was prepared from 30 to 60 nm sized NiS (1.5%) deposited on the surface of g-C_3N_4 and further decorated with 20–30 nm carbon black (0.5%) nanoparticles. The optimized ternary photocatalyst system exhibited a very high rate of H_2 evolution, 992 μmol g^{-1} h^{-1} which was higher than that of the binary composites, and with 3 wt.% Pt co-catalyst photocatalyst. This ternary composite showed a gradual loss of photoactivity in repeated cycles, typical of sulfide materials. Similarly, acetylene black decorated with $Ni(OH)_2$ was found a robust dual co-catalyst for an efficient photocatalytic activity of g-C_3N_4 under visible-light [64]. The nanoparticle of 20–50 nm acetylene black formed a chain-like structure on g-C_3N_4 and the composite was decorated with in-situ grown $Ni(OH)_2$ nanoparticles. The photocatalytic H_2 production efficiency of pure g-C_3N_4 (0.75 μmol g^{-1} h^{-1}) was increased with the loading of acetylene black (2.4 μmol g^{-1} h^{-1}). However, with loading a well-known $Ni(OH)_2$ co-catalyst for H_2 evolution reaction, a 100 fold increase in activity was observed comparing with pure g-C_3N_4. Next, a drastic increase in photocatalytic activity was observed when $Ni(OH)_2$ decorated acetylene black was used as a dual co-catalyst. The rate of H_2 production over this ternary nanocomposite reached to 240 μmol g^{-1} h^{-1} with a 320 times increase in comparison with pristine g-C_3N_4. These studies demonstrated an important strategy of combining nano-carbons with other earth-abundant co-catalysts as replacement of noble metal materials.

For the development of a noble-metal-free photocatalyst, Mori et al. made use of two different types of graphitic carbon nitrides, bulk g-C_3N_4 and delaminated nanostructured g-C_3N_4 in understanding the effect of the nanostructure [65]. They designed a ternary composite with Ni complex and a visible-light-responsive organic dye, thiazole orange (TO; band gap 1.84 eV). For the nanostructured g-C_3N_4, the BET specific surface area (148 m^2 g^{-1}) and pore volume (0.43 cm^3 g^{-1}) were about 15 and 10 times, respectively large than those of the bulk g-C_3N_4 and found effective in enhancing photocatalytic properties. The amounts of loadings of the active site of molecular level Ni co-catalyst species and the photosensitizer TO were optimized for H_2 production from aqueous solution and remained stable during the photocatalytic reaction. Ni K-edge X-ray absorption fine structure spectroscopy and TEM studies on both fresh and used materials demonstrated mononuclear species of Ni co-catalyst that remained stable during photocatalysis. Hence, molecular species of Ni, rather than the colloidal form, was responsible for the photocatalytic reaction. Over the bulk g-C_3N_4 based optimized system the rate of H_2 production was about 1.7 μmol h^{-1} that increased more than three times upon changing it to nanoporous g-C_3N_4 (about 5.8 μmol h^{-1}) with a high specific surface area and porosity.

A facile thermal process was developed by Pany et al. for one-step N and S incorporation into TiO_2 and fabrication of its nanocomposite with g-C_3N_4 [66]. Nanoparticles of around 20 nm were observed in the TEM images consistent with the crystallite size calculated from XRD pattern by using Scherrer formula. This known synergistic combination of TiO_2/g-C_3N_4 was made more effective with the introduction of dopants, N and S. Furthermore, small crystallite size, phase pure anatase, and a high specific surface area were found effective for enhanced visible light absorption and separation of charges. In this complex system, the leftover of sulfate from the titania precursor was incorporated onto the N,S-TiO_2/g-C_3N_4 heterojunction and acted as a co-catalyst. For the optimized N,S-TiO_2/g-C_3N_4 system, the rate of photocatalytic H_2 production reached to 317 μmol h^{-1}, which was 2.5 times higher than pure g-C_3N_4. In comparison with simple TiO_2/g-C_3N_4 [67] (52.71 μmol h^{-1}) heterojunction, the overall rate of H_2 evolution was higher for this complex system, N,S-TiO_2/g-C_3N_4 (317 μmol h^{-1}). Furthermore, the N,S-TiO_2/g-C_3N_4 complex system demonstrated stable performance during repeated usage for H_2 evolution reaction.

Another TiO_2-based complex system was investigated by Jiang et al. towards the development of the noble-metal-free system [68]. A novel ternary composite of TiO_2–In_2O_3 with g-C_3N_4 was synthesized by a solvothermal method. The nanoparticles of TiO_2–In_2O_3 were densely and uniformly distributed on the surface of g-C_3N_4. As observed under TEM, the average diameter of the TiO_2/In_2O_3 nanoparticles loaded onto g-C_3N_4 was around 12 nm (Fig. 8A). BET specific surface area of the ternary composite reached to 90 m^2 g^{-1}. Photocatalytic H_2 evolution activity of pure and hybrid materials is depicted in Fig. 8B. An enhanced photocatalytic activity by the ternary composite was attributed to a low rate of recombination along with a high specific surface area. Under visible-light illumination from LED, the rate of H_2 production was 8.6 μmol h^{-1} that was higher than binary hybrids, and 48 times higher than that of the pure g-C_3N_4.

A complex system of g-C_3N_4 co-sensitized with two dyes namely Eosin Y (EY) and Rose Bengal (RB), and loaded with in-situ grown $Co(OH)_2$ nanoparticle was developed for H_2 evolution under

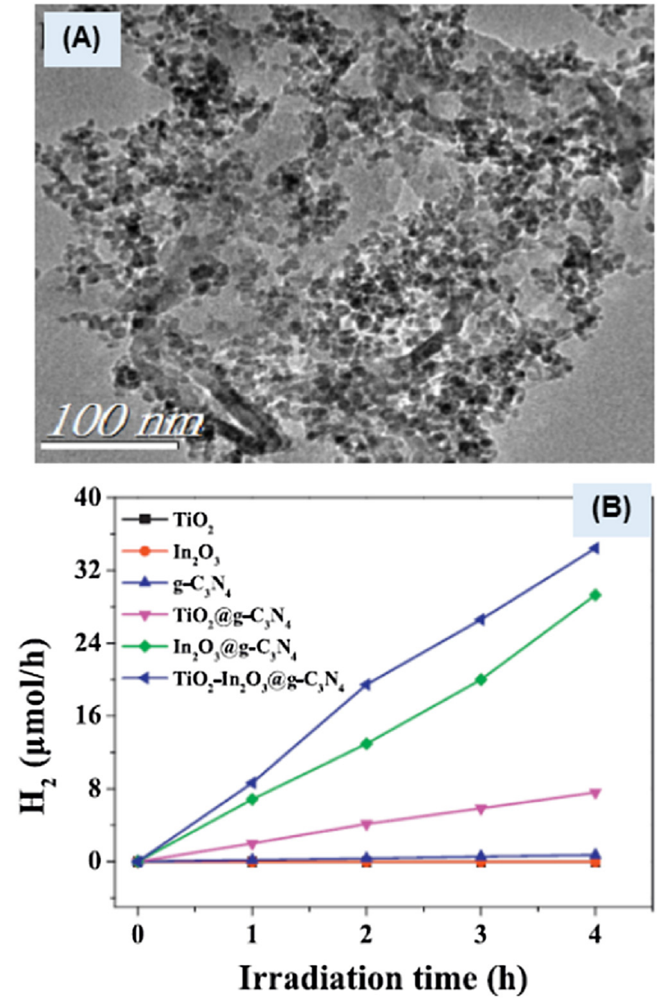

Fig. 8. (A) TEM image of TiO_2-In_2O_3 nanoparticles decorated on g-C_3N_4, and (B) Photocatalytic H_2 evolution activity of pure materials, binary composites, and ternary composite.
Reproduced with permission from the Ref. [68]. Copyright (2015) Elsevier.

visible-light irradiation [69]. The average size of $Co(OH)_2$ nanoparticles in TEM image was 3 nm and in good agreement with the one calculated from the line width analysis of the diffraction peak using Scherrer equation. Absorption of the visible light was extended from 430 nm to 600 nm with the co-sensitization of a binary system, $Co(OH)_2$/g-C_3N_4. Under the reaction conditions, only a trace amount of H_2 was produced over $Co(OH)_2$/g-C_3N_4. Essentially no H_2 evolution was observed over the catalyst systems composed of dyes and g-C_3N_4 without $Co(OH)_2$ co-catalyst loading. With a synergistic effect of co-catalyst and sensitizers, an optimized rate of H_2 evolution (143.9 μmol h^{-1}) was obtained for the 30 wt.% Co loaded g-C_3N_4 co-sensitized with EY to RB molar ratio at unity, and operating at pH 9. Stable performance in repeated runs of H_2 evolution reaction and a profile of constant photocurrent ascribed sustainable use of this noble-metal-free system. In contrast to the approach of co-sensitization with two dyes, Hao et al. used only Eosin Y for photosensitization of g-C_3N_4 and modulated the selective transfer of photogenerated electrons on differently exposed facets of binary metal (Co and Mo) sulfide [70]. The $Co_xMo_{1-x}S_2$/g-C_3N_4 composite was prepared via a facile solvothermal method and the dye photosensitizer was added into the aqueous reaction mixture and used for H_2 evolution reaction. The binary metal sulfide coupled with g-C_3N_4 comprised of irregular nanoparticles of 50 nm to 200 nm aggregates. In comparison with a 30%Co/g-C_3N_4 ratio for an optimum photoactivity, a high amount of co-catalyst at 70%$Co_xMo_{1-x}S_2$/g-C_3N_4 was needed for the best H_2 production efficiency at pH 9 and under visible light irradiation. The EY sensitized pure g-C_3N_4 (2.2 μmol h^{-1}) showed a slight activity for H_2 production from an aqueous solution that increased to 29.3 μmol h^{-1} and 78.4 μmol h^{-1} with loading a single metal sulfide co-catalyst of CoS_2 and MoS_2, respectively. Next, with the co-loading of both the sulfides the complex system $Co_xMo_{1-x}S_2$/g-C_3N_4 demonstrated an enhanced rate of H_2 production, 176.5 μmol h^{-1}. Furthermore, the photocatalyst system showed a stable production of H_2 in repeated cycles.

An artificial Z-scheme photocatalytic system of $ZnIn_2S_4$/nanocarbon/g-C_3N_4 was developed for visible-light-driven H_2 production [71]. Nanocarbon sandwiched in between the heterojunction forming semiconductors was anticipated to act as a solid electron mediator. The rate of H_2 production on the nanocomposite photocatalyst system reached to 50.32 μmol h^{-1} that was about 3.4 times higher comparing with $ZnIn_2S_4$, and pure g-C_3N_4 was almost inactive. Towards the development of a non-noble metal photocatalyst for H_2 production from water, Li et al. investigated dual synergetic effects from pyridine modification of g-C_3N_4 and loading with MoS_2 co-catalyst [72]. At first, a donor-acceptor system of pyridine modified g-C_3N_4 was synthesized from co-pyrolysis of 2,5-dibromopyridine and urea at 550 °C for 2 h. TEM analysis showed nanosized flower-like MoS_2 folded from nanosheets of ~2 nm was loaded onto the donor-acceptor system by a solvothermal method. Under visible-light irradiation, the optimized system with 3% MoS_2 showed an enhanced and stable rate of H_2 evolution, 25 μmol h^{-1}. For the MoS_2 co-catalyst loaded samples, the amount of H_2 produced over pyridine modified complex photocatalyst was 2.5 times higher than the pristine system.

CdS is an important material for visible-active photocatalysis but, suffers from photo-corrosion, so the construction of its composites is helpful in gaining stability. Recently, Cheng et al. used a low-temperature solid-state method to fabricate ternary nanocomposites of two metal sulfides, CdS and CuS with g-C_3N_4 [73]. The intimate connection between metal sulfides and g-C_3N_4 nanosheets was clearly observed in the high-resolution TEM to fabricate the triple heterojunction. TEM images of the nanocomposite showed nanosheets of g-C_3N_4 loaded with about 8 nm sized CdS nanoparticles closely adjacent to CuS nanoparticles (Fig. 9A & B). The size of CuS nanoparticles was smaller with reference to 8 nm size of CdS. The construction of the triple heterojunction was important for the accelerated separation of photoexcited charge carriers and their respective reactions are illustrated in the schematic diagram, Fig. 9C. In comparison with the pure materials and binary composites, this ternary composite demonstrated a remarkable enhancement in the photocatalytic activity. The optimized nanocomposite exhibited H_2 production rate of around 57.6 μmol h^{-1} under visible light irradiation. The corresponding apparent quantum efficiency reached to 16.5% at 420 nm.

Lately, Zhang et al. reported on the design of ~7 nm Cu-Cu_2O well distributed g-C_3N_4 nanocomposite and sensitized with Erythrosin B for visible-light-driven H_2 production from water [74]. TEM analysis showed that ~7 nm nanoparticles of Cu-Cu_2O were well dispersed on the surface of g-C_3N_4. For the composite with 7 wt.% copper, the rate of H_2 reached to 400 μmol g^{-1} h^{-1} which was ~3 times higher compared with pure g-C_3N_4 (140 μmol g^{-1} h^{-1}). Next, a significant improvement was observed with the dye sensitization and the rate reached to 5000 μmol g^{-1} h^{-1} but showed a slight decrease in recycling tests. Hou et al. used a combination of foaming-assisted electrospinning process and followed by a solution dipping process for fabrication of ternary hybrid nanofibers of TiO_2, WO_3, and g-C_3N_4 [75]. Thoroughly mesoporous ternary hybrid nanofibers of around 200 nm

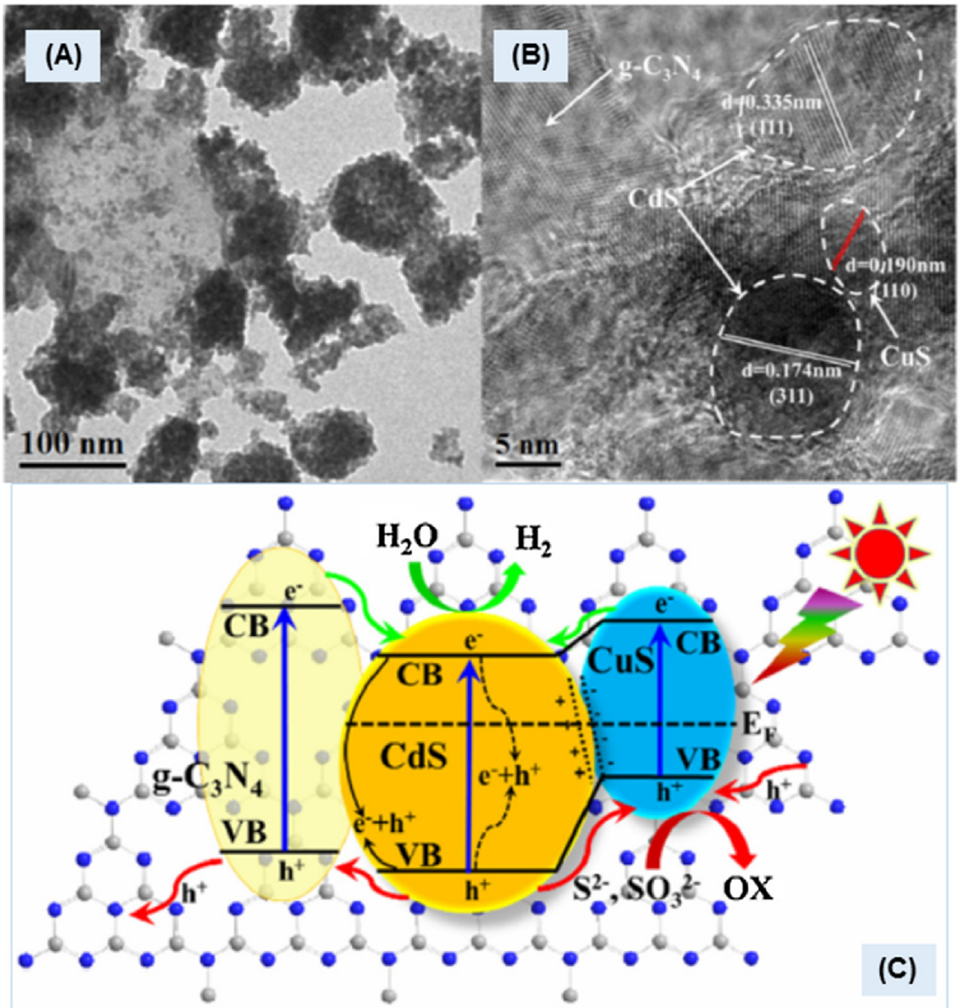

Fig. 9. (A) TEM and (B) HR-TEM images of the as-prepared ternary composite of CdS/g-C_3N_4/CuS, (C) Inferential schematic mechanism proposed for the photocatalytic production of H_2 over the ternary nanocomposite under visible-light irradiation.
Reproduced with permission from the Ref. [73]. Copyright (2016) Elsevier.

diameter were synthesized in the process. This noble-metal-free hybrid yielded a high and stable visible-light-driven photocatalytic H_2 release at a rate of ~287 μmol h^{-1} compared with the individual components. In comparison with pristine g-C_3N_4 and TiO_2 P25, the nanofiber composite showed better stability in consecutive photocatalytic cycles. All of these studies provide important strategies towards design and development of noble-metal-free efficient photocatalyst systems for sustainable harvesting of solar energy.

2.3. O_2 evolution reaction

In natural photosynthesis, water oxidation is a crucial step in a series of reactions required for the sunlight-light-driven conversion of CO_2 and H_2O into sugar. The water oxidation half-reaction is a key step and major bottleneck to control overall water splitting process as it requires transfer of four electrons [76]. In the two half reactions of water splitting, the oxidation is considered a complicated process for it involves the sluggish transfer of four electrons. A large scale application of the most active catalyst systems for water oxidation based on Ir and Ru are hindered because of the high cost and environmental issues [77,78]. Therefore, the development of low-cost catalyst systems is important for sustainable application of water splitting process.

For water splitting via separate H_2 and/or O_2 evolution half reactions, significant advances have been made with the development of H_2 evolution reaction, and only a few researchers have attempted on O_2 evolution reaction for it is a difficult step requiring transfer for four electrons [13,2]. In the photocatalytic reactions, $AgNO_3$ is usually used as a sacrificial reagent to trap electrons and leave holes for O_2 evolution half reaction of water splitting. Photocatalytic O_2 evolution from water is a key bottleneck for the conversion and storage of solar energy in the chemical form. A sluggish requirement for transfer of four-electrons and high activation energy barrier for oxygen–oxygen bond formation are the main difficulties with the development of a water oxidation catalyst for photocatalytic O_2 evolution half reaction.

The role of band gap engineering towards improved photocatalytic activity of g-C_3N_4 was investigated by its sulfur-mediated solid-state synthesis under N_2 flow [79]. Sulfur-doping of g-C_3N_4 helped in lowering of the valence band position and was ascribed to the enhanced photocatalytic activity of this metal-free system for water oxidation reaction. The material produced with sulfur-mediated approach depicted nanopores of 20–30 nm and a high specific surface area (60 m^2 g^{-1}) compared with bulk g-C_3N_4 (10 m^2 g^{-1}). For the reaction under the UV–vis light, the rate of O_2 evolution over the optimized material reached to 20.1 μmol h^{-1} that was 4.2 times higher comparing with pure bulk g-C_3N_4.

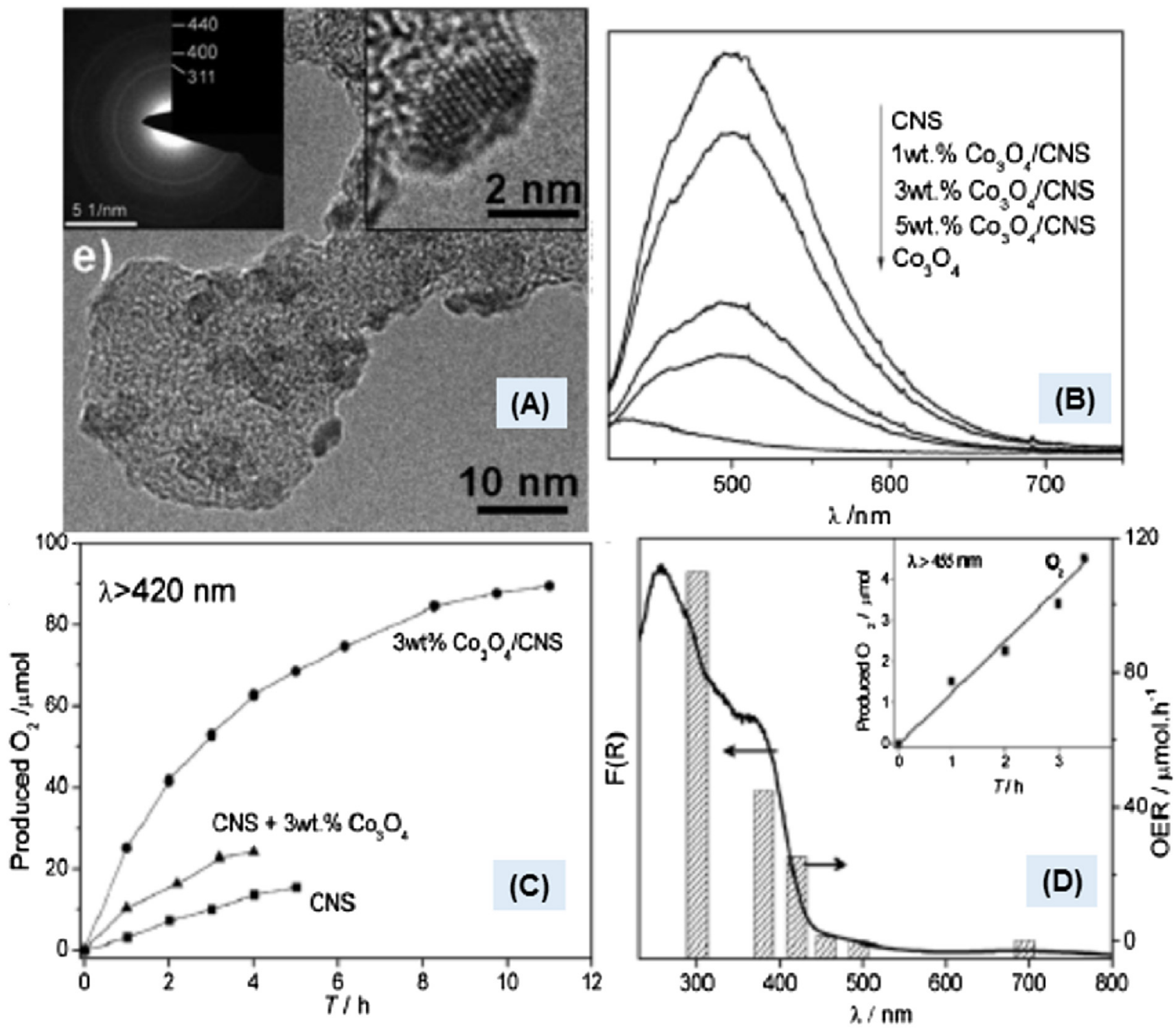

Fig. 10. (A) HR-TEM images of the Co_3O_4 nanoparticles on sulfur-mediated synthesized g-C_3N_4 (CNS), (B) PL spectra of CNS, Co_3O_4, and nanohybrids with various amounts of Co_3O_4 loaded on CNS, (C) Visible light active O_2 evolution by CNS, CNS + 3 wt.% Co_3O_4 (physical mixture), and 3 wt.% Co_3O_4/CNS nanohybrid, and (D) Wavelength dependent O_2 evolution rate over 3 wt.% Co_3O_4/CNS nanohybrid. The inset in (D) is the O_2 evolution curve under visible light ($\lambda > 455$ nm).

Next, Zhang et al. combined this g-C_3N_4 photocatalyst prepared via sulfur-mediated synthesis approach with nanoparticles of a water oxidation catalyst, Co_3O_4 [80]. As shown in Fig. 10A, the composite exhibited a well-constructed nanohybrid structure of g-C_3N_4 with Co_3O_4 nanocrystals of ~3 nm diameter. A tight electronic and spatial interaction in the nanohybrid structure was observed with an increased quenching of the PL intensity upon loadings of Co_3O_4 (Fig. 10B) and further confirmed by X-ray photoelectron spectroscopy studies. A synergistic effect was found upon the construction of a composite of Co_3O_4 nanoparticles and S-doped g-C_3N_4. The formation of nanojunctions was believed to promote the direct transfer of photogenerated holes to Co_3O_4. Under visible light, the nanohybrid system with a well-constructed heterojunction demonstrated significantly enhanced O_2 evolution comparing with pure semiconductor and its physical mixture with Co_3O_4 (Fig. 10C). Loading of Co_3O_4 at 3 wt.% was found the optimum for water oxidation reaction. In comparison to O_2 production by the co-catalyst free material (2.8 μmol h^{-1}), the rate was significantly enhanced to 25.1 μmol h^{-1} over this hybrid composite, under visible light irradiation. The rate of O_2 evolution was dependent on the optical absorption of the organic semiconductor material (Fig. 10D). This observation supports that the process of water oxidation was initiated by photo-induced excitation of the polymeric semiconductor. For the optimized nanohybrid structure, an apparent quantum efficiency of 1.1% was determined under illumination at 420 nm.

In search of a metal-free g-C_3N_4 based photooxidation catalyst, Chu et al. tuned the band structure of g-C_3N_4 by incorporating electron-deficient pyromellitic dianhydride monomer [81]. The TEM analysis showed interconnected particles for the polyimide composite with sizes of ~50 nm. Thus obtained polyimide depicted a lowering of valence band position (by 0.8 V) even more pronounced than that was observed with S-doping (by 0.2 V), and consequently demonstrated an enhanced capability for water oxidation. Under visible-light irradiation, the initial rate of O_2 production on polyimide was estimated to be 7.7 μmol h^{-1} that was about an order of magnitude larger than that of pristine g-C_3N_4 (0.8 μmol h^{-1}), and almost double comparing with the rate over S-doped g-C_3N_4 (3.6 μmol h^{-1}).

2.4. H_2O_2 generation

Photocatalytic generation of H_2O_2 is important for its in-situ use in advanced oxidation process, and potential use as a fuel.

Furthermore its solubility in water and easy transport compared with H_2 makes it an interesting candidate as a solar fuel. Kofuji et al. constructed visible light active nanohybrids of g-C_3N_4 with aromatic diimide and graphene for reduction of O_2 to H_2O_2 [82]. Under visible light irradiation for 24 h, g-C_3N_4 modified with aromatic diimide produced 14 μmol of H_2O_2. While the optimized catalyst system including appropriate constituent of graphene generated double amount of H_2O_2 (29 μmol). Li et al. demonstrated the construction of a solid-gas interface of a Fenton reaction over g-C_3N_4 modified with hydroxyl and Fe^{3+} species [83]. These modifications played significant roles in photoactive production of H^+ and Fe^{2+}/Fe^{3+} pair formation, and therefore determined the rate of H_2O_2 generation. Pristine g-C_3N_4 was inactive for producing H_2O_2 while only hydroxyl modified sample generated about 3.4 μmol of H_2O_2. A highly enhanced amount of H_2O_2 generated in 1 h over the sample modified with hydroxyl and Fe^{3+} species was estimated to be 522 μmol.

2.5. CO_2 reduction

Photocatalytic conversion of CO_2 to value added chemicals is immensely important for that not only reduces the level of greenhouse gas but also helps meet the demand for the renewable fuels. In the late 1970s, Halmann, and Inoue et al. first reported the light-induced reduction of CO_2 [84,85]. Artificial photosynthesis over semiconductor materials for reduction of CO_2 into various chemicals is a highly sought after reaction to fulfill energy demands and mitigate climate changes. As the production of chemical fuels from CO_2 has been considered an ideal solution to simultaneously solve the issues with environment and energy. Therefore, many researchers have attempted various semiconductor materials for the photocatalytic conversion of CO_2.

Metal-free microstructures of g-C_3N_4 nano-flakes derived from different precursors were evaluated for photoreduction of CO_2, under visible-light irradiation. Mao et al. heat treated urea and melamine to modulate microstructure of the produced g-C_3N_4 [86]. A mesoporous structure of nano-flakes of around 5 nm for the g-C_3N_4 (obtained from urea) produced methanol and ethanol at rates of 6.28 μmol g^{-1} h^{-1} and 4.51 μmol g^{-1} h^{-1}, respectively. On the other hand, a non-porous sample of g-C_3N_4 (obtained from melamine) produced ethanol only and at a lower rate, 3.64 μmol g^{-1} h^{-1}. Hence, the mesoporous structure from nano-flakes demonstrated higher photoactivity for CO_2 reduction. Furthermore, alcohols were the only product obtained from the photoreduction of CO_2 on metal-free g-C_3N_4. The selectivity of CO_2 photoreduction products became more diverse with the research work reported by Niu et al. that used bulk g-C_3N_4 and its nanosheets of around 2 nm size as photocatalysts [87]. Under various experimental conditions, methane and acetaldehyde were the only product of CO_2 photoreduction. Bulk g-C_3N_4 (bandgap ~2.7 eV) produced CH_3CHO only while conversion over g-C_3N_4 nanosheets (bandgap ~2.9 eV) was selective to CH_4.

A further development was made by Ong et al. by the construction of hybrid nanostructure via a combined sonication-assisted and surface charge modification strategy [88]. A metal-free photocatalyst of 2D/2D hybrid heterostructure was prepared from protonated g-C_3N_4 and reduced graphene oxide (rGO). An intimate contact across the heterojunction interface was seen by the TEM and spectroscopic analysis. The optimized nanostructure with 15 wt.% rGO exhibited a considerably enhanced conversion of CO_2 (~14 μmol g_{cat}^{-1}) in the presence of water vapors into CH_4, under illumination from an energy-saving daylight bulb. The photochemical quantum yield was 0.56% which was 5.4 and 1.7 times higher compared with protonated g-C_3N_4 and 15 wt.% of rGO on bulk g-C_3N_4. The enhanced photocatalytic activity of the nanostructure was attributed to the intimately connected rGO for an effective separation of photogenerated charges. Construction of Z-scheme photocatalysts has received much attention for CO_2 reduction, and an effective indirect Z-scheme of BiOI/g-C_3N_4 was synthesized by Wang et al. via a simple deposition method [89].

Shi et al. decorated nanosheets of g-C_3N_4 onto zirconium metal-organic framework (MOF; UiO-66) via a facile electrostatic self-assembly method [90]. TEM analysis of the nanocomposite showed ~4 nm thick nanosheets decorated onto MOF structure (Fig. 11A). BET surface area of the composite was around 1340 m^2 g^{-1}. The nanocomposite was highly active for the photocatalytic reduction of CO_2 to CO comparing with the g-C_3N_4 nanosheets alone and the composite prepared from bulk g-C_3N_4 (Fig. 11B). Photoluminescence spectra showed a significant quenching of the intensity indicating a better separation of photoexcited electron-hole pairs in the nanocomposite (Fig. 11C). This phenomenon was further confirmed with fluorescence lifetime measurements. Hence, transfer of photogenerated electrons from the nanosheets to the MOF was substantially suppressing the recombination of electron-hole pairs. Suitable potentials of the nanocomposite for CO_2 reduction and the proposed mechanism under visible light irradiation are depicted in Fig. 11D. Besides a strong adsorption capacity, an efficient separation of charge carriers was found important for this high activity of the nanocomposite. The rate of CO evolution over the optimized composite containing 10 wt.% g-C_3N_4 nanosheet was the highest, and yield reached to more than 3 times better than that of the nanosheets alone. A slight drop in the photocatalytic activity was seen during the recycling tests.

In an effort to develop noble-metal-free photocatalyst, Zhou et al. developed a series of g-C_3N_4 composites with nitrogen-doped TiO_2 by a simple pyrolysis process [91]. Formation of porous g-C_3N_4 and loading with nanoparticles were evidenced from N_2 sorption and microscopy studies. TEM analysis showed nanoparticles in the range of 20 nm to 40 nm dispersed on the surface of g-C_3N_4 nanosheets. Pertaining to its enhanced absorption of light and ease with the separation of charge carriers, the nanocomposite was highly active for CO_2 reduction selectively into CO. Under 12 h irradiation, about 15 μmol of CO was obtained which was four times higher compared with the commercial TiO_2 P25. Another similar nanocomposite system for CO_2 reduction was developed by Raziq et al. by combining nanosize TiO_2 and B-doping of g-C_3N_4 nanosheets [54]. The coupling of B-doped nanosheets of g-C_3N_4 with nanocrystalline TiO_2 for the construction of co-catalyst free nanojunctions was carried out by the facile calcination method. TEM analysis revealed finite ~5 nm diameter nanoparticles of TiO_2 well-dispersed on the surface of the organic semiconductor. The separation of photogenerated charges was improved after B-doping and further enhanced upon coupling with nanosized TiO_2. Upon B-doping of the g-C_3N_4 structure, the amount of CH_4 in 8 h photocatalytic reaction increased from ~7 μmol (pristine g-C_3N_4) to 68 μmol. The highest amount of CH_4, 106 μmol was observed over the nanocomposite. In contrast to the CO_2 reduction to CO over the nitrogen-doped TiO_2 composite observed by Zhou et al. [91], here in this study CH_4 was the main product. The rate of H_2 evolution was also similarly increased upon B-doping of g-C_3N_4 and further with the construction of heterojunction with TiO_2.

A simple impregnation strategy was adopted by He et al. for the synthesis of ZnO nanoparticle-functionalized g-C_3N_4 as shown in Fig. 12A [92]. TEM analysis showed a close coupling of ZnO nanoparticles onto the surface of g-C_3N_4. Electrochemical impedance spectra demonstrated efficient charge transfer between the components of the optimized nanocomposite (Fig. 12B). Comparing with a physical mixture of ZnO and g-C_3N_4 the presence of strong affinity between the two semiconductors in the composite was further confirmed by the X-ray photoelectron spectroscopy. The composite demonstrated a superior performance for

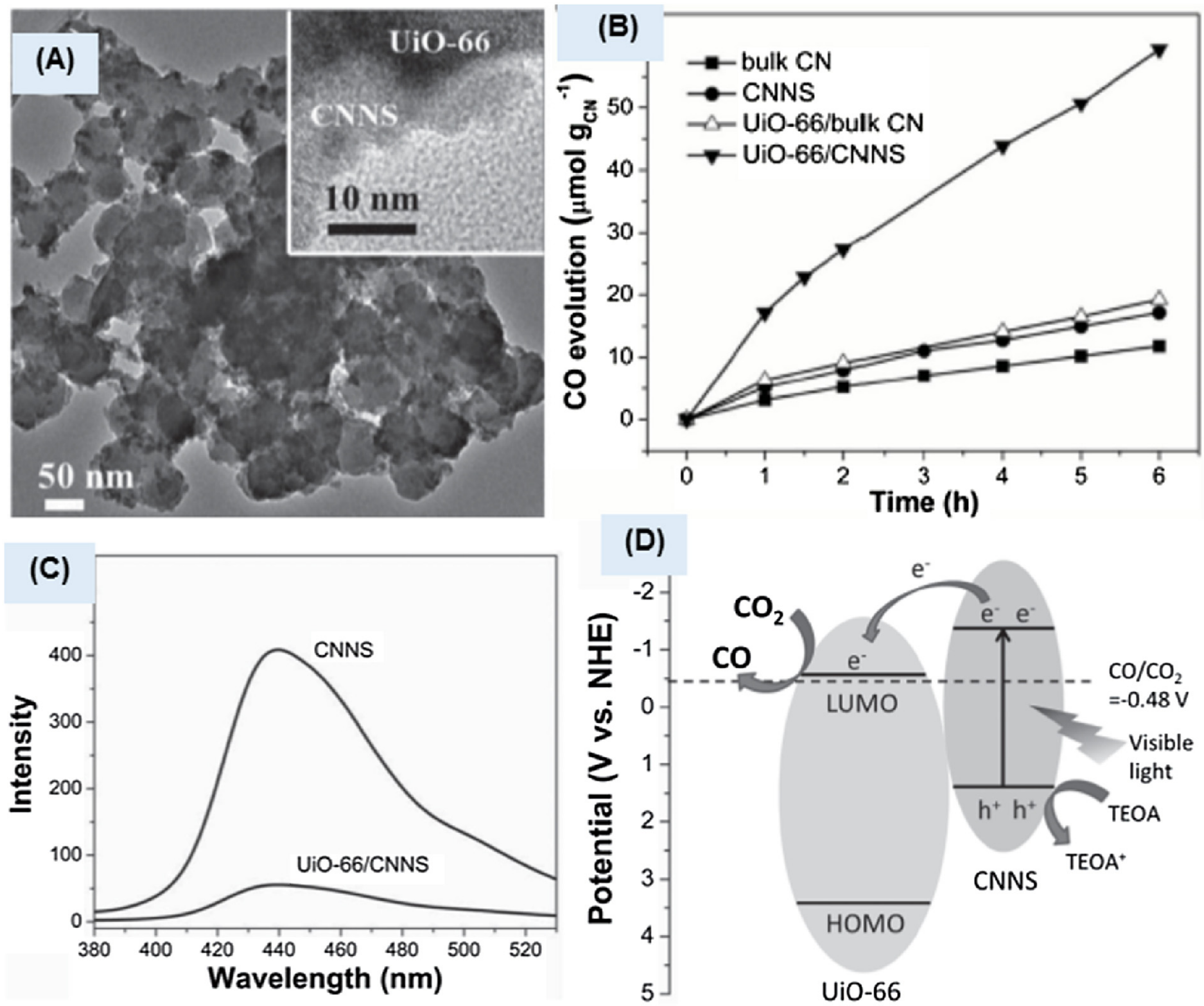

Fig. 11. (A) TEM and HR-TEM images of nanocomposite of Zr-MOF (UiO-66) and g-C3N4 nanosheet (CNNS), (B) Time course of CO evolution over bulk g-C_3N_4 (CN), CNNS, UiO-66/bulk CN, and UiO-66/CNNS photocatalysts, (C) PL spectra of CNNS and UiO-66/CNNS, and (D) Schematic of proposed photocatalytic reduction mechanism of CO_2 by the UiO-66/CNNS heterogeneous photocatalyst under visible light irradiation.
Reproduced with permission from the Ref. [90]. Copyright (2015) Wiley.

photocatalytic CO_2 reduction due to effective separation of charges at the interface (Fig. 12C). CO and methanol were the main reaction products from the photocatalytic reduction of CO_2. The optimized heterojunction with 6 wt.% ZnO demonstrated a CO_2 conversion rate of ~46 μmol h^{-1} $g_{cat}{}^{-1}$ that was 4.9 and 6.4 times higher than that of the pristine g-C_3N_4 and TiO_2 P25, respectively. A physical mixture of 6 wt.% ZnO with g-C_3N_4 (6ZC-PM) showed much less rate of CO_2 conversion and stressed the importance of good heterojunction between inorganic-organic semiconductors (Fig. 12C). However, the cyclic runs for the optimized catalyst showed a small decrease in the photoactivity.

Besides ZnO, He et al. also used ~50 nm sized nano-spherical SnO_{2-X} for the construction of a composite with g-C_3N_4 by simple calcination [93]. The conduction band position of SnO_{2-X} is closer to the valence band position of g-C_3N_4, therefore a direct Z-scheme type composite was formed upon coupling these semiconductors. The nanocomposite was highly efficient for reduction of CO_2 and for the degradation of organic pollutants, under visible light irradiation. Initially, the photocatalytic performance of the composite increased gradually with the SnO_{2-X} concentration and the optimized value was around 42 wt.%, and with further loading the activity was decreased. The photocatalytic CO_2 reduction on the optimized composite reached about 23 μmol h^{-1} $g_{cat}{}^{-1}$ which was 4.3 and 5 times higher than that of the pristine g-C_3N_4 and TiO_2 P25, respectively. In all the various photocatalyst employed in this study, CO was the main product from the reduction of CO_2. The performance of the SnO_{2-X}/g-C_3N_4 nanocomposite was inferior and remained at the half as compared with that of the ZnO/g-C_3N_4 [92]. These studies on noble-metal-free systems present interesting strategies towards the photocatalytic production of fuel from CO_2 and provide important feedback for future developments.

2.6. N_2 fixation

In nature, after photosynthesis, nitrogen fixation is the second most important chemical process and soil-dwelling bacteria are able to utilize N_2 from the air. Industrially, Haber–Bosch process for the catalytic synthesis of ammonia from hydrogen and nitrogen under high pressure and the temperature is the main artificial process for nitrogen fixation. The cost of raw material and the process has been pushing for alternate methods for nitrogen fixation. Since the first report on photocatalytic conversion of N_2, this process has been thought to be the best alternative to traditional techniques. The first study on photofixation was reported by Schrauzer et al. for conversion of N_2 to NH_3 over Fe-doped TiO_2 [94]. Recently, many researchers have attempted on the development of a low-cost and

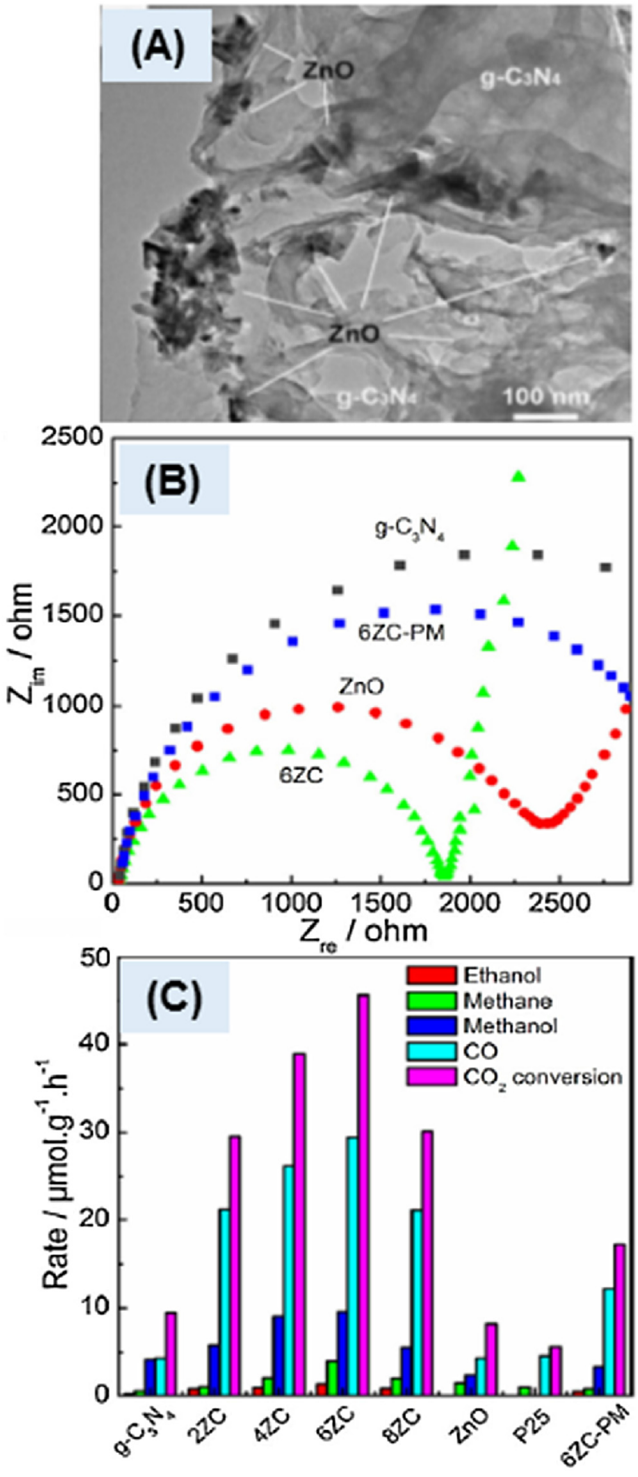

Fig. 12. (A) TEM of a composite of 6 wt.% ZnO and $g\text{-}C_3N_4$ (6ZC), (B) Electrochemical impedance spectral changes in pure materials, a physical mixture of 6 wt.% ZnO and $g\text{-}C_3N_4$ (6ZC-PM) and 6ZC, and (C) Photocatalytic activities of $g\text{-}C_3N_4$, ZnO, P25, and composites of 2–8 wt.% ZnO with $g\text{-}C_3N_4$ (2–8ZC), and 6ZC-PM.

Reproduced with permission from the Ref. [92]. Copyright (2015) Elsevier.

visible-active photocatalyst materials for fixation of N_2. Hu et al. constructed a 2D/2D heterojunction between protonated $g\text{-}C_3N_4$ and reduced rGO [95]. By acid treatment, the electrostatic surface charge on $g\text{-}C_3N_4$ was modulated to make an effective interfacial contact with rGO, and furthermore, it converted the bulk structure to nanosheets. The rate of visible-light-driven generation of NH_4^+ over the optimized heterojunction with sufficient interfacial contact was 3.7 times higher compared with the hybrid structure prepared without surface charge modification. Furthermore, this layered hybrid was highly efficient in the photodegradation of organic pollutant and remained stable in repeated runs.

In another study on the artificial photo-fixation of N_2, Hu et al. prepared a novel heterojunction of ternary metal sulfide, ZnSnCdS with $g\text{-}C_3N_4$ by hydrothermal method [96]. The average size of multi-metal sulfide nanoparticles was in the range of 30–50 nm. An effective separation of photogenerated electron-hole pairs in the strongly coupled heterojunction was evidenced from the imaging and various spectroscopy techniques. High-resolution TEM images showed a tight coupling of irregularly shaped ZnSnCdS with sheet-like $g\text{-}C_3N_4$ which is favorable for the transfer of the photogenerated charges (Fig. 13). As shown in the optical spectra in Fig. 13C, the absorption edges of the heterojunctions were located between that of the pristine $g\text{-}C_3N_4$ and ZnSnCdS and further confirmed the electronic coupling. Because of the effective interfacial charge transfer, an outstanding N_2 photo-fixation was observed over the heterojunction, under visible light irradiation (Fig. 13D). Besides strong coupling of this ternary sulfide with $g\text{-}C_3N_4$ its deficiency in sulfur was found synergistic to provide active sites to absorb and activate N_2 molecules. Under visible light irradiation, the rate of generation of NH_4^+ (7.543 mg L^{-1} h^{-1}) over the optimized composite containing 80% ZnSnCdS was 33.2-folds and 1.6-folds greater comparing with the pristine $g\text{-}C_3N_4$ and pure ZnSnCdS. The nanocomposite was also efficient for photodegradation of rhodamine B (RhB), but the optimized concentration of ZnSnCdS was 20% only. The same research group also prepared a heterojunction of $g\text{-}C_3N_4$ with another ternary metal sulfide, ZnMoCdS [97]. TEM analysis of the composite showed ~50 nm nanoparticles of ZnMoCdS attached on the surface of $g\text{-}C_3N_4$. The optimized composite with only 20% of ZnMoCdS exhibited the highest rate of generation of NH_4^+ (3.5 mg L^{-1} h^{-1}) that was 13.5-folds and 1.75-fold greater than those of pristine $g\text{-}C_3N_4$ and the ZnMoCdS. In conclusion, compared with the Mo-based ternary metal sulfide composite the one prepared from Sn-based ternary metal sulfide demonstrated superior photocatalytic activity for nitrogen fixation.

2.7. Organic synthesis

Both catalytic oxidation and reduction are industrially important reactions for all the various organic synthesis. Wang et al. attempted earliest studies on $g\text{-}C_3N_4$ based materials for photocatalytic organic synthesis reactions [98–100]. Performing organic synthesis reactions in a controlled manner and under safe conditions is critically desired. Photocatalytic activation of O_2 or H_2O_2 for oxidation reaction and use of the in-situ generated H_2 for reduction reaction offer a safe and economical alternative to the industrial processes. Semiconductor materials based on $g\text{-}C_3N_4$ have been evaluated for both oxidation [13,101], and reduction types of reactions [60,102]. Here in this section, we will summarize some $g\text{-}C_3N_4$ based noble-metal-free photocatalytic systems employed for the organic synthesis.

Song et al. used $g\text{-}C_3N_4$, and further modified it with SnO_2 for evaluating photocatalytic esterification of benzaldehyde and various alcohols under visible light irradiation [103]. A slice-like morphology for the nanostructure of as-prepared $g\text{-}C_3N_4$ was observed under TEM. Production of various esters in the presence of H_2O_2 was enhanced under irradiation of visible light. Loading of SnO_2 further significantly promoted the photocatalytic ester formation reaction. Dark conversion of benzaldehyde and ethanol to ethyl benzoate was 24% that increased upon irradiation with light to 32% and further to 41% with the promotor SnO_2. Zhang et al. activated the metal-free $g\text{-}C_3N_4$ through reflux in acidic media,

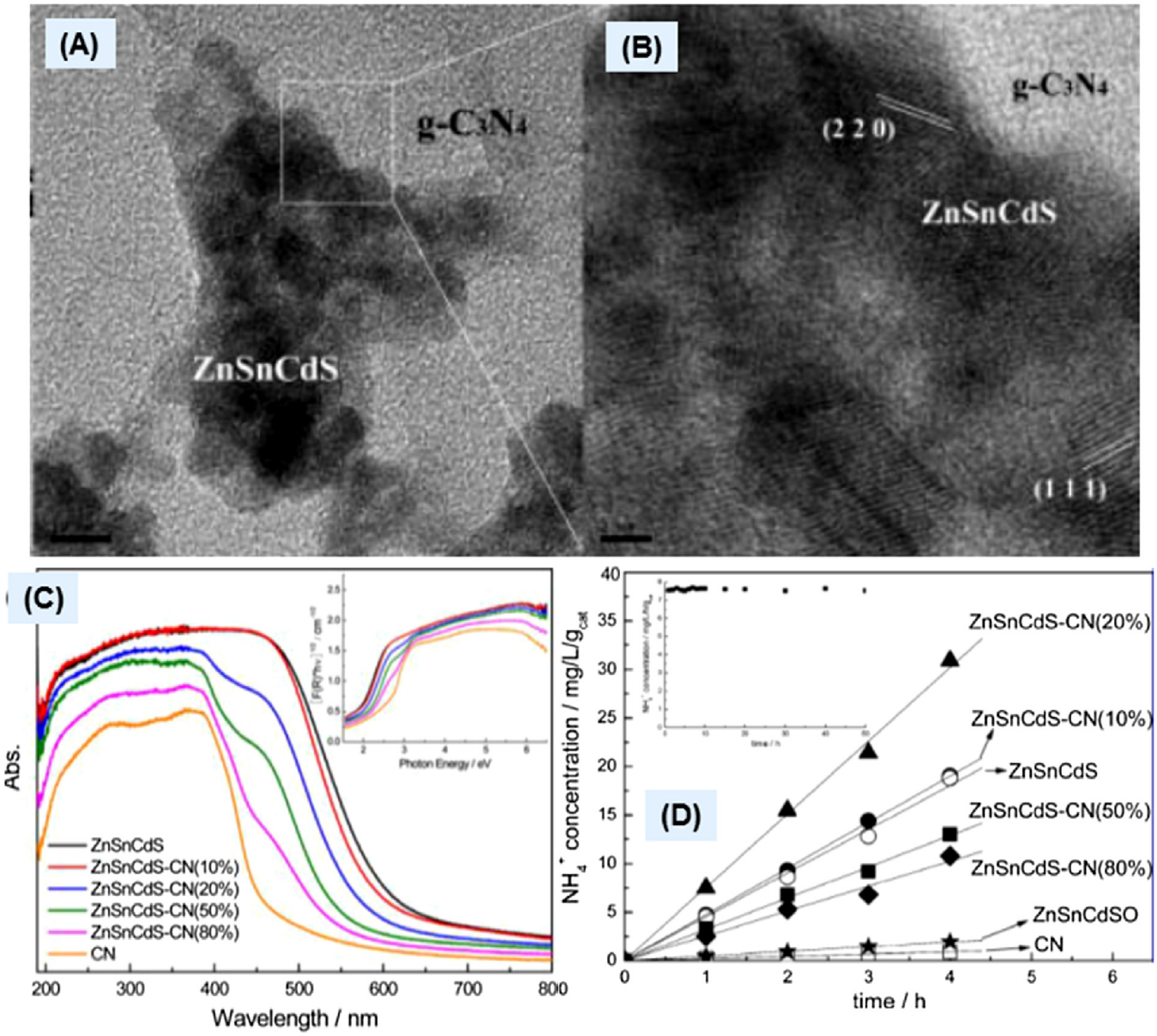

Fig. 13. (A) TEM and (B) HR-TEM images of the ZnSnCdS loaded on g-C_3N_4 (20%), (C) UV–vis spectra of as-prepared materials with Tauc plots in the inset, and (D) Nitrogen photo-fixation performance of the as-prepared catalysts under visible light. The inset in (D) shows the photocatalytic stability of ZnSnCdS-CN(20%).
Reproduced with permission from the Ref. [96]. Copyright (2016) American Chemical Society.

essentially changing the bulk to nanostructures [104]. The modified polymeric semiconductor was used for the selective aerobic oxidation of benzyl alcohol under visible light irradiation. Among all the acidified samples, the one treated with sulfuric acid gave 23% yield of benzaldehyde under 4 h irradiation of visible light which was 2.5 times higher comparing with pristine g-C_3N_4. The enhanced photocatalytic performance of acidified g-C_3N_4 was attributed to a larger specific surface area and enhanced surface chemical property of the nanoporous sheets of g-C_3N_4.

Shiravand et al. loaded nanoporous silica (LUS-1) with Fe-containing g-C_3N_4 by impregnation followed calcination method [105]. From XRD studies they proposed the formation of a nanoscale layer of g-C_3N_4 on the surface of LUS-1. A drastic enhancement in the hydroxylation of benzene to phenol in the presence of H_2O_2 was observed over the optimized nanostructure catalyst under sunlight. A maximum yield of phenol (16%) was exhibited by g-C_3N_4 with 20%Fe and loaded onto LUS-1. Ye et al. also worked on the selective production of phenol over similar catalyst system; nano-coating of Fe-containing g-C_3N_4 on titanium silicate zeolite (TS-1) [106]. Under visible light irradiation, more than 10% yield of phenol was observed over the optimized composite that was higher comparing with pure materials. Under visible light, Fe-containing g-C_3N_4 loaded on LUS-1 showed a better yield of phenol ~16% comparing with the one loaded on TS-1 (10%).

Recently, Nasir Baig et al. worked on magnetic Fe species loaded onto g-C_3N_4 for a sustainable application in photocatalytic hydrogenation, under visible light irradiation [102]. TEM analysis showed that aggregates of nano-sized ferrite were loaded onto g-C_3N_4, Fe@g-C_3N_4. The nanocomposite systems were screened for the hydrogenation of styrene and with an optimized concentration of Fe (10%) the obtained yield was 98%. During the photocatalytic reaction at room temperature, hydrazine was used as a source of H_2. The magnetically separable nano-ferrite system was efficient for the photocatalytic hydrogenation of various alkenes and alkynes. TEM analysis showed that nano-ferrite remained stable during photocatalytic testing. Suyana et al. prepared a composite of g-C_3N_4 with ZnS by the one-pot synthetic approach [60]. TEM analysis showed 4–7 nm sized nanoparticles of ZnS in the nanocomposite. The optimized heterojunction with 14 wt.% ZnS demonstrated more than 90% photocatalytic reduction of *p*-nitrophenol to *p*-aminophenol, under 240 min illumination with sunlight. Sodium

sulfite was used as a hole scavenger during this photoreduction reaction of *p*-nitrophenol.

Dai et al. prepared a nanocomposite of CdS with g-C_3N_4 via a hydrothermal method [107]. TEM image depicted ~50 nm nanoparticles of CdS decorated on the surface of g-C_3N_4. In comparison with the individual components, the composite was highly efficient for visible light active selective oxidation of benzyl alcohol by holes to benzaldehyde and reduction of nitrobenzene by electrons to aniline. Under 4 h of illumination over the optimized system, the yield of benzaldehyde and nitrobenzene was 44.6% and 26.0%, respectively. A small decrease in photocatalytic activity was noticed in cycling tests. Zhang et al. prepared a nanocomposite from the decoration of in-situ prepared $Ag_3PW_{12}O_{40}$ onto g-C_3N_4 by stirring with precursors, at room temperature [108]. TEM analysis showed that uniform nanospheres (~5 nm) of $Ag_3PW_{12}O_{40}$ were anchored on g-C_3N_4 nanosheets. The nanocomposite was highly active for selective photocatalytic conversion of cyclooctene and cyclohexane without adding any oxidant at 60 °C. The photocatalytic oxidative conversion of cyclohexanone was 8.62% with more than 99% selectivity to cyclohexanone under near-UV irradiation. For cyclooctene, the conversion reached 41.2% with selectivity mainly to epoxycyclooctane (77.2%). This noble-metal-free system remained stable in the repeated cycles of photocatalytic oxidation reactions. These studies provide significant guidance in designing sustainable catalyst systems and appropriate reaction conditions for realizing light-induced catalytic oxidation and reduction reactions.

2.8. Degradation of organic pollutants

Degradation of organic pollutants in the environment over the semiconductor solids is an extensively explored reaction by heterogeneous photocatalysis [109]. Similarly, most of the studies on photocatalytic properties of g-C_3N_4 and its modified system also focused on environmental remediation reactions, usually using organic dyes as a model pollutant [2,12]. From a large volume of research papers on the topic of photocatalytic degradation of organic pollutants (Fig. 3), we provide here a summary of few from each of the different categories of materials and modifications. In line with the focus of this review, we will mainly discuss some noble-metal-free or precious-metal-free nanoscale photocatalyst systems.

2.8.1. Metal-free photocatalyst system

Development of metal-free photocatalyst materials is important for their sustainable application. Zhang et al. prepared carbon-rich g-C_3N_4 nanosheets by hydrothermal method [110]. In comparison with the pristine g-C_3N_4, the modified semiconductor showed a significantly enhanced photocatalytic degradation of 4-nitophenol, under visible light irradiation. Oxygen functionalized g-C_3N_4 and co-doped with S and P was synthesized by hydrothermal post-treatment [111]. The modified material was highly active for visible-active photodegradation of RhB, methylene blue (MB), methyl orange (MO) and phenol under anoxic conditions. The highest RhB degradation constant, 0.026 min^{-1} was 13 times higher comparing with the pristine g-C_3N_4. Dang et al. synthesized a core-shell heterojunction via a self-assembly process [112]. A spherical core of α-S was enwrapped with ultra-thin nanosheets of g-C_3N_4 for rapid charge transfer. The composite with 35% of g-C_3N_4 nanosheets demonstrated the highest photocatalytic degradation of RhB with 6.7 times faster rate compared with α-S.

Modification of g-C_3N_4 with carbon-based nanostructures has been attracting attention for an enhanced absorption of visible-to-IR and fast transfer of photogenerated carriers. Liao et al. fabricated graphene oxide (GO) modified g-C_3N_4 by the sonochemical approach [113]. This metal-free hybrid structure of nanosheets showed efficient photocatalytic degradation of organic pollutants under visible light irradiation. The photodegradation of RhB and 2, 4-dichlorophnol over the hybrid structure was 3.8 and 2.1 times higher comparing with pristine g-C_3N_4. Another carbon-based material, multi-walled carbon nanotubes was combined with g-C_3N_4 nanosheets due to electrostatically-driven self-assembly with the hydrothermal method [114]. The visible-light-driven photodegradation of MB by the composite was 8.1 times of that of the g-C_3N_4 nanosheets. Bai et al. modified g-C_3N_4 with Fullerene (C_{60}) via a facile thermal treatment [115]. Photocatalytic degradation of MB and phenol was carried out under visible light irradiation. Comparing with bulk g-C_3N_4 the efficiency of the composite was 2.9 times and 4.0 times higher for phenol and MB, respectively. Sun et al. decorated glucose-derived carbon nanospheres onto g-C_3N_4 via a hydrothermal method [116]. For the degradation of phenol under simulated sunlight, the nanocomposite demonstrated 4.9 times higher efficiency compared with pristine g-C_3N_4.

2.8.2. Transition metal based system

Photodegradation of organic wastewater over semiconductor materials has received considerable attention to cope up with the environmental challenges. The mainly explored wide band gap semiconductor oxides TiO_2 and ZnO are not suitable for harvesting solar light. Among transition metal based g-C_3N_4 systems, modifications with titanium materials are most explored for an understandable combination of these two semiconductor photocatalysts of main interest. Chang et al. prepared composites of 10–20 nm TiO_2 nanoparticles with exfoliated nanosheets through a facile sol-gel method [117]. The hybrid structure was highly active for visible-light-driven degradation of RhB. The apparent reaction rate constant for the optimized composite was 2.4 and 7.0 times higher compared with bare TiO_2 and N-TiO_2, respectively. Zhu et al. used an in-situ calcination method for the synthesis of a composite of homogeneously embedded 20–30 nm TiO_2 P25 in the sheets of g-C_3N_4 [118]. For the optimized nanocomposite, the photodegradation efficiency was 3.3 times higher than that of the pure g-C_3N_4 under visible light. Thin films of g-C_3N_4 from melamine and ~14 nm TiO_2 nanoparticles were prepared by thermal heating in Ar atmosphere [119]. Visible-light-driven degradation of MB over the optimized hybrid was almost twice in comparison with pure TiO_2.

Ma et al. used a hard template, SiO_2 for preparing mesoporous g-C_3N_4, and loaded it with 5–10 nm sized nanoparticles of TiO_2 [120]. For the degradation of RhB under visible light irradiation, the optimized heterojunction demonstrated 1.6 times higher rate than that of the pure mesoporous g-C_3N_4. Zhou et al. prepared an irregularly agglomerated hybrid of 20–40 nm size from ball milling of TiO_2 and g-C_3N_4 [121]. Photocatalytic activity of the hybrid material was 3.0 and 1.3 times higher than those of the pure g-C_3N_4 and TiO_2, respectively. Li et al. optimized solvothermal conditions for seed-induced growth of 50 nm to 200 nm sized TiO_2 nanoparticles loaded onto nanosheets of g-C_3N_4 [122]. In comparison with direct-grown composite and pure g-C_3N_4 the seed-grown composites were highly efficient for degradation of MO and phenol under visible light irradiation. For the optimized seed-grown composite, the photodegradation rate constant for MO and phenol was 30 and 14 times higher than that of the pristine g-C_3N_4. Li et al. used a simple one-step calcination of $H_2Ti_3O_7$ and melamine precursors for the synthesis of Ti^{3+} self-doped TiO_2 heterojunction with g-C_3N_4 [123]. The photodegradation of MB was studied under a 30 W visible-light-emitting diode. The removal rate constant for the optimized composite reached 0.038 min^{-1} which was 26.7 and 7.6 times higher compared with pure TiO_2 and g-C_3N_4, respectively. Lu et al. prepared a composite of Ti^{3+} containing TiO_2 rectangular nanosheets of 100 nm and g-C_3N_4 by hydrothermal-sonication assisted strategy [124]. The optimized composite was highly active

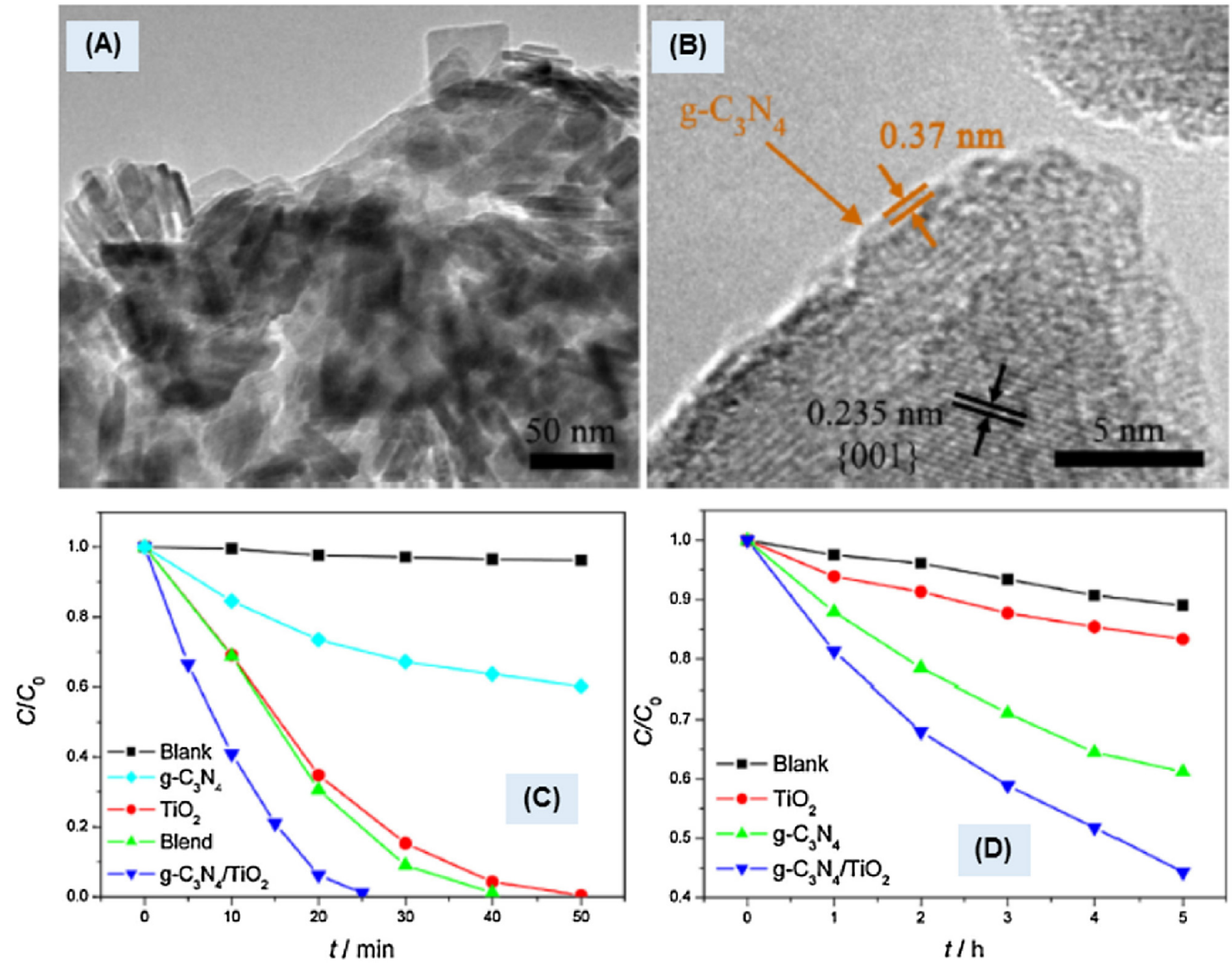

Fig. 14. (A) TEM image of TiO_2 and g-C_3N_4 hybrid structure, (B) HR-TEM of the hybrid, (C) Photocatalytic degradation of MB under UV irradiation, and (D) Photocatalytic degradation of MB under visible-light irradiation.

for visible-light-driven photooxidation of RhB and photoreduction of Cr^{6+}.

Gu et al. developed a facile solvent evaporation method for hybridizing TiO_2 with dominant {001} facets with g-C_3N_4 [125]. The high-energy {001} facets calculated for the sheet-like anatase nanocrystals (~38 X ~6 nm) was about 76% for pure TiO_2. The optimal amount of g-C_3N_4 in the heterojunction was around 5.3% as estimated by the thermogravimetric analysis. Well-defined boundaries of TiO_2 nanosheets displayed an obscure bulk configuration upon hybridization with g-C_3N_4 as studied by TEM (Fig. 14A). For the hybrid structure, the lattice spacing of 0.235 nm was seen in the HR-TEM that was assigned to the exposed {001} facet of TiO_2 (Fig. 14B). Furthermore, an outermost layer of about 0.37 nm in the HR-TEM was corresponding to a monolayer of g-C_3N_4 (ca. 0.325 nm). TEM and spectroscopic studies demonstrated a strong interfacial interaction between TiO_2 and g-C_3N_4. The photocatalytic activity of the heterojunction structure was evaluated for the degradation of MB, RhB, acridine orange, and 2,4-dichlorophenol under both UV and visible light irradiations (Fig. 14C & D). The optimized composite showed the highest photocatalytic degradation towards all the organic dyes illustrating the importance of heterojunction.

N-doping in TiO_2 is an important strategy in making it visible active photocatalyst, and further heterojunction with another suitable semiconductor is added advantage. Wang et al. used an in-situ microwave-assisted approach for the synthesis of composites of ~15 nm spherical N-TiO_2 and g-C_3N_4 nanosheets [126]. H_2TiO_3 was used as a precursor for TiO_2 and $NH_3{\cdot}H_2O$ as the N-doping source. The heterojunction was highly efficient for visible-light-driven photodegradation of RhB and MO. The rate of photodegradation of RhB over the optimize composite was 2 and 2.7 times higher than that of the pure g-C_3N_4 and N-TiO_2. Li et al. constructed heterojunction between 10 and 30 nm N-TiO_2 nanoparticles and g-C_3N_4 nanosheets by direct co-calcination [127]. Visible-light-driven photodegradation of RhB over the optimized composite was 19 and 5.3 times higher compared with individual N-TiO_2 and g-C_3N_4, respectively. Recently, Sun et al. prepared an in-situ composite of N-TiO_2 nanoparticles of 30–50 nm and g-C_3N_4 from one-step calcination of TiN and melamine [128]. Under visible light irradiation, the efficiency of optimized composite towards photodegradation of MB was just 1.9 times greater than compared with N-TiO_2. Kumar et al. prepared nanocomposite from N-doped $SrTiO_3$ nanoparticles of ~50 nm and g-C_3N_4 by a polymeric citrate and thermal exfoliation method [129]. The optimized nanocomposite (0.0558 min^{-1}) showed much higher photocatalytic degradation rate for RhB than that of the pure g-C_3N_4 (0.0113 min^{-1}), $SrTiO_3$ (0.0038 min^{-1}), and N-doped $SrTiO_3$ (0.0135 min^{-1}) under visible light.

There are a few studies on nanocomposites of g-C_3N_4 with Group V metals for the noble-metal-free photodegradation

reactions. Liu et al. prepared a heterojunction of ∼5 nm sized spherical nanoparticles of V_2O_5 with lamellar g-C_3N_4 by simple one-pot synthesis [130]. Rhodamine B was almost completely removed over the optimized nanocomposite for 80 min illumination of visible light. And for the same time of illumination, pristine g-C_3N_4 and V_2O_5 showed less than 10% photodegradation efficiency. Kumar et al. prepared a hybrid nanocomposite of $NaTaO_3$ nanoparticles of ∼43 nm with g-C_3N_4 by a facile ultrasonic dispersion method [131]. Under both UV–vis and visible light, the nanocomposite exhibited highly enhanced photodegradation of RhB compared with pure g-C_3N_4, $NaTaO_3$, and TiO_2 P25. Photodegradation efficiency was almost 100% in 90 min illumination of full light, however, it reached only ∼90% under visible light only even for twofold time of illumination. Yong et al. also used ultrasonic-assisted method for fabrication of a similar nanocomposite of ∼30 nm sized nanoparticles of $KTaO_3$ with g-C_3N_4 [132]. In comparison with pure materials, the optimized nanocomposite demonstrated enhanced photocatalytic degradation of RhB, under visible light irradiation.

For the development of a noble-metal-free photocatalyst, MoS_2 is emerging as an economical alternative co-catalyst. A nanocomposite of MoS_2 nanoparticles onto g-C_3N_4 nanosheets was fabricated by a low-temperature hydrothermal method [133]. The nanocomposite demonstrated much-enhanced photodegradation of MO under simulated solar light. Li et al. coupled nanosheets of MoS_2 with g-C_3N_4 via a facile ultrasonic method for constructing a visible light active photocatalyst [134]. The rate of photodegradation of RhB over the optimized heterostructure reached 0.301 min^{-1} which was 3.6 times higher compared with pure g-C_3N_4.

Li et al. used solvothermal method for the construction of heterojunction between irregular nanoparticles of Bi_2MoO_6 and g-C_3N_4 [135]. In comparison with pure Bi_2MoO_6 and g-C_3N_4 the optimized composite exhibited enhanced photodegradation efficiency for RhB and MB under visible light. After 70 min of irradiation, optimized heterojunction exhibited about 98% photodegradation of RhB while pure g-C_3N_4 or Bi_2MoO_6 showed less than 60% removal. Around the same time, Tian et al. also prepared heterojunction of Bi_2MoO_6 nanosheets with g-C_3N_4 via a solvothermal route [136]. The optimized composite was highly efficient for visible-light-driven degradation of MO and 2,4-dichlorophenol. The composite demonstrated more than 3 times faster photodegradation of MO compared with pure g-C_3N_4 or Bi_2MoO_6. A ternary composite of MoS_2 nanosheets of ∼5 nm thickness, graphene oxide and g-C_3N_4 was prepared using a facile sonochemical method for visible active photocatalysis [137]. The ternary composite exhibited enhanced photodegradation of RhB compared with binary composites and pure g-C_3N_4.

Visible-light-driven WO_3 (bandgap 2.7 eV) and its modified materials have many potential applications in photocatalysis. Huang et al. prepared composite of 100–200 nm sized nanoparticles of WO_3 with g-C_3N_4 by a calcination method for the fabrication of a visible light active photocatalyst [138]. The heterojunction exhibited an enhanced photodegradation efficiency for MB and 4-chlorophenol. The optimized composite showed 97% degradation of MB within 2 h and 43% degradation of 4-chlorophenol within 6 h. Under the same conditions, pure g-C_3N_4 reached only 81% degradation of MB and 3% degradation of 4-chlorophenol. Katsumata et al. prepared composite of WO_3 particles of 100–300 nm with g-C_3N_4 by mechanical mixing in an agate mortar [139]. The composite was used for visible-light-driven degradation of gas-phase acetaldehyde. A complete degradation was achieved on the optimized composite with the highest generation of CO_2. Contrary to the other studies, Chen et al. illustrated on the formation of Z-scheme between ∼30 nm WO_3 and g-C_3N_4 via ball milling and heat treatment [140]. The optimized Z-scheme photocatalyst was highly efficient for visible-light-driven degradation of MB and fuchsin. The rate constants for photodegradation of MB and fuchsin over the optimized composite were 4.8 times and 3.8 times higher than that of the pristine g-C_3N_4.

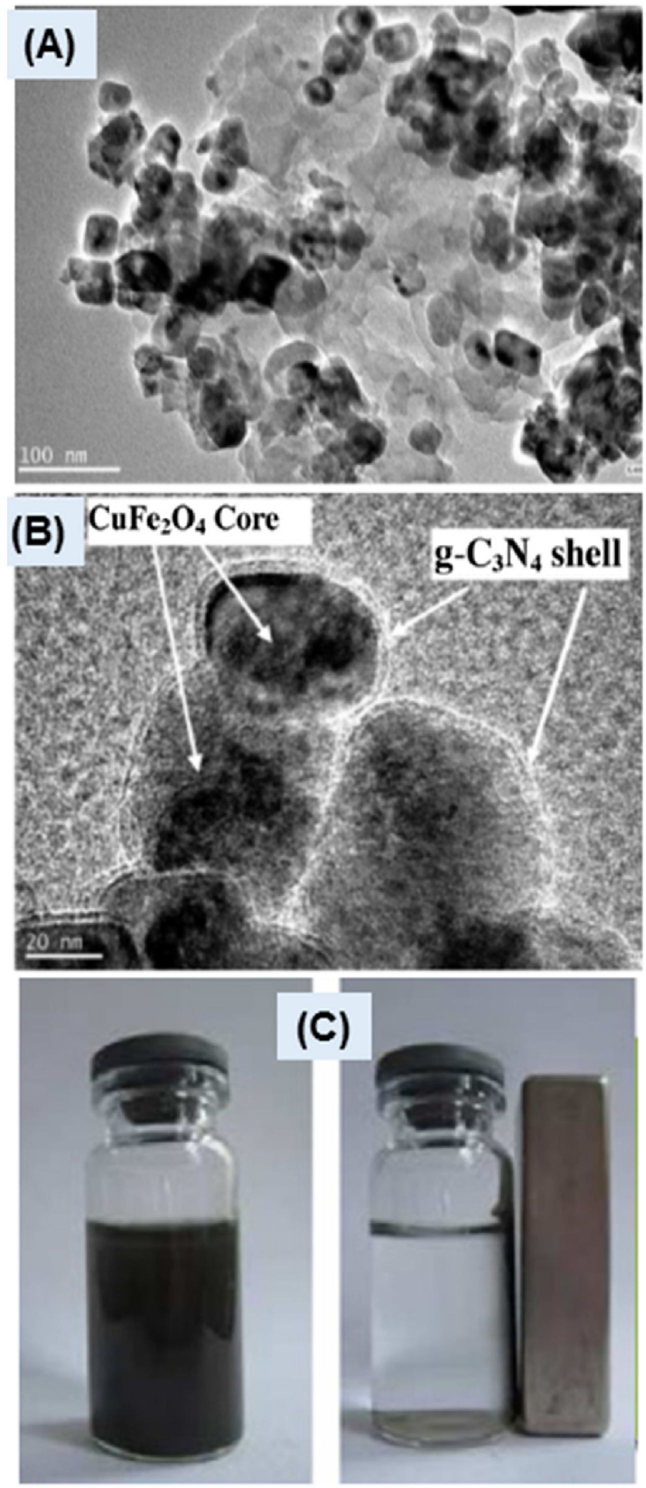

Fig. 15. (A) TEM image of the core–shell structure of $CuFe_2O_4$@g-C_3N_4 (2:1) hybrid, (B) HR-TEM of the hybrid clearly showing the core–shell structure, and (C) Separation of solid and solvent phases using an external magnet.
Reproduced with permission from the Ref. [147]. Copyright (2015) Elsevier.

W-based multi-metal materials are important semiconductors for photocatalysis and their hybridization with g-C_3N_4 also shall be interesting. Wang et al. hybridized $ZnWO_4$ nanorods of 60 × 30 nm by enwrapping with g-C_3N_4 via a facile chemisorption method

[141]. The optimized composite was highly efficient for the photodegradation of MB under both UV and visible light irradiations. Besides a dramatic enhancement of photocatalytic activity under visible light about 80% increase was observed under UV irradiation. Zhan et al. prepared films from the same type of composite and used it for degradation of phenol under UV irradiation [142]. The photodegradation efficiency of optimized composite was ~2 times of the pure $ZnWO_4$. Tian et al. prepared heterojunction of 50–100 nm sized $CdWO_4$ nanorods with g-C_3N_4 by a simple mixing and calcination method [143]. The optimized composite was highly active for photodegradation of RhB under visible light irradiation. Comparatively, the rate of reaction was 1.6 and 54.6 times higher than that of pure g-C_3N_4 and $CdWO_4$.

Fe-based materials are getting attention for photocatalysis, especially for their magnetic separation in sustainable applications. Vignesh et al. prepared a ~19 nm ternary magnetic nanocomposite from TiO_2, $MnFe_2O_4$ and g-C_3N_4 via chemical impregnation method [144]. The optimized ternary composite was highly efficient for photodegradation of MO under simulated solar light. For 3 h illumination, $MnFe_2O_4$/g-C_3N_4/TiO_2 exhibited 99.3% degradation while binary composite, $MnFe_2O_4$/g-C_3N_4 (4.9%) and pure materials, $MnFe_2O_4$ (4.2%), g-C_3N_4 (43.7%), and TiO_2 (85.1%) showed inferior performance. Zhu et al. prepared a nanocomposite of highly dispersed Fe_3O_4 nanoparticles of 5–10 nm onto g-C_3N_4 by ultrasonic-assisted wet chemical method [145]. Magnetic conductive imprinted photocatalysts (MCIPs) were prepared from the nanocomposite support and organic template and functional monomer. MCIPs were employed for photodegradation of 2-mercaptobenzothiazole (MBT) under visible light irradiation. The optimized MCIP exhibited highly enhanced (~85%) photodegradation of MBT in 60 min compared with pure g-C_3N_4 (40%). A simple impregnation method was used by Liu et al. for grafting 20–50 nm nanoclusters of Fe^{3+} species onto the surface of g-C_3N_4 [146]. Furthermore, a ternary composite was prepared with the addition of graphene for enhanced visible-light-driven degradation of MO. The photodegradation reaction rate constant of the optimized composite was 0.0276 min^{-1} which was about 2 and 11 times higher than that of the binary composite and pure g-C_3N_4.

A novel core–shell structure of magnetic $CuFe_2O_4$@g-C_3N_4 was fabricated through a self-assembly method by Yao et al. [147]. TEM image depicted that after hybridization the $CuFe_2O_4$ nanoparticles in the range of 50–60 nm were well interwoven among the g-C_3N_4 (Fig. 15A). Formation of core–shell structure was shown by the HR-TEM analysis, the $CuFe_2O_4$ nanoparticles were encapsulated within the films of g-C_3N_4 (Fig. 15B). The thickness of the g-C_3N_4 shell was in the range of 5–7 nm. In comparison with the pure semiconductors, the hybrid structure demonstrated an excellent photo-Fenton-like catalytic activity for the decolorization of an organic dye, Orange II. Magnetic $CuFe_2O_4$@g-C_3N_4 with 2:1 was found the best photocatalyst which decomposed ~98% of organic dye within 210 min of visible light irradiation. The physical separation of the composite from the solution with an external magnet is depicted in Fig. 15C which illustrated an easy recycling of the catalyst material.

Zhang et al. decorated nanoparticles of spinel $ZnFe_2O_4$ (ZnFe) on g-C_3N_4 (CN) sheets through a one-step solvothermal route [148]. Superior visible active photocatalytic properties of the nanocomposite were ascribed to the effective separation of photogenerated charges and to its high dispersion in water. An optimized heterojunction was obtained for the 160CN-ZnFe sample prepared from the Fe precursor to g-C_3N_4 ratio of 2:1. Fig. 16A revealed the distribution of optimized 5–6 nm nanoparticles of $ZnFe_2O_4$ attached to g-C_3N_4 sheets. The magnetic properties were effectively controlled by tuning the coverage and size of the spinel oxide (Fig. 16B). The optimized composite demonstrated an extremely high visible light photodegradation activity towards MO and phenol comparing with individual semiconductors. The optimized composite demonstrated ~98% decomposition of MO in 180 min while the photocatalytic activity of pristine g-C_3N_4 (36%) and $ZnFe_2O_4$ (44%) was very low. Furthermore, a low photocatalytic activity of a physical mixture indicated the importance of well-connected interface between semiconductors. The curves for visible-light-driven degradation of phenol are depicted in Fig. 16C. The enhanced photocatalytic activity of the composite was ascribed to effective separation of electron-hole pairs on nanojunctions. Recyclability of the optimized catalyst for the degradation of MO showed a slight decrease in the activity (Fig. 16D).

ZnO is an important semiconductor but poorly responsive to visible light and suffers from high recombination of photogenerated charges. Fabrication of heterojunction between ZnO and g-C_3N_4 is interesting for their appropriate band potentials in enhancing separation of electron-hole pairs. Chen et al. used a facile solvothermal route for the fabrication of heterojunction between 10 and 30 nm sized nanospheres of ZnO and mesoporous g-C_3N_4 [149]. The composite structure was employed for photodegradation of MB under visible light and simulated solar irradiation and was found efficient. In comparison with pure g-C_3N_4 mesoporous the photocatalytic activity was 2.3 and 1.9 times higher under visible light and solar irradiation. Vignesh et al. used mesoporous ZnO nano-triangles of 50–60 nm size for construction of a nanocomposite with g-C_3N_4 nano-foils through a sonochemical impregnation method [150]. The heterojunction structure exhibited highly efficient degradation of RhB under solar light irradiation and remained stable in cycling tests. The optimized nanocomposite demonstrated 100% removal within 60 min that was faster than pure g-C_3N_4 and ZnO nano-triangles. In addition to ZnO, nanoparticles of multi-metal oxide, Zn_2SnO_4 was also coupled with g-C_3N_4 for enhanced visible-light-driven photoactivity. Zhang et al. synthesized the composite Zn_2SnO_4/g-C_3N_4 from heating a mixture of Zn_2SnO_4 and melamine [151]. Formation of heterojunction promoted the separation of photogenerated charges and thus enhanced the degradation of RhB under visible light irradiation. The reaction rate constant of 0.038 min^{-1} was exhibited by the optimized composite which was 3.2 and 38 times higher than the rates of pure g-C_3N_4 and Zn_2SnO_4, respectively.

The synthesis of a novel ternary composite of ZnO nanoparticles, g-C_3N_4 and GO was systematically studied for enhanced visible-light-driven photocatalysis [152]. A schematic of the co-precipitation and calcination process employed for the synthesis of nanoparticles and composites is provided in Fig. 17A. The ternary composite with a spherical ZnO nanoparticles of 5–10 nm size evenly embedded in the porous g-C_3N_4 was obtained by this method as shown in the TEM image (Fig. 17B). A drastic quenching of photoluminescence intensity for the ternary composite indicated successful hybridization of the components. The optical spectra showed that absorption of the visible-light was significantly enhanced in the ternary composites (Fig. 17C). The optimum content of 50% g-C_3N_4 in the binary composite, ZnO/g-C_3N_4 exhibited effective hybridization and a high photocatalytic efficiency. However, performance of the ternary composite was two times faster than that of the ZnO/g-C_3N_4. The optimized ternary composite exhibited more than 99% degradation of MB in just 15 min under visible-light irradiation, and the photocatalytic activity was maintained in the repeated runs.

CdS and multi-metal sulfides with Cd are fascinating visible-light-driven photocatalyst materials, however their photo-corrosion under working conditions is a serious issue. Coupling of Cd-based sulfides with g-C_3N_4 is interesting for enhanced photocatalysis and stability of the system. CdS nanoparticles with 10–30 nm size were randomly distributed on g-C_3N_4 sheets via an in-situ precipitation-deposition method [153]. This novel inorganic-organic composite demonstrated high activity and

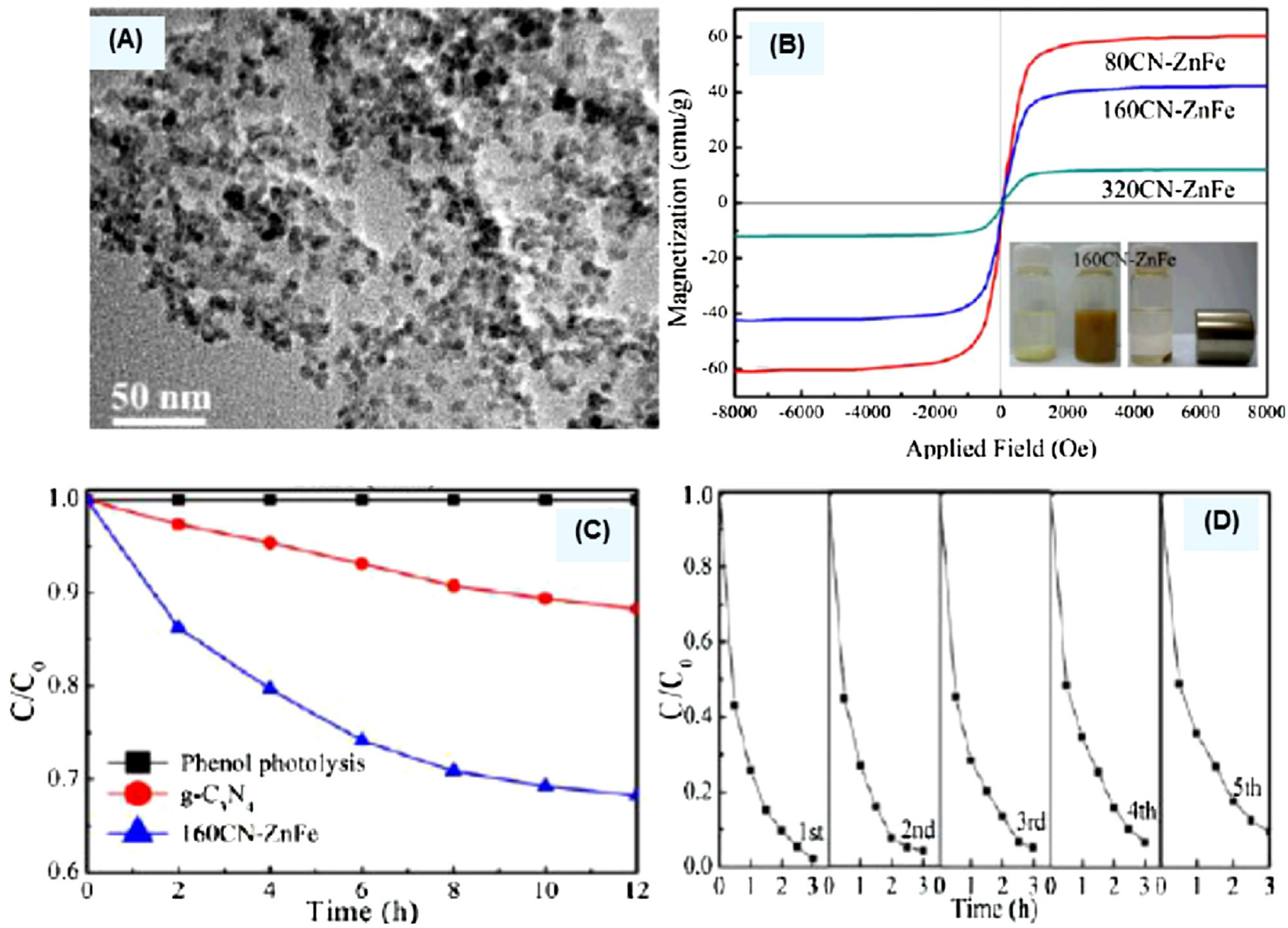

Fig. 16. (A) TEM image of g-C_3N_4-$ZnFe_2O_4$ (CN-ZnFe) composite, (B) Magnetization curves of the composites. Inset in (B) shows the composite with a stable, brown aqueous dispersion and easy separation by a magnet. (C) Photocatalytic degradation of phenol over pure g-C_3N_4 and the optimized composite, and (D) Cycling runs for the photocatalytic degradation of MO over the optimized nanocomposite under visible-light irradiation.

stability for degradation of MO and 4-aminobenzoic acid under visible light irradiation. In comparison with pure g-C_3N_4 (and CdS) the photocatalytic activity was 20.5 (3.1) and 41.6 (2.7) times higher for the degradation of MO and 4-aminobenzoic acid, respectively.

Cui et al. used hydrothermal methods for the fabrication of heterojunction between ~30 nm $Zn_{0.8}Cd_{0.2}S$ and g-C_3N_4 [154]. The composites were prepared using various ratios of Zn/Cd and found highly active for degradation of RhB compared with pure g-C_3N_4 and $Zn_{1-X}Cd_XS$, under visible light. For 90 min of illumination, ~98% of the organic dye was removed over the optimized composite while only about 73% removed on an individual component, pure $Zn_{0.8}Cd_{0.2}S$. Lately, Tian et al. used the same multi-metal sulfide, $Zn_{0.8}Cd_{0.2}S$ with a uniform diameter of ~10 nm and constructed a heterojunction with P-doped g-C_3N_4 via ultrasonic-assisted in-situ precipitation method [155]. The composite was highly active for the removal of MB under simulated sunlight. Photocatalytic degradation efficiency of pure $Zn_{0.8}Cd_{0.2}S$, 56% increased to ~64% upon the construction of heterojunction with g-C_3N_4 and further increased to more than 93% with P-doped g-C_3N_4.

Reduced graphene oxide is known for a crucial role in the effective separation of photogenerated electron-hole pairs. Pawar et al. prepared a ternary composite of CdS, rGO, and g-C_3N_4 using a facile chemical method [156]. TEM and HR-TEM images of the ternary composite in Fig. 18A and B show the presence of rGO sheets and CdS nanoparticles of ~40 nm size attached to g-C_3N_4. As shown in magnified TEM, CdS nanoparticles were sporadically coated onto g-C_3N_4 and rGO sheets. Spectroscopic characterizations further confirmed the construction of strong contacts in between the components of the composite for extended absorption of visible light and enhanced separation of photogenerated electron-hole pairs. Consequently, the ternary composite exhibited superior photodegradation of RhB and Congo red under both UV and visible light irradiations. The results for cyclic photodegradation of RhB showed a stable performance of the composite (Fig. 18C). A schematic of the composite for an improved photocatalytic performance which was attributed to a reduction in the recombination of electron-hole pairs as well as increased absorption is presented in Fig. 18D.

2.8.3. Post-transition metal based system

Post-transition metal based semiconductor nanomaterials mainly that of Bi, Sn, and In were coupled with g-C_3N_4 for the development of efficient photocatalyst systems. Ge et al. prepared 10–30 nm sized agglomerated nanocomposites of g-C_3N_4 and Bi_2WO_6 by calcination [157]. Photocatalytic activity of the heterostructure was evaluated by degradation of MO under visible light irradiation. For the optimized heterojunction, the rate of degradation was 0.0365 min^{-1} which was about 4 and 48 times higher than that of the pure g-C_3N_4 and Bi_2WO_6, respectively. Liu et al. worked on the similar photocatalyst system of g-C_3N_4 and Bi_2WO_6 for the construction of a core-shell structure [158]. Uniform nanospheres of Bi_2WO_6 with an average size of 30–40 nm were coated with ultrathin nanosheets of g-C_3N_4 by ultrasonication-chemisorption method. The optimized composite

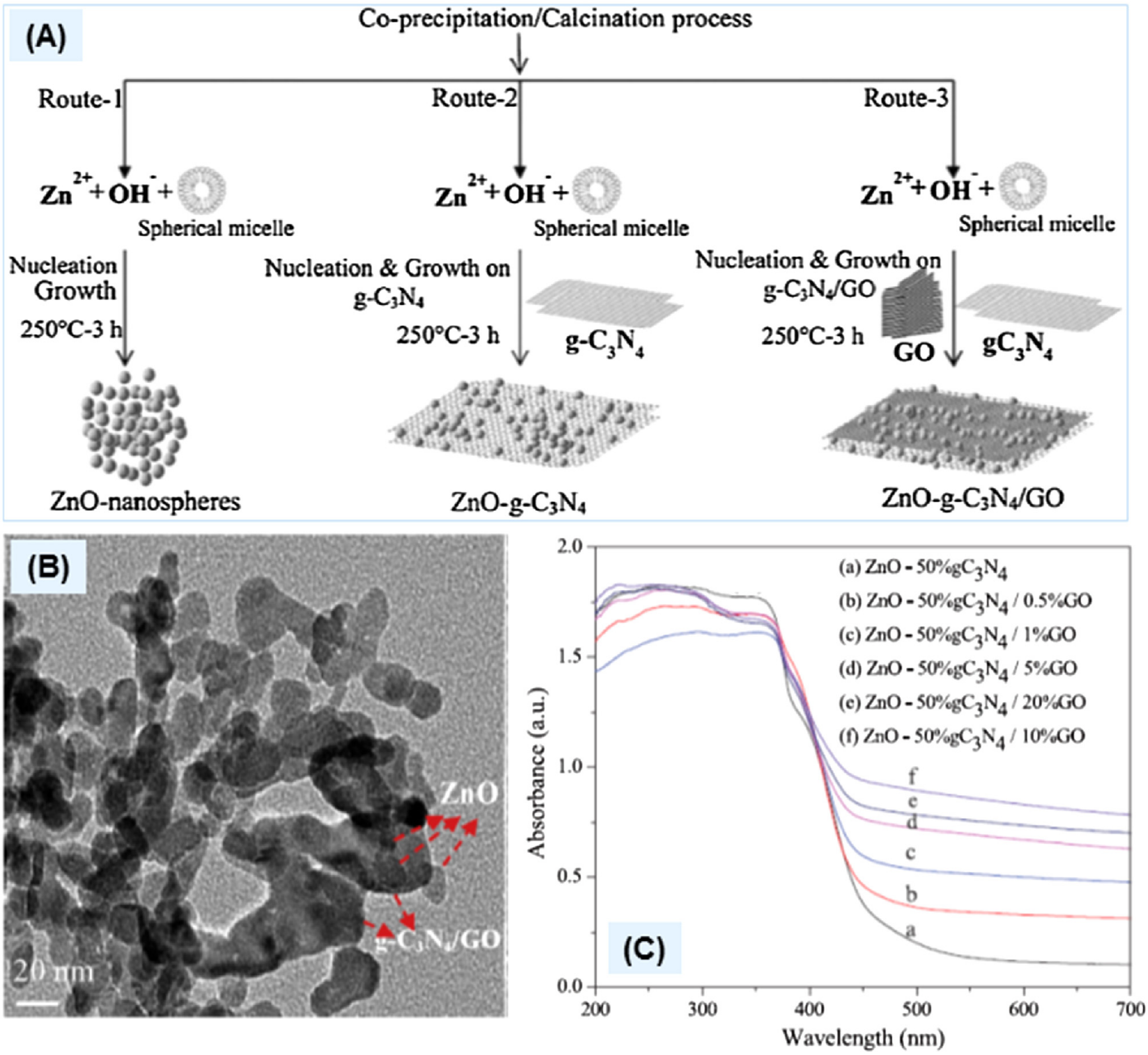

Fig. 17. (A) Formation mechanism for the nanostructures of ZnO and g-C_3N_4, (B) TEM image of ZnO loaded on g-C_3N_4, and (C) UV-vis spectra for the various nanostructures. Reproduced with permission from the Ref. [152]. Copyright (2015) Elsevier.

structure exhibited significantly enhanced degradation of MB, RhB, MO, and phenol, under visible light irradiation. The rate constant for MB degradation over the optimized core-shell structure reached as high as 0.0814 min^{-1}.

$BiPO_4$, an oxoacid salt photocatalyst was also used for modifications with g-C_3N_4 for noble-metal-free reactions. Pan et al. coated $BiPO_4$ nanorods of 80 nm by 400 nm size with various levels of thickness of g-C_3N_4 from less than 5 nm to 30 nm via a facile ultrasonic dispersion method [159]. Self-assembled core-shell heterojunction was highly efficient for the degradation of MB under UV light irradiation. The optimized core-shell structure exhibited a very high rate constant of 0.4701 min^{-1} that was 2.5 and 4.5 times higher compared with that of the pure $BiPO_4$ and TiO_2 P25, respectively. Obregon et al. further modified $BiPO_4$ and g-C_3N_4 composite with the addition of TiO_2 [160]. The complex ternary heterostructure of ~12 nm TiO_2 and 70–90 nm $BiPO_4$ with g-C_3N_4 was prepared by a simple impregnation method. The ternary composite with a cascade charge separation mechanism demonstrated enhanced degradation of organic pollutant, under solar-like irradiation. The optimum rate for the degradation of phenol was 1.5 times higher with respect to pure TiO_2.

Bismuth oxyhalides (BiOX) are interesting materials for their excellent electrical and optical properties resulting from their unique layered structure. Construction of heterojunctions of BiOX and g-C_3N_4 has resulted in enhanced photocatalytic properties under visible light irradiation. Yang et al. prepared heterojunctions by the in-situ growth of less than 50 nm thick nano-flakes of BiOBr on the surface of protonated g-C_3N_4 [161]. The nanocomposite was evaluated for the degradation of RhB under visible light irradiation. Photodegradation reaction rate constant for the optimized heterojunction reached to extremely high value of 0.3608 min^{-1} which was about 35 and 34 times higher compared with individual protonated g-C_3N_4 and BiOBr, respectively. Xia et al. constructed layered nanojunctions from in-situ grown ultrasmall 6 nm thick nanosheets of $Bi_4O_5I_2$ uniformly dispersed on ultrathin g-C_3N_4 via a facile solvothermal method in the presence of a reactable ionic liquid that provided iodide [162]. The nanostructure displayed much higher photocatalytic activity for the degradation

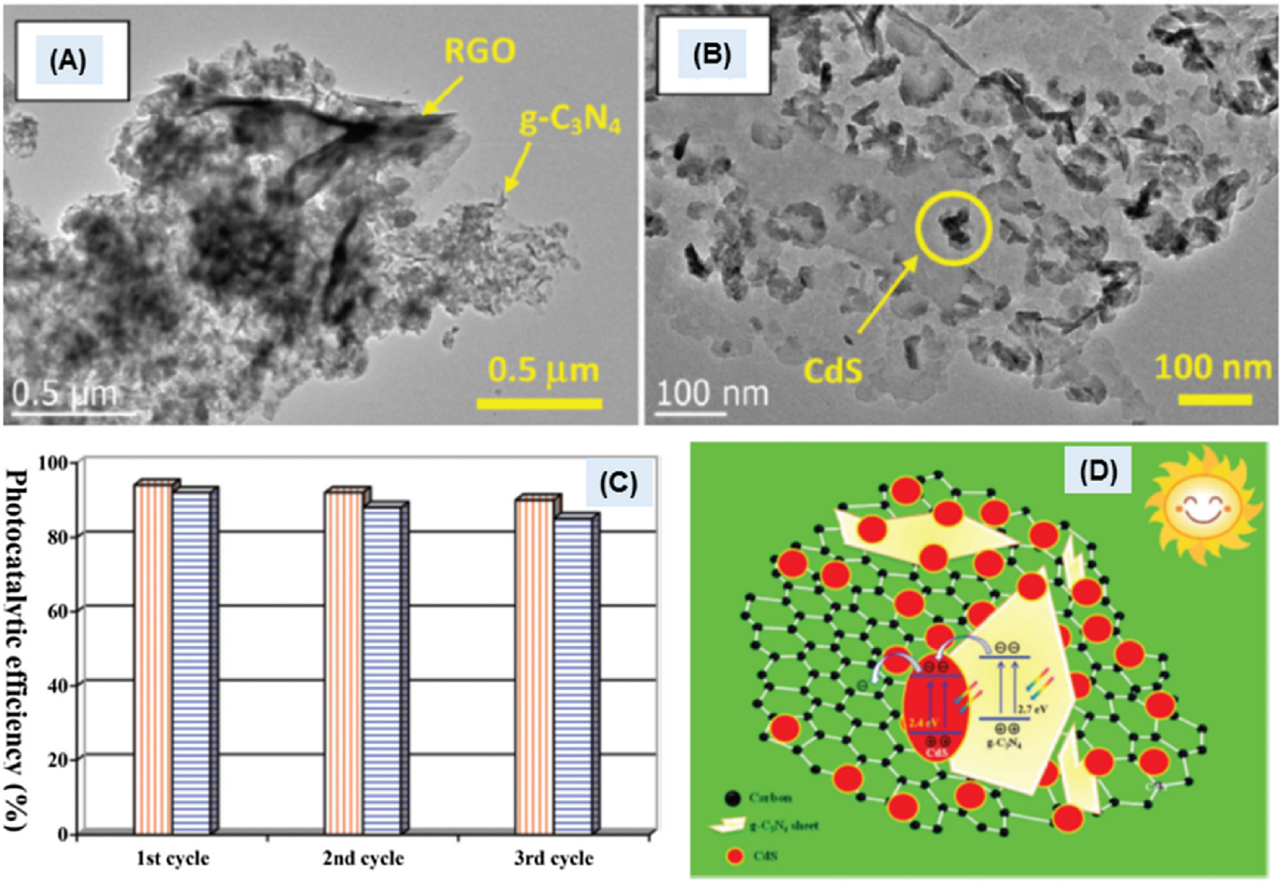

Fig. 18. (A) TEM image of ternary composite of CdS, rGO and g-C_3N_4, (B) TEM image showing CdS nanoparticles on g-C_3N_4 sheets, (C) Cycling runs for the photocatalytic degradation of an organic dye, RhB over the optimized nanocomposite under visible-light (bars with vertical red lines) and UV (bars with horizontal blue lines) irradiation, and (D) Scheme for electron–hole separation and transport towards visible-active degradation over the nanocomposite. (For interpretation of the references to colour in this figure legend, the reader is referred to the web version of this article.)

Reproduced with permission from the Ref. [156]. Copyright (2014) Royal Society of Chemistry.

of RhB and a colorless endocrine disrupting chemical bisphenol A, under visible light irradiation. Over the optimized nanostructure ~70% of RhB was effectively removed in 60 min while pure $Bi_4O_5I_2$ removed only 31%. And in 20 min, bisphenol A degradation efficiency of the layered nanojunction reached to 90% but only 35% was degraded on pristine $Bi_4O_5I_2$. Yuan et al. developed a complex ternary composite from two ternary bismuth compounds BiOI rounded sheets of 50–150 nm and BiOBr quadrate sheets of 200–500 nm with g-C_3N_4 by a facile solvothermal method [163]. The composite was highly efficient for visible-light-driven degradation of MB. The photodegradation rate constant over the optimized composite (0.0113 min^{-1}) was 2.5 and 3.2 times higher than that of pristine g-C_3N_4 and BiOI/BiOBr, respectively.

Like TiO_2 and ZnO, SnO_2 is a traditional wide band gap semiconductor activated by UV light only. Both conduction and valence band positions of SnO_2 are suitable for construction of effective heterojunction with g-C_3N_4. Yin et al. synthesized a nanocomposite of extremely fine 2–3 nm size nanoparticles of SnO_2 evenly dispersed on g-C_3N_4 by ultrasonication [164]. In comparison with pristine g-C_3N_4 and SnO_2, the optimized heterojunction was highly active for the degradation of MO under visible light. Chen et al. also worked on the same photocatalyst system, a heterojunction of SnO_2 and g-C_3N_4 [165]. Aggregated nanoparticles of SnO_2 were in-situ grown onto the surface of g-C_3N_4 nanosheets via a hydrothermal route. The nanocomposite was evaluated for photocatalytic degradation of MO under visible light irradiation. The optimum photodegradation efficiency of the heterojunction was 17 and 89 times higher compared with that of the pure g-C_3N_4 and SnO_2.

In_2S_3 (bandgap ~2.2 eV) is an *n*-type semiconductor which is widely used in harvesting solar energy. Therefore it is a good choice for modifying g-C_3N_4 towards its noble-metal-free photocatalytic applications. Xing et al. constructed g-C_3N_4 and In_2S_3 heterojunction via a hydrothermal method [166]. The nanocomposite structure exhibited higher photocatalytic activity than those of the pure g-C_3N_4 and In_2S_3. TEM image of g-C_3N_4 nanosheets decorated with In_2S_3 nanoparticles is presented in Fig. 19A indicating the formation of heterojunctions. Detailed investigations by TEM microscopy illustrated on the formation of an intimate interface between the semiconductors, which was favorable for the separation of photogenerated charge carriers. Optical spectra of the nanocomposites showed their good prospects for their photoactivity in the visible region. Consequently, the nanocomposite heterojunction exhibited higher efficiency for photodegradation of RhB, 96% degradation in just 30 min. The visible light active photocatalytic process is illustrated in the schematic (Fig. 19B). Photocatalytic activity of the heterojunction was higher than the bare materials and that of the physical mixture.

Li et al. used amorphous particles of this earth-abundant Al_2O_3 as an electron acceptor in the heterostructure with g-C_3N_4 [167]. A composite of amorphous Al_2O_3 with lots of defect sites was constructed with surface hydroxyl modified g-C_3N_4 through ultrasonic dispersion method. Photocatalytic properties of the composite were evaluated by degradation of RhB, under visible light irradiation. The reaction rate constant for the optimized composite with amorphous Al_2O_3 reached 0.0257 min^{-1} which was 9.2 times higher in comparison to the composite with γ-Al_2O_3. Furthermore,

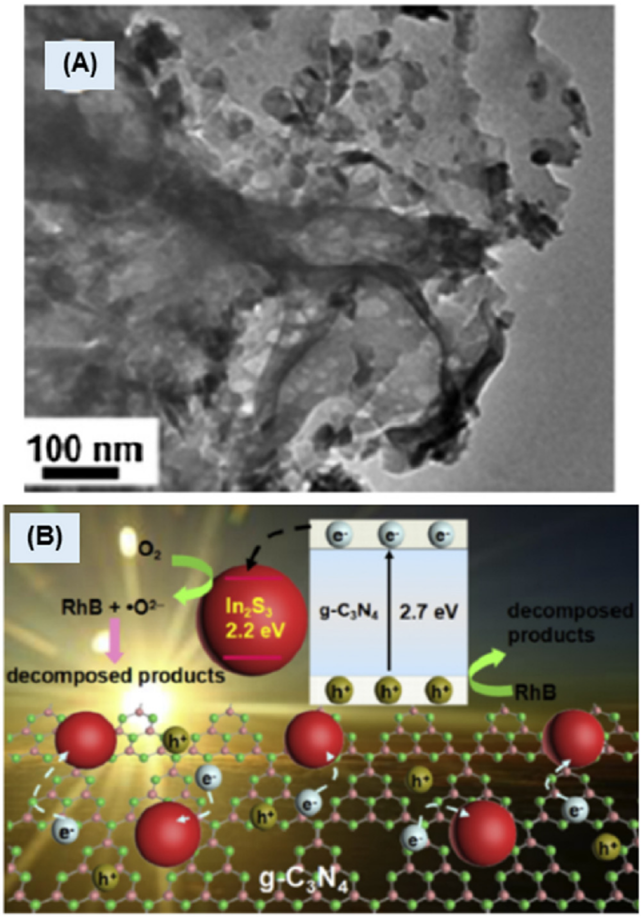

Fig. 19. (A) TEM image of the In_2S_3 and $g\text{-}C_3N_4$ composite, and (B) Schematic illustration of the photocatalytic reaction process over the composite material. Reproduced with permission from the Ref. [166]. Copyright (2014) Elsevier.

the composite prepared via hydroxyl modified route was 3.8 times more efficient compared with the composite prepared without surface modification of $g\text{-}C_3N_4$. Hence, both surface modification of and use of amorphous Al_2O_3 was important for the construction of a visible-light-driven photocatalyst.

2.8.4. Semimetal based systems

A few researchers studied nanocomposites of $g\text{-}C_3N_4$ with semimetal materials for photocatalytic applications. Wang et al. coated spherical SiO_2 nanoparticles of less than 50 nm with in-situ grown $g\text{-}C_3N_4$ by calcination of melamine [168]. In comparison with pure $g\text{-}C_3N_4$, a high BET surface area and mesoporous structure of the composite was found important for photodegradation of RhB. The optimized composite structure showed 99.9% removal of organic dye after 90 min of visible light irradiation. The rate constant for optimized composite ($0.051\ min^{-1}$) was 2.3 times higher compared with that of the pure $g\text{-}C_3N_4$. Lin et al. prepared similar type core-shell nanosphere for an enhanced visible-light-driven degradation of RhB [169]. Relatively large, 200–300 nm SiO_2 nanospheres derived from tetraethyl orthosilicate were coated with cyanamide and followed by heating in N_2 atmosphere. The optimized core-shell composite depicted more than 94% degradation of RhB which was ~3.5 times higher compared with pristine $g\text{-}C_3N_4$.

Antimony and boron modified $g\text{-}C_3N_4$ nanomaterials were also considered for photocatalytic applications. Wen et al. constructed a heterojunction between 45 nm sized $HSbO_3$ and $g\text{-}C_3N_4$ by heating in N_2 atmosphere [170]. The nanocomposite was highly efficient for visible-light-driven degradation of RhB. The optimized heterojunction demonstrated almost complete removal of organic dye within 6 h while pure $g\text{-}C_3N_4$ showed less than 50% removal. Lately, Wang et al. synthesized heterostructure of sheaf-like Sb_2S_3 rods (100–500 nm) and ultrathin $g\text{-}C_3N_4$ sheets embedded with $g\text{-}C_3N_4$ quantum dots (less than 10 nm) [171]. The composite structure was active for photodegradation of MO under near-IR irradiation. The rate of degradation for the optimized composite was $0.0103\ min^{-1}$ which was 2.6 times higher compared with pure Sb_2S_3.

2.8.5. Rare earth metals based system

Modifications of $g\text{-}C_3N_4$ with rare earth metal based materials were studied for the construction of efficient photocatalyst systems. Among rare earth metals, Ce based photocatalysts are the most interesting candidates. Luo et al. prepared a nanocomposite of 10–20 nm nanoparticles of CeO_2 with P-doped $g\text{-}C_3N_4$ by facile mixing-calcination route [172]. The heterojunction was used for the degradation of MO under visible light irradiation. Photodegradation efficiency of the optimized composite with rate constant $0.011\ min^{-1}$ was more than 12 and 5 times higher compared with that of the pure CeO_2 and P-doped $g\text{-}C_3N_4$, respectively. Wang et al. used ultrasonic-heat treatment method for construction of a ternary composite of CeO_2 nanorod, $g\text{-}C_3N_4$ and N-doped reduced graphene oxide [173]. Visible-light-driven rate for the degradation of RhB over the ternary composite ($0.025\ min^{-1}$) was 2.1 fold higher than that of the binary composite of $g\text{-}C_3N_4$ and N-doped rGO.

Controllable synthesis of CeO_2 and $g\text{-}C_3N_4$ nanocomposite via a facile hydrothermal method was investigated by She et al. [174]. TEM image in Fig. 20A shows ultrafine 3–10 nm nanocubes of CeO_2 closely bonded with $g\text{-}C_3N_4$. XRD patterns depicted an increase in the intensity of CeO_2 peaks with an increase in its contents in the nanocomposite (Fig. 20B). Furthermore, changes in the diffraction peak positions further emphasized on the attachment between the two components of the composite. Photocatalytic degradation of MB under visible light was significantly improved over the nanocomposites with all the various ratios (Fig. 20C). The optimized nanocomposite with 5% CeO_2 demonstrated 99% efficiency in 3.5 h and showed a small decrease in recycling tests.

Many of the vanadates of rare earth metals are suitable semiconductors for fabrication of heterojunctions with $g\text{-}C_3N_4$ towards their visible-active photocatalytic applications. He et al. constructed a heterojunction between 50 nm sized nanoparticles of $DyVO_4$ and $g\text{-}C_3N_4$ by a milling and heating treatment method [175]. The composite was tested for visible-light-driven degradation of RhB and MB. The optimized heterojunction exhibited the highest rate ($0.0365\ min^{-1}$) of rhodamine degradation which was 2.6 and 10.3 times higher compared with pure $g\text{-}C_3N_4$ and $DyVO_4$, respectively. A composite of finely dispersed $SmVO_4$ nanoparticles of 30–60 nm on the surface of $g\text{-}C_3N_4$ was prepared by a simple mixing-calcination method [176]. The optimized heterostructure showed a significantly enhanced degradation of RhB under visible light irradiation. The rate of degradation for the optimized heterojunction reached to $0.0345\ min^{-1}$ and that was 2.4 and 6.3 times higher than that of the pure $g\text{-}C_3N_4$ and $SmVO_4$, respectively. He et al. used two polymorphs of $LaVO_4$ namely tetragonal (t) and monoclinic (m) with different optical properties for the construction of heterostructures with $g\text{-}C_3N_4$ by calcination method [177]. In the heterojunctions, particles of t-$LaVO_4$ appeared as ~10×50 nm nanorods while relatively larger sized different shapes like rods, plates and spheres were seen for m-$LaVO_4$ in its composite. Both the $LaVO_4$ polymorphs were almost inactive for the degradation of RhB under visible light irradiation. However, highly efficient photodegradation of rhodamine was observed upon the construction of heterojunctions with $g\text{-}C_3N_4$.

He et al. synthesized composite of $g\text{-}C_3N_4$ with $GdVO_4$ by a milling and heating method [178]. Powder XRD patterns showed

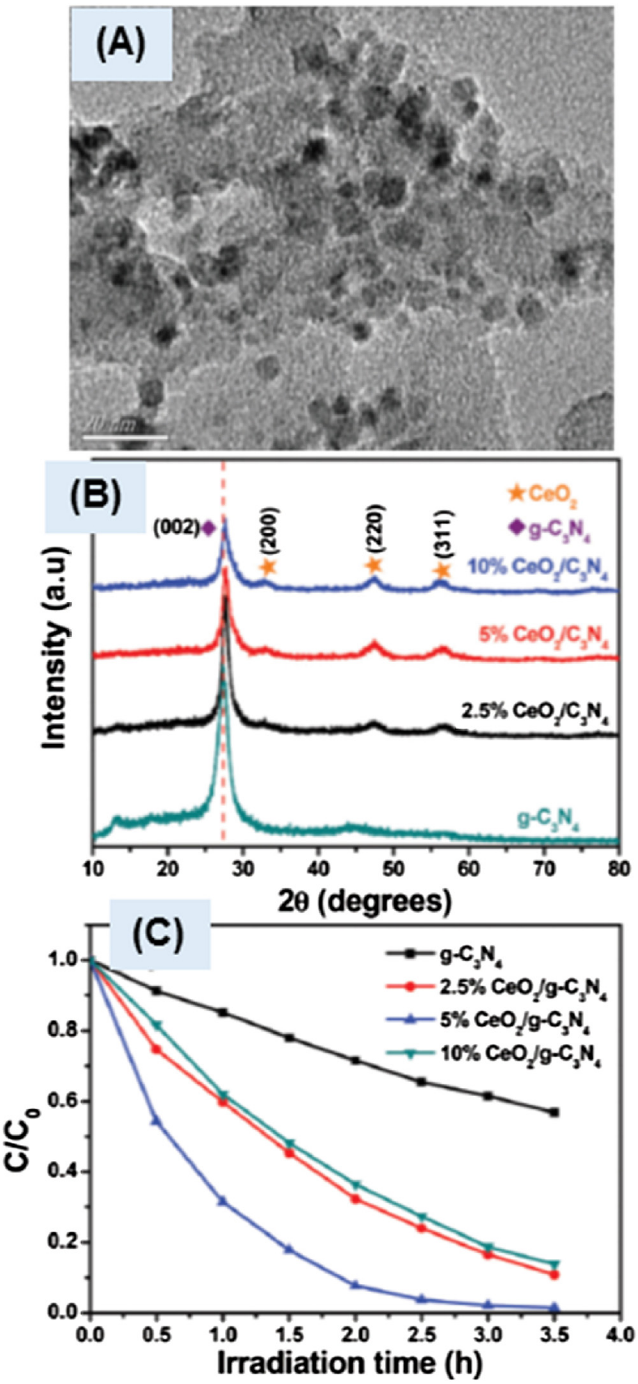

Fig. 20. (A) TEM image of the nanocomposite of 10 wt.% CeO_2 with g-C_3N_4, (B) Powder XRD patterns of g-C_3N_4 and the nanocomposites with various amounts of CeO_2, and (C) Photocatalytic degradation of an organic dye, MB over the as-prepared materials.

(Reproduced with permission from the Ref. [174]. Copyright (2015) Royal Society of Chemistry.

two-phase composite in which diffraction peak intensity for GdVO4 increased with its concentration and at the expense of that of g-C_3N_4 (Fig. 21A). An intimate connection between organic and inorganic semiconductors was seen in the TEM images (Fig. 21B) and confirmed with the quenching of PL intensity for the nanocomposites. Mainly dispersed $GdVO_4$ nanoparticles of 50 nm were present in the TEM image, although some small aggregates were also observed. Under visible light irradiation for 120 min, about 97% degradation of RhB was observed over the optimized nanocomposite (10 wt.% $GdVO_4$) that showed stable performance in repeated cycles (Fig. 21C). The hybrid structure exhibited enhanced photocatalytic activity because of the synergistic effect of the two semiconductors in separation of electron-hole pairs. The band potentials of $GdVO_4$ (2.36 eV) are suitable for the construction of heterojunction with g-C_3N_4 and schematically represented in Fig. 21D and thereby improved the photo-oxidation efficiency.

2.9. Biocide

Visible-light-driven inactivation of bacteria over photocatalyst material is an important application towards environmental remediation. Among a wide variety of materials used for bacterial inactivation, most of the efficient photocatalysts are silver based materials which are unfavorable for green and sustainable application in disinfection. Therefore, development of a metal-free photocatalyst system is particularly interesting for biocide, and this polymeric metal-free semiconductor g-C_3N_4 is an interesting choice. Wang et al. introduced this ternary composite of g-C_3N_4 nanosheets and rGO wrapped on cylooctasulfur (α-sulfur) [179]. The order of wrapping was important in directing the photocatalytic activity of the composite under visible light irradiation. In aerobic conditions, the composite g-C_3N_4/rGO/α-sulfur showed enhanced inactivation of bacteria. However, under anaerobic conditions, the composite rGO/g-C_3N_4/α-sulfur was more active.

Microfiltration is widely used technology for purification of water. However, the size exclusion limitations in removing smaller size contaminants and inherent fouling of the membrane are challenges in microfiltration process. An integrated approach of microfiltration and visible-light-driven photocatalysis was studied by Zhao et al. [180]. A composite of g-C_3N_4 nanosheets and reduced graphene oxide was assembled on the surface of cellulose acetate, a commercial membrane. The integrated process was highly efficient for the removal of various organic contaminants and complete inactivation of bacteria from the surface water comparing with membrane filtration alone. Thurston et al. prepared photoactive antimicrobial films containing metal-free semiconductor, g-C_3N_4 nanosheets [181]. Visible-light-driven production of reactive oxygen species on g-C_3N_4 derived films indicated their potential for antimicrobial activity. The film containing nanosheets of g-C_3N_4 showed biocidal activity against both Gram negative and Gram positive bacteria under visible light irradiation.

2.10. NOx abatement

Nitric oxide (NO) and nitrogen dioxide (NO_2) referred as NO_X, are air pollutants of high environmental concern for their link with acid rain and smog. Various techniques are assessed for NO_X abatement, however, economic feasibility and removal at low concentration are pending issues. Visible-light-driven photocatalytic decomposition of NO_X under sunlight irradiation or in the indoor artificial light presents as an attractive green technology that could purify air from a low concentration of pollutants at ambient conditions.

The research group of Fan Dong has extensively worked on photocatalytic NO_X abatement over g-C_3N_4 based materials. In the year 2013, they synthesized nanoarchitectures of g-C_3N_4 by pyrolysis of urea and used the material for photocatalytic removal of gaseous NO and aqueous RhB under visible light irradiation [182]. The intermediate and highly toxic, NO_2 was monitored in the deNO$_X$ process. Photocatalytic activity of the as-prepared material improved with increased time of pyrolysis of urea, and maximum NO_X removal ratio was 32.1%. A critically very high BET specific surface area, 288 $m^2\,g^{-1}$ was recorded for the optimized nanosheets of g-C_3N_4 which produced the lowest level of NO_2 intermediate. The enhancement of deNOx processes was correlated with

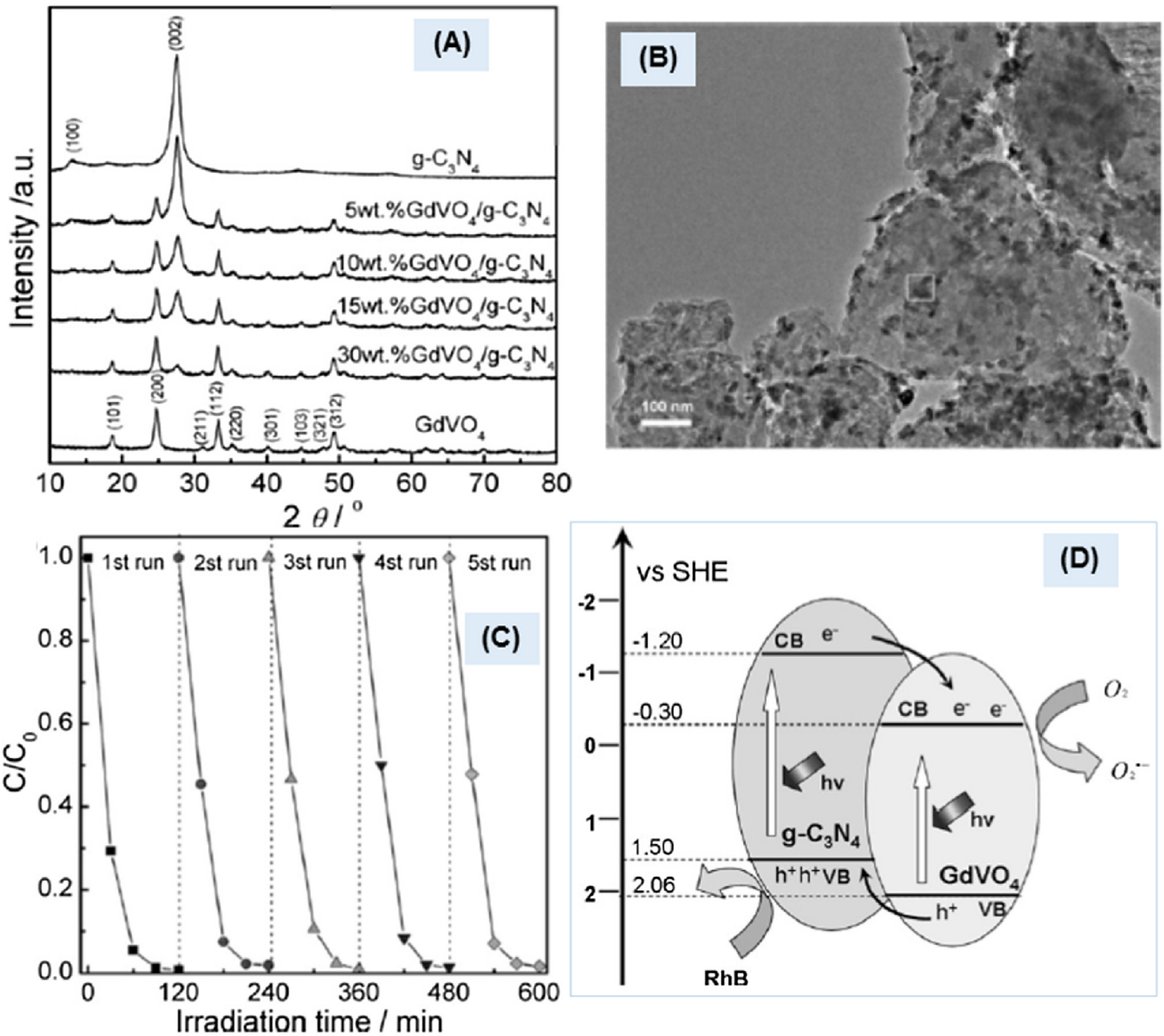

Fig. 21. (A) Powder XRD patterns of $GdVO_4$, g-C_3N_4, and their nanocomposites, (B) TEM image of 10 wt.% $GdVO_4$ loaded on g-C_3N_4, (C) Cycling runs for the photocatalytic degradation of an organic dye, RhB over the optimized nanocomposite under visible-light irradiation, and (D) Scheme for electron–hole separation and transport at the interface of the nanocomposite.

Reproduced with permission from the Ref. [178]. Copyright (2013) Elsevier.

physicochemical properties of the photocatalyst. In another study, they prepared two types of metal-free g-C_3N_4/g-C_3N_4 heterojunctions from dicyandiamide, melamine and urea precursors [183]. However, no significant improvement was observed for NO removal. Yet another approach of high-temperature synthesis of metal-free g-C_3N_4 did not improve the NO removal. And for the nanosheets of g-C_3N_4 synthesized at 600 °C, photocatalytic NO removal ratio was at 32.7% [184]. Porous nanosheets of g-C_3N_4 prepared from thiourea also showed similar performance and NO removal ratio was 33.5% [185]. Zhao et al. optimized the synthesis by altering the precursor mass and found that 'less is better' for the construction of a photocatalytically active g-C_3N_4 [186]. The optimized material exhibited a very high removal ratio of NO at 48.3%, but with a significant formation of NO_2. In another approach, Wang et al. synthesized a honeycomb-like structure of g-C_3N_4 via thermal condensation of urea with the addition of water [187]. An enhanced removal ratio of NO (48%) was reached over the honeycomb structure and remained stable in repeated runs. Interestingly, the formation of toxic intermediate, NO_2 was dramatically inhibited.

In order to improve electronic and photocatalytic properties, Ho et al. investigated on copolymerization induced C-doping for rolling-up the layer structure of g-C_3N_4 [188]. A schematic of the synthesis process and photocatalysis along with supporting TEM images is shown in Fig. 22A. In the tubular configuration, the band gap was narrowed from 2.7 eV (pure g-C_3N_4) to 2.4 eV which extended the absorption of the visible spectrum and enhanced the separation of charges. For the modified g-C_3N_4, a broadened (002) diffraction peak along with a down shift illustrated on the disturbed structure (Fig. 22B). Pertaining to the structural changes, a tuning of the electronic structure was examined with various spectroscopic techniques and theoretical calculations. A high photocatalytic activity compared with the pure structures further confirmed the importance of the modified g-C_3N_4 structure. Cyclic runs for an efficient photocatalytic removal of NOx over the optimized catalyst are shown in Fig. 22C.

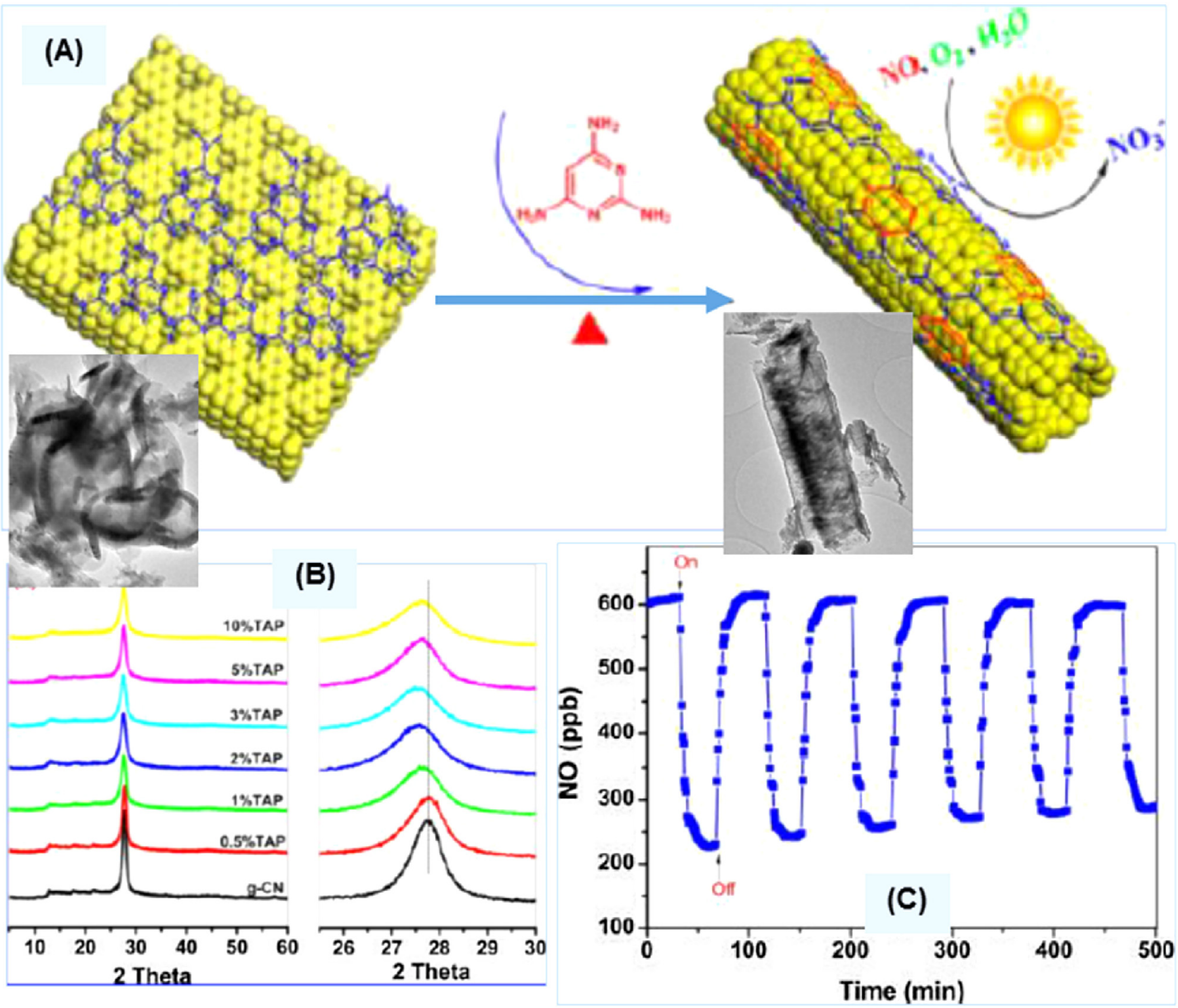

Fig. 22. (A) TEM images and the corresponding schematic representation of rolling-up of the layer structure of g-C_3N_4, (B) Powder XRD patterns for layered g-C_3N_4 after rolled-up structure, and (D) Photocatalytic removal of NO_X.
Reproduced with permission from the Ref. [188]. Copyright (2015) American Chemical Society.

Zhao et al. synthesized carbon self-doped g-C_3N_4 with soft-template of carbon foam which enhanced visible to near-IR absorption [189]. Photocatalytic NO removal ratio over the optimized material reached to 50.1% that was much higher comparing with pure g-C_3N_4 and other similar catalysts. The C-doped nanosheets showed a small decrease in repeated tests. As a further modification of g-C_3N_4, Dong et al. immobilized g-C_3N_4 on structured Al_2O_3 ceramic foam by a novel in-situ thermal approach [190]. The photocatalytic activity improved as the synthesis temperature increased from 450 °C to 600 °C and with the formation of nanoarchitecture. A highly enhanced NO removal ratio of 77.1% was observed over the optimized system. Furthermore, the photocatalyst demonstrated a stable performance in cycling runs.

Next, for enhanced separation of photogenerated charges Dong et al. constructed a metal-free isotype g-C_3N_4/g-C_3N_4 heterojunction from a molecular composite of urea and thiourea precursors [191]. The formation of a heterojunction between two types of nanosheets of g-C_3N_4 was described by TEM observations (Fig. 23A). The average thickness of g-C_3N_4 sheets derived from urea and thiourea was in the range of 20–40 nm (nanosized) and 400–800 nm (bulk structure), respectively. The band edge of the heterojunction was in between the two types of the g-C_3N_4 samples and indicated their electronic coupling. An enhanced quenching of PL intensity as shown in Fig. 23B further supported the formation of heterojunction with a lower rate of recombination. A schematic illustration of enhanced absorption of visible light and efficient separation of photogenerated electron-pairs at the interface is provided in Fig. 23C. Furthermore, electrochemical analyses confirmed the findings from TEM and spectroscopic analyses and indicated good photocatalytic activity of the isotype heterojunction (Fig. 23D). Compared with pure g-C_3N_4 materials obtained from urea (31.7%) and thiourea (27.3%) the isotype heterojunction exhibited an enhanced removal ratio of NO at 47.6%, under visible light irradiation for 30 min.

2.11. Metal ion redox

In contrast to organic pollutants, inorganic metal ions are particularly problematic because they are not biodegradable but can accumulate in tissues and severely endanger the living organisms. Cr^{6+} is a common wastewater pollutant from leather tanning, electroplating, and mining industry. Because of carcinogenicity

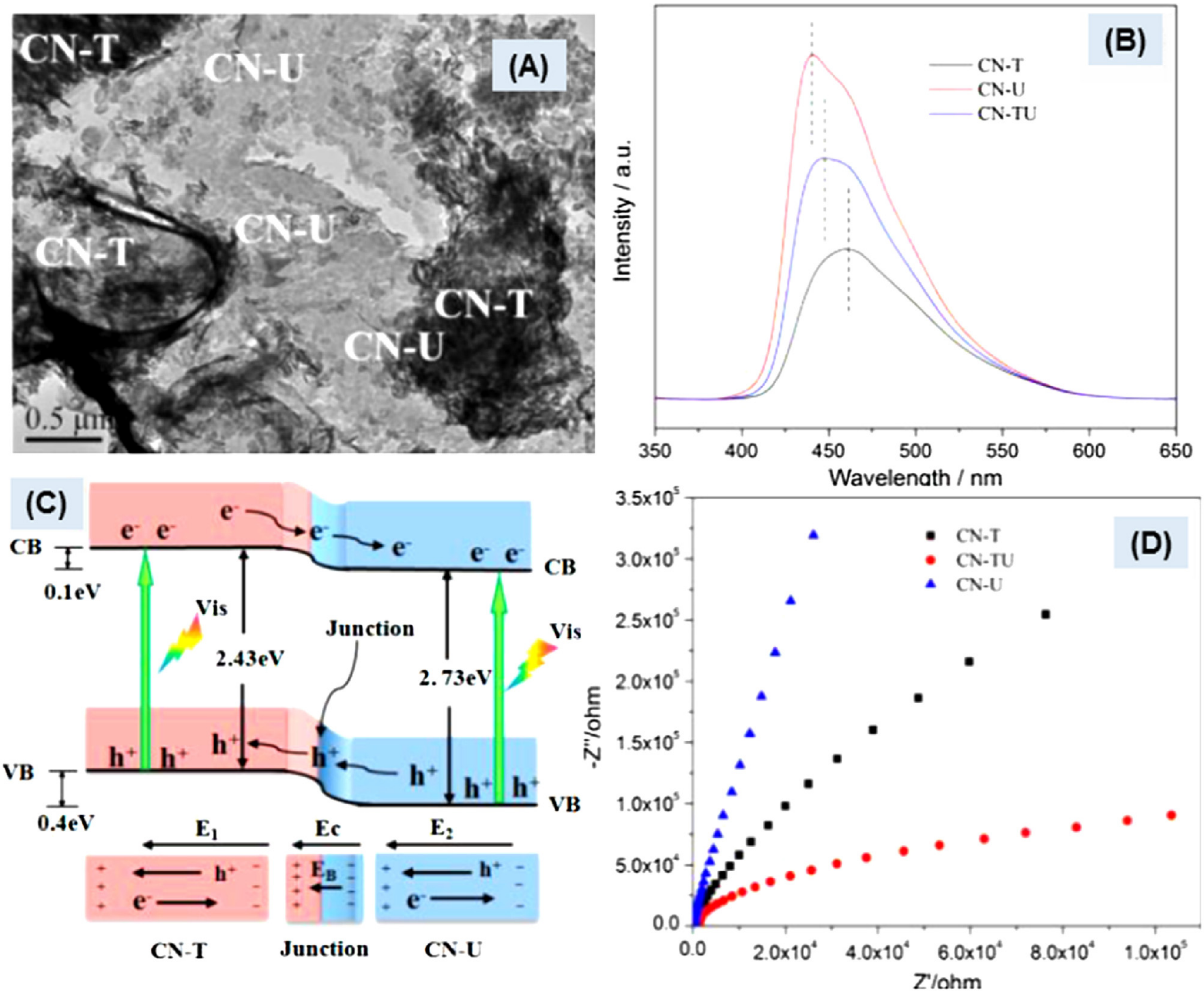

Fig. 23. (A) TEM image of isotype heterojunction of g-C_3N_4, from urea (CN-U) and g-C_3N_4, from thiourea (CN-T), (B) Photoluminescence spectra for pure g-C_3N_4 samples of and their heterojunction, (C) Schematic illustration of separation of photogenerated electron-hole pairs at the heterojunction interface, and (D) Electrochemical impedance spectra of pure g-C_3N_4 samples of and their heterojunction.
Reproduced with permission from the Ref. [191]. Copyright (2015) American Chemical Society.

and mutagenicity related issues, its maximum concentrations in drinking water and discharged industrial wastewaters has been regulated. Reduction of Cr^{6+} to Cr^{3+} is an effect way of controlling its pollution. Uranium is a typical radioactive pollutant from nuclear industry which can cause serious health problems. The predominant oxidation state of uranium species in the ambient environment is the soluble U^{6+} and its reduction to insoluble U^{4+} oxide is an important approach for the elimination of radioactive pollution. Contrary to the desired reduction of Cr^{6+} and U^{6+} species, As^{3+} is highly toxic in its reduced state and oxidation to As^{5+} is helpful in lowering down the toxicity and ultimate removal. So a versatile photocatalyst system is required for controlling the fate of inorganic metal ions, and g-C_3N_4 is a good candidate.

Liu et al. synthesized a composite of g-C_3N_4 with ZnO via a deposition-precipitation followed thermal method [192]. TEM images showed nanoparticle size of the composite (~50 nm) and good contact between organic and inorganic semiconductors to achieve enhanced separation of photogenerated charges. The composite was employed for both photooxidation of RhB and photoreduction of Cr^{6+} under visible light irradiation. The rate constant for photoreduction of Cr^{6+} over the optimized composite (0.0142 min^{-1}) was five times higher compared with pure g-C_3N_4. Photooxidation rate constant for RhB (0.0367 min^{-1}) was more than three times of the pristine g-C_3N_4 and higher comparing with photoreduction process. Sun et al. fabricated visible light active 3D flower-like heterostructure of g-C_3N_4 and SnS_2 nano-flakes via a solvothermal method [193]. Because of high separation of photogenerated charges, the optimized heterojunction showed about 99% photoreduction of toxic Cr^{6+} to Cr^{3+} within 50 min in neutral solution with reaction rate constant of 0.4582 $mol^{-1}\,dm^3\,min^{-1}$. However, the photocatalytic activity slightly decreased in repeated cycles. Uniform size $Zn_{1-X}Cd_XS$ nanoparticles of 15 nm finely distributed on the surface of g-C_3N_4 sheets were prepared via a facile and template free in-situ precipitation method [194]. The nanocomposite was highly efficient for visible light active photooxidation of organic dyes and photoreduction of metal ions. Over the optimized photocatalyst system, quick reduction of about 99% Cr^{6+} to Cr^{3+} was observed in just 25 min of illumination.

Zang et al. hybridize brookite TiO_2 nanoparticles of approximately 40 nm size with g-C_3N_4 sheets via a facile calcination method [195]. The optimized brookite composite showed higher photocatalytic activity comparing with other types of TiO_2, both anatase, and rutile. Visible-light-driven photooxidation of extremely toxic As^{3+} to relatively less toxic As^{5+} reached up to

55% at maximum in 180 min. In addition, comparing with pure materials the optimized composite demonstrated an enhanced photocatalytic degradation of MO. B-doped layered nanosheets of g-C_3N_4 containing nanosize pores were prepared by calcination [196]. The reaction time for the optimized photocatalytic reduction of aqueous UO_2^{2+} decreased from 50 min for g-C_3N_4 to 20 min for the B-doped g-C_3N_4. The rate constant for the optimized sample was 0.13 min^{-1} which was 2.54 times higher than pure g-C_3N_4 and slightly decreased in recycling tests.

These studies summarized in this review demonstrate on the use of g-C_3N_4 based nanomaterials for photocatalytic applications. Especially, this database on noble-metal-free photocatalyst systems for all the various applications will be a useful guideline for sustainable developments.

3. Conclusions and future perspectives

In all the various photoactive applications, noble-metal-free nanoscale photocatalyst systems based on g-C_3N_4 demonstrated favorable results for its versatile applications. Especially, the good achievements in H_2 evolution reaction surpassing that of with the Pt co-catalyst are highly promising towards a sustainable production of green and renewable energy. Pertaining to the high stability of g-C_3N_4 and its nanocomposites under different conditions, it has gained attention for a number of organic synthesis reactions. Reduction of CO_2 is also successfully explored on some nanoscale combinations of g-C_3N_4. Some developments are also made towards the photocatalytic fixation of N_2. Photodegradation of various organic pollutants without H_2O_2 is successfully achieved on g-C_3N_4 based nanomaterials. Photocatalytic removal of NO_X has also shown a potential application of this polymeric semiconductor. Although interesting photocatalytic results are achieved on the noble-metal-free nanoscale materials but still there are many areas needing attention for further improvements. Indeed, a facile synthesis of materials is important but we should not overlook a better design of the nanoscale materials towards an enhanced photocatalytic performance. Innovative methods and computational help are required towards the fabrication of site-selective loading of nanoparticles for an enhanced efficient performance. In addition, greener synthesis strategies should be sought after for a sustainable synthesis of the photoactive nanomaterials. Furthermore, development of materials with magnetic properties for an easy separation are highly desired. For a true evaluation of the noble-metal-free systems, it requires making a fair comparison with the optimized loaded noble metal based reference photocatalyst. For most of the g-C_3N_4 hybrid systems with sulfur based materials, further modifications are required to overcome the long induction period in H_2 evolution reaction. Furthermore, the stability of metal sulfide hybrids remains an outstanding issue. Detailed characterizations of the spent catalysts, especially with TEM is needful to observe the evolution of the active site and their stability during photocatalytic testing. And last but not least, any secondary hazards from the nanoscale materials need a serious consideration before moving forward to their large-scale applications.

Acknowledgements

The authors wish to thank the Natural Sciences and Engineering Research Council of Canada for the financial support to conduct this research work.

References

[1] A. Thomas, A. Fischer, F. Goettmann, M. Antonietti, J.-O. Müller, R. Schlögl, J.M. Carlsson, Graphitic carbon nitride materials: variation of structure and morphology and their use as metal-free catalysts, J. Mater. Chem. 18 (2008) 4893–4908, http://dx.doi.org/10.1039/B800274F.

[2] W.-J. Ong, L.-L. Tan, Y.H. Ng, S.-T. Yong, S.-P. Chai, Graphitic carbon nitride (g-C3N4)-based photocatalysts for artificial photosynthesis and environmental remediation: are we a step closer to achieving sustainability? Chem. Rev. (2016), http://dx.doi.org/10.1021/acs.chemrev.6b00075.

[3] A. Fujishima, K. Honda, Electrochemical photolysis of water at a semiconductor electrode, Nature 238 (1972) 37–38, http://dx.doi.org/10.1038/238037a0.

[4] X. Wang, K. Maeda, A. Thomas, K. Takanabe, G. Xin, J.M. Carlsson, K. Domen, M. Antonietti, A metal-free polymeric photocatalyst for hydrogen production from water under visible light, Nat. Mater. 8 (2009) 76–80, http://dx.doi.org/10.1038/nmat2317.

[5] X. Wang, K. Maeda, X. Chen, K. Takanabe, K. Domen, Y. Hou, X. Fu, M. Antonietti, Polymer semiconductors for artificial photosynthesis: hydrogen evolution by mesoporous graphitic carbon nitride with visible light, J. Am. Chem. Soc. 131 (2009) 1680–1681, http://dx.doi.org/10.1021/ja809307s.

[6] X. Wang, S. Blechert, M. Antonietti, Polymeric graphitic carbon nitride for heterogeneous photocatalysis, ACS Catal. 2 (2012) 1596–1606, http://dx.doi.org/10.1021/cs300240x.

[7] S. Cao, J. Yu, g-C3N4-based photocatalysts for hydrogen generation, J. Phys. Chem. Lett. 5 (2014) 2101–2107, http://dx.doi.org/10.1021/jz500546b.

[8] G. Dong, Y. Zhang, Q. Pan, J. Qiu, A fantastic graphitic carbon nitride (g-C3N4) material: electronic structure, photocatalytic and photoelectronic properties, J. Photochem. Photobiol. C Photochem. Rev. 20 (2014) 33–50, http://dx.doi.org/10.1016/j.jphotochemrev.2014.04.002.

[9] X. Dong, F. Cheng, Recent development in exfoliated two-dimensional g-C3N4 nanosheets for photocatalytic applications, J. Mater. Chem. A 3 (2015) 23642–23652, http://dx.doi.org/10.1039/C5TA07374J.

[10] Y. Zheng, L. Lin, B. Wang, X. Wang, Graphitic carbon nitride polymers toward sustainable photoredox catalysis, Angew. Chem. Int. Ed. 54 (2015) 12868–12884, http://dx.doi.org/10.1002/anie.201501788.

[11] S. Yin, J. Han, T. Zhou, R. Xu, Recent progress in g-C3N4 based low cost photocatalytic system: activity enhancement and emerging applications, Catal. Sci. Technol. 5 (2015) 5048–5061, http://dx.doi.org/10.1039/C5CY00938C.

[12] Z. Zhao, Y. Sun, F. Dong, Graphitic carbon nitride based nanocomposites: a review, Nanoscale 7 (2014) 15–37, http://dx.doi.org/10.1039/C4NR03008G.

[13] S. Cao, J. Low, J. Yu, M. Jaroniec, Polymeric photocatalysts based on graphitic carbon nitride, Adv. Mater. 27 (2015) 2150–2176, http://dx.doi.org/10.1002/adma.201500033.

[14] S. Ye, R. Wang, M.-Z. Wu, Y.-P. Yuan, A review on g-C3N4 for photocatalytic water splitting and CO2 reduction, Appl. Surf. Sci. 358 (Part A) (2015) 15–27, http://dx.doi.org/10.1016/j.apsusc.2015.08.173.

[15] G. Mamba, A.K. Mishra, Graphitic carbon nitride (g-C3N4) nanocomposites: a new and exciting generation of visible light driven photocatalysts for environmental pollution remediation, Appl. Catal. B Environ. 198 (2016) 347–377, http://dx.doi.org/10.1016/j.apcatb.2016.05.052.

[16] K. Nakata, A. Fujishima, TiO2 photocatalysis: design and applications, J. Photochem. Photobiol. C Photochem. Rev. 13 (2012) 169–189, http://dx.doi.org/10.1016/j.jphotochemrev.2012.06.001.

[17] X. Wang, X. Chen, A. Thomas, X. Fu, M. Antonietti, Metal-containing carbon nitride compounds: a new functional organic–metal hybrid material, Adv. Mater. 21 (2009) 1609–1612, http://dx.doi.org/10.1002/adma.200802627.

[18] X. Chen, J. Zhang, X. Fu, M. Antonietti, X. Wang, Fe-g-C3N4-catalyzed oxidation of benzene to phenol using hydrogen peroxide and visible light, J. Am. Chem. Soc. 131 (2009) 11658–11659, http://dx.doi.org/10.1021/ja903923s.

[19] J. Zhang, X. Chen, K. Takanabe, K. Maeda, K. Domen, J.D. Epping, X. Fu, M. Antonietti, X. Wang, Synthesis of a carbon nitride structure for visible-light catalysis by copolymerization, Angew. Chem. Int. Ed. 49 (2010) 441–444, http://dx.doi.org/10.1002/anie.200903886.

[20] J. Zhang, M. Zhang, R.-Q. Sun, X. Wang, A facile band alignment of polymeric carbon nitride semiconductors to construct isotype heterojunctions, Angew. Chem. Int. Ed. 51 (2012) 10145–10149, http://dx.doi.org/10.1002/anie.201205333.

[21] K. Takanabe, K. Kamata, X. Wang, M. Antonietti, J. Kubota, K. Domen, Photocatalytic hydrogen evolution on dye-sensitized mesoporous carbon nitride photocatalyst with magnesium phthalocyanine, Phys. Chem. Chem. Phys. 12 (2010) 13020–13025, http://dx.doi.org/10.1039/C0CP00611D.

[22] J. Zhang, M. Zhang, C. Yang, X. Wang, Nanospherical carbon nitride frameworks with sharp edges accelerating charge collection and separation at a soft photocatalytic interface, Adv. Mater. 26 (2014) 4121–4126, http://dx.doi.org/10.1002/adma.201400573.

[23] J. Sun, J. Zhang, M. Zhang, M. Antonietti, X. Fu, X. Wang, Bioinspired hollow semiconductor nanospheres as photosynthetic nanoparticles, Nat. Commun. 3 (2012) 1139, http://dx.doi.org/10.1038/ncomms2152.

[24] J. Zhang, F. Guo, X. Wang, An optimized and general synthetic strategy for fabrication of polymeric carbon nitride nanoarchitectures, Adv. Funct. Mater. 23 (2013) 3008–3014, http://dx.doi.org/10.1002/adfm.201203287.

[25] Z. Lin, X. Wang, Nanostructure engineering and doping of conjugated carbon nitride semiconductors for hydrogen photosynthesis, Angew. Chem. Int. Ed. 52 (2013) 1735–1738, http://dx.doi.org/10.1002/anie.201209017.

[26] M. Zhang, X. Wang, Two dimensional conjugated polymers with enhanced optical absorption and charge separation for photocatalytic hydrogen

evolution, Energy Environ. Sci. 7 (2014) 1902–1906, http://dx.doi.org/10.1039/C3EE44189J.
[27] G. Zhang, G. Li, X. Wang, Surface modification of carbon nitride polymers by core–shell nickel/nickel oxide cocatalysts for hydrogen evolution photocatalysis, ChemCatChem 7 (2015) 2864–2870, http://dx.doi.org/10.1002/cctc.201500069.
[28] D. Zheng, G. Zhang, Y. Hou, X. Wang, Layering MoS2 on soft hollow g-C3N4 nanostructures for photocatalytic hydrogen evolution, Appl. Catal. Gen. 521 (2016) 2–8, http://dx.doi.org/10.1016/j.apcata.2015.10.037.
[29] G. Zhang, S. Zang, X. Wang, Layered Co(OH)2 deposited polymeric carbon nitrides for photocatalytic water oxidation, ACS Catal. 5 (2015) 941–947, http://dx.doi.org/10.1021/cs502002u.
[30] G. Zhang, S. Zang, L. Lin, Z.-A. Lan, G. Li, X. Wang, Ultrafine cobalt catalysts on covalent carbon nitride frameworks for oxygenic photosynthesis, ACS Appl. Mater. Interfaces 8 (2016) 2287–2296, http://dx.doi.org/10.1021/acsami.5b11167.
[31] J. Qin, S. Wang, H. Ren, Y. Hou, X. Wang, Photocatalytic reduction of CO2 by graphitic carbon nitride polymers derived from urea and barbituric acid, Appl. Catal. B Environ. 179 (2015) 1–8, http://dx.doi.org/10.1016/j.apcatb.2015.05.005.
[32] S. Nayak, L. Mohapatra, K. Parida, Visible light-driven novel g-C3N4/NiFe-LDH composite photocatalyst with enhanced photocatalytic activity towards water oxidation and reduction reaction, J. Mater. Chem. A 3 (2015) 18622–18635, http://dx.doi.org/10.1039/C5TA05002B.
[33] J. Liu, Y. Liu, N. Liu, Y. Han, X. Zhang, H. Huang, Y. Lifshitz, S.-T. Lee, J. Zhong, Z. Kang, Metal-free efficient photocatalyst for stable visible water splitting via a two-electron pathway, Science 347 (2015) 970–974, http://dx.doi.org/10.1126/science.aaa3145.
[34] Y. Cui, Z. Ding, X. Fu, X. Wang, Construction of conjugated carbon nitride nanoarchitectures in solution at low temperatures for photoredox catalysis, Angew. Chem. Int. Ed. 51 (2012) 11814–11818, http://dx.doi.org/10.1002/anie.201206534.
[35] A. Suryawanshi, P. Dhanasekaran, D. Mhamane, S. Kelkar, S. Patil, N. Gupta, S. Ogale, Doubling of photocatalytic H2 evolution from g-C3N4 via its nanocomposite formation with multiwall carbon nanotubes: electronic and morphological effects, Int. J. Hydrogen Energy. 37 (2012) 9584–9589, http://dx.doi.org/10.1016/j.ijhydene.2012.03.123.
[36] F. He, G. Chen, Y. Zhou, Y. Yu, L. Li, S. Hao, B. Liu, ZIF-8 derived carbon (C-ZIF) as a bifunctional electron acceptor and HER cocatalyst for g-C3N4: construction of a metal-free, all carbon-based photocatalytic system for efficient hydrogen evolution, J. Mater. Chem. A. 4 (2016) 3822–3827, http://dx.doi.org/10.1039/C6TA00497K.
[37] S. Fang, Y. Xia, K. Lv, Q. Li, J. Sun, M. Li, Effect of carbon-dots modification on the structure and photocatalytic activity of g-C3N4, Appl. Catal. B Environ. 185 (2016) 225–232, http://dx.doi.org/10.1016/j.apcatb.2015.12.025.
[38] Y. Ma, E. Liu, X. Hu, C. Tang, J. Wan, J. Li, J. Fan, A simple process to prepare few-layer g-C3N4 nanosheets with enhanced photocatalytic activities, Appl. Surf. Sci. 358 (Part A) (2015) 246–251, http://dx.doi.org/10.1016/j.apsusc.2015.08.174.
[39] Q. Liang, Z. Li, Z.-H. Huang, F. Kang, Q.-H. Yang, Holey graphitic carbon nitride nanosheets with carbon vacancies for highly improved photocatalytic hydrogen production, Adv. Funct. Mater. 25 (2015) 6885–6892, http://dx.doi.org/10.1002/adfm.201503221.
[40] X. Xia, N. Deng, G. Cui, J. Xie, X. Shi, Y. Zhao, Q. Wang, W. Wang, B. Tang, NIR light induced H2 evolution by a metal-free photocatalyst, Chem. Commun. 51 (2015) 10899–10902, http://dx.doi.org/10.1039/C5CC02589C.
[41] Y. Hou, A.B. Laursen, J. Zhang, G. Zhang, Y. Zhu, X. Wang, S. Dahl, I. Chorkendorff, Layered nanojunctions for hydrogen-evolution catalysis, Angew. Chem. Int. Ed. 52 (2013) 3621–3625, http://dx.doi.org/10.1002/anie.201210294.
[42] J. Yu, S. Wang, B. Cheng, Z. Lin, F. Huang, Noble metal-free Ni(OH)2–g-C3N4 composite photocatalyst with enhanced visible-light photocatalytic H2-production activity, Catal. Sci. Technol. 3 (2013) 1782–1789, http://dx.doi.org/10.1039/C3CY20878H.
[43] L. Bi, D. Xu, L. Zhang, Y. Lin, D. Wang, T. Xie, Metal Ni-loaded g-C3N4 for enhanced photocatalytic H2 evolution activity: the change in surface band bending, Phys. Chem. Chem. Phys. 17 (2015) 29899–29905, http://dx.doi.org/10.1039/C5CP05158D.
[44] L. Kong, Y. Dong, P. Jiang, G. Wang, H. Zhang, N. Zhao, Light-assisted rapid preparation of a Ni/g-C3N4 magnetic composite for robust photocatalytic H2 evolution from water, J. Mater. Chem. A. 4 (2016) 9998–10007, http://dx.doi.org/10.1039/C6TA03178A.
[45] M.S. Akple, J. Low, S. Wageh, A.A. Al-Ghamdi, J. Yu, J. Zhang, Enhanced visible light photocatalytic H2-production of g-C3N4/WS2 composite heterostructures, Appl. Surf. Sci. 358 (Part A) (2015) 196–203, http://dx.doi.org/10.1016/j.apsusc.2015.08.250.
[46] W. Chen, T.-Y. Liu, T. Huang, X.-H. Liu, G.-R. Duan, X.-J. Yang, S.-M. Chen, A novel yet simple strategy to fabricate visible light responsive C,N-TiO2/g-C3N4 heterostructures with significantly enhanced photocatalytic hydrogen generation, RSC Adv. 5 (2015) 101214–101220, http://dx.doi.org/10.1039/C5RA18302B.
[47] H. Liu, Z. Jin, Z. Xu, Hybridization of Cd0.2Zn0.8S with g-C3N4 nanosheets: a visible-light-driven photocatalyst for H2 evolution from water and degradation of organic pollutants, Dalton Trans. 44 (2015) 14368–14375, http://dx.doi.org/10.1039/C5DT01364J.
[48] S.-S. Yi, J.-M. Yan, B.-R. Wulan, S.-J. Li, K.-H. Liu, Q. Jiang, Noble-metal-free cobalt phosphide modified carbon nitride: an efficient photocatalyst for hydrogen generation, Appl. Catal. B Environ. 200 (2017) 477–483, http://dx.doi.org/10.1016/j.apcatb.2016.07.046.
[49] D.H. Wang, J.N. Pan, H.H. Li, J.J. Liu, Y.B. Wang, L.T. Kang, J.N. Yao, A pure organic heterostructure of μ-oxo dimeric iron(III) porphyrin and graphitic-C3N4 for solar H2 roduction from water, J. Mater. Chem. A 4 (2015) 290–296, http://dx.doi.org/10.1039/C5TA07278F.
[50] S.-W. Cao, Y.-P. Yuan, J. Barber, S.C.J. Loo, C. Xue, Noble-metal-free g-C3N4/Ni(dmgH)2 composite for efficient photocatalytic hydrogen evolution under visible light irradiation, Appl. Surf. Sci. 319 (2014) 344–349, http://dx.doi.org/10.1016/j.apsusc.2014.04.094.
[51] S.-W. Cao, X.-F. Liu, Y.-P. Yuan, Z.-Y. Zhang, J. Fang, S.C.J. Loo, J. Barber, T.C. Sum, C. Xue, Artificial photosynthetic hydrogen evolution over g-C3N4 nanosheets coupled with cobaloxime, Phys. Chem. Chem. Phys. 15 (2013) 18363–18366, http://dx.doi.org/10.1039/C3CP53350F.
[52] J. Hong, Y. Wang, Y. Wang, W. Zhang, R. Xu, Noble-metal-free NiS/C3N4 for efficient photocatalytic hydrogen evolution from water, ChemSusChem 6 (2013), http://dx.doi.org/10.1002/cssc.201301147, 2200–2200.
[53] Y. Lu, D. Chu, M. Zhu, Y. Du, P. Yang, Exfoliated carbon nitride nanosheets decorated with NiS as an efficient noble-metal-free visible-light-driven photocatalyst for hydrogen evolution, Phys. Chem. Chem. Phys. 17 (2015) 17355–17361, http://dx.doi.org/10.1039/C5CP01657F.
[54] F. Raziq, Y. Qu, X. Zhang, M. Humayun, J. Wu, A. Zada, H. Yu, X. Sun, L. Jing, Enhanced cocatalyst-Free visible-light activities for photocatalytic fuel production of g-C3N4 by trapping holes and transferring electrons, J. Phys. Chem. C 120 (2016) 98–107, http://dx.doi.org/10.1021/acs.jpcc.5b10313.
[55] X. Wang, J. Chen, X. Guan, L. Guo, Enhanced efficiency and stability for visible light driven water splitting hydrogen production over Cd0.5Zn0.5S/g-C3N4 composite photocatalyst, Int. J. Hydrogen Energy 40 (2015) 7546–7552, http://dx.doi.org/10.1016/j.ijhydene.2014.11.055.
[56] H. Liu, Z. Xu, Z. Zhang, D. Ao, Novel visible-light driven Mn0.8Cd0.2S/g-C3N4 composites: Preparation and efficient photocatalytic hydrogen production from water without noble metals, Appl. Catal. Gen. (n.d.). http://dx.doi.org/10.1016/j.apcata.2015.08.026.
[57] H. Liu, Z. Xu, Z. Zhang, D. Ao, Highly efficient photocatalytic H2 evolution from water over CdLa2S4/mesoporous g-C3N4 hybrids under visible light irradiation, Appl. Catal. B Environ. 192 (2016) 234–241, http://dx.doi.org/10.1016/j.apcatb.2016.03.074.
[58] H. Liu, Z. Jin, Z. Xu, Z. Zhang, D. Ao, Fabrication of ZnIn2S4–g-C3N4 sheet-on-sheet nanocomposites for efficient visible-light photocatalytic H2-evolution and degradation of organic pollutants, RSC Adv. 5 (2015) 97951–97961, http://dx.doi.org/10.1039/C5RA17028A.
[59] Z. Zhang, K. Liu, Z. Feng, Y. Bao, B. Dong, Hierarchical sheet-on-sheet ZnIn2S4/g-C3N4 heterostructure with highly efficient photocatalytic H2 production based on photoinduced interfacial charge transfer, Sci. Rep. 6 (2016) 19221, http://dx.doi.org/10.1038/srep19221.
[60] P. Suyana, K.R. Sneha, B.N. Nair, V. Karunakaran, A.P. Mohamed, K.G.K. Warrier, U.S. Hareesh, A facile one pot synthetic approach for C3N4–ZnS composite interfaces as heterojunctions for sunlight-induced multifunctional photocatalytic applications, RSC Adv. 6 (2016) 17800–17809, http://dx.doi.org/10.1039/C5RA27427C.
[61] Y. Zhong, J. Yuan, J. Wen, X. Li, Y. Xu, W. Liu, S. Zhang, Y. Fang, Earth-abundant NiS co-catalyst modified metal-free mpg-C3N4/CNT nanocomposites for highly efficient visible-light photocatalytic H2 evolution, Dalton Trans. 44 (2015) 18260–18269, http://dx.doi.org/10.1039/C5DT02693H.
[62] J. Yuan, J. Wen, Y. Zhong, X. Li, Y. Fang, S. Zhang, W. Liu, Enhanced photocatalytic H2 evolution over noble-metal-free NiS cocatalyst modified CdS nanorods/g-C3N4 heterojunctions, J. Mater. Chem. A 3 (2015) 18244–18255, http://dx.doi.org/10.1039/C5TA04573H.
[63] J. Wen, X. Li, H. Li, S. Ma, K. He, Y. Xu, Y. Fang, W. Liu, Q. Gao, Enhanced visible-light H2 evolution of g-C3N4 photocatalysts via the synergetic effect of amorphous NiS and cheap metal-free carbon black nanoparticles as co-catalysts, Appl. Surf. Sci. 358 (Part A) (2015) 204–212, http://dx.doi.org/10.1016/j.apsusc.2015.08.244.
[64] G. Bi, J. Wen, X. Li, W. Liu, J. Xie, Y. Fang, W. Zhang, Efficient visible-light photocatalytic H2 evolution over metal-free g-C3N4 co-modified with robust acetylene black and Ni(OH)2 as dual co-catalysts, RSC Adv. 6 (2016) 31497–31506, http://dx.doi.org/10.1039/C6RA03118H.
[65] K. Mori, T. Itoh, H. Kakudo, T. Iwamoto, Y. Masui, M. Onaka, H. Yamashita, Nickel-supported carbon nitride photocatalyst combined with organic dye for visible-light-driven hydrogen evolution from water, Phys. Chem. Chem. Phys. 17 (2015) 24086–24091, http://dx.doi.org/10.1039/C5CP04493F.
[66] S. Pany, K.M. Parida, A facile in situ approach to fabricate N,S-TiO2/g-C3N4 nanocomposite with excellent activity for visible light induced water splitting for hydrogen evolution, Phys. Chem. Chem. Phys. 17 (2015) 8070–8077, http://dx.doi.org/10.1039/C4CP05582A.
[67] J. Wang, J. Huang, H. Xie, A. Qu, Synthesis of g-C3N4/TiO2 with enhanced photocatalytic activity for H2 evolution by a simple method, Int. J. Hydrogen Energy 39 (2014) 6354–6363, http://dx.doi.org/10.1016/j.ijhydene.2014.02.020.
[68] Z. Jiang, D. Jiang, Z. Yan, D. Liu, K. Qian, J. Xie, A new visible light active multifunctional ternary composite based on TiO2-In2O3 nanocrystals heterojunction decorated porous graphitic carbon nitride for photocatalytic

treatment of hazardous pollutant and H2 evolution, Appl. Catal. B Environ. 170–171 (2015) 195–205, http://dx.doi.org/10.1016/j.apcatb.2015.01.041.
[69] Z. Li, Y. Wu, G. Lu, Highly efficient hydrogen evolution over Co(OH)2 nanoparticles modified g-C3N4 co-sensitized by Eosin Y and Rose Bengal under Visible Light Irradiation, Appl. Catal. B Environ. 188 (2016) 56–64, http://dx.doi.org/10.1016/j.apcatb.2016.01.057.
[70] X. Hao, Z. Jin, S. Min, G. Lu, Modulating photogenerated electron transfer with selectively exposed Co–Mo facets on a novel amorphous g-C3N4/CoxMo1-xS2 photocatalyst, RSC Adv. 6 (2016) 23709–23717, http://dx.doi.org/10.1039/C5RA22102A.
[71] F. Shi, L. Chen, M. Chen, D. Jiang, A g-C3N4/nanocarbon/ZnIn2S4 nanocomposite: an artificial Z-scheme visible-light photocatalytic system using nanocarbon as the electron mediator, Chem. Commun. 51 (2015) 17144–17147, http://dx.doi.org/10.1039/C5CC05323D.
[72] M. Li, L. Zhang, X. Fan, M. Wu, Y. Du, M. Wang, Q. Kong, L. Zhang, J. Shi, Dual synergetic effects in MoS2/pyridine-modified g-C3N4 composite for highly active and stable photocatalytic hydrogen evolution under visible light, Appl. Catal. B Environ. 190 (2016) 36–43, http://dx.doi.org/10.1016/j.apcatb.2016.02.060.
[73] F. Cheng, H. Yin, Q. Xiang, Low-temperature solid-state preparation of ternary CdS/g-C3N4/CuS nanocomposites for enhanced visible-light photocatalytic H2-production activity, Appl. Surf. Sci. (n.d.) http://dx.doi.org/10.1016/j.apsusc.2016.06.169.
[74] P. Zhang, T. Wang, H. Zeng, Design of Cu-Cu2O/g-C3N4 nanocomponent photocatalysts for hydrogen evolution under visible light irradiation using water-soluble Erythrosin B dye sensitization, Appl. Surf. Sci. (n.d.) http://dx.doi.org/10.1016/j.apsusc.2016.05.162.
[75] H. Hou, F. Gao, L. Wang, M. Shang, Z. Yang, J. Zheng, W. Yang, Superior thoroughly mesoporous ternary hybrid photocatalysts of TiO2/WO3/g-C3N4 nanofibers for visible-light-driven hydrogen evolution, J. Mater. Chem. A 4 (2016) 6276–6281, http://dx.doi.org/10.1039/C6TA02307J.
[76] K.N. Ferreira, T.M. Iverson, K. Maghlaoui, J. Barber, S. Iwata, Architecture of the photosynthetic oxygen-evolving center, Science 303 (2004) 1831–1838, http://dx.doi.org/10.1126/science.1093087.
[77] J.F. Hull, D. Balcells, J.D. Blakemore, C.D. Incarvito, O. Eisenstein, G.W. Brudvig, R.H. Crabtree, Highly active and robust Cp* iridium complexes for catalytic water oxidation, J. Am. Chem. Soc. 131 (2009) 8730–8731, http://dx.doi.org/10.1021/ja901270f.
[78] L. Duan, F. Bozoglian, S. Mandal, B. Stewart, T. Privalov, A. Llobet, L. Sun, A molecular ruthenium catalyst with water-oxidation activity comparable to that of photosystem II, Nat. Chem. 4 (2012) 418–423, http://dx.doi.org/10.1038/nchem.1301.
[79] J. Zhang, J. Sun, K. Maeda, K. Domen, P. Liu, M. Antonietti, X. Fu, X. Wang, Sulfur-mediated synthesis of carbon nitride: band-gap engineering and improved functions for photocatalysis, Energy Environ. Sci. 4 (2011) 675–678, http://dx.doi.org/10.1039/C0EE00418A.
[80] J. Zhang, M. Grzelczak, Y. Hou, K. Maeda, K. Domen, X. Fu, M. Antonietti, X. Wang, Photocatalytic oxidation of water by polymeric carbon nitride nanohybrids made of sustainable elements, Chem. Sci. 3 (2012) 443–446, http://dx.doi.org/10.1039/C1SC00644D.
[81] S. Chu, Y. Wang, Y. Guo, J. Feng, C. Wang, W. Luo, X. Fan, Z. Zou, Band structure engineering of carbon nitride: in search of a polymer photocatalyst with high photooxidation property, ACS Catal. 3 (2013) 912–919, http://dx.doi.org/10.1021/cs4000624.
[82] Y. Kofuji, Y. Isobe, Y. Shiraishi, H. Sakamoto, S. Tanaka, S. Ichikawa, T. Hirai, Carbon nitride–aromatic diimide–graphene nanohybrids: metal-free photocatalysts for solar-to-hydrogen peroxide energy conversion with 0.2% efficiency, J. Am. Chem. Soc. 138 (2016) 10019–10025, http://dx.doi.org/10.1021/jacs.6b05806.
[83] Y. Li, S. Ouyang, H. Xu, X. Wang, Y. Bi, Y. Zhang, J. Ye, Constructing solid–gas-interfacial fenton reaction over Alkalinized-C3N4 photocatalyst to achieve apparent quantum yield of 49% at 420 nm, J. Am. Chem. Soc. 138 (2016) 13289–13297, http://dx.doi.org/10.1021/jacs.6b07272.
[84] M. Halmann, Photoelectrochemical reduction of aqueous carbon dioxide on p-type gallium phosphide in liquid junction solar cells, Nature 275 (1978) 115, http://dx.doi.org/10.1038/275115a0.
[85] T. Inoue, A. Fujishima, S. Konishi, K. Honda, Photoelectrocatalytic reduction of carbon dioxide in aqueous suspensions of semiconductor powders, Nature 277 (1979) 637–638, http://dx.doi.org/10.1038/277637a0.
[86] J. Mao, T. Peng, X. Zhang, K. Li, L. Ye, L. Zan, Effect of graphitic carbon nitride microstructures on the activity and selectivity of photocatalytic CO2 reduction under visible light, Catal. Sci. Technol. 3 (2013) 1253–1260, http://dx.doi.org/10.1039/C3CY20822B.
[87] P. Niu, Y. Yang, J.C. Yu, G. Liu, H.-M. Cheng, Switching the selectivity of the photoreduction reaction of carbon dioxide by controlling the band structure of a g-C3N4 photocatalyst, Chem. Commun. 50 (2014) 10837–10840, http://dx.doi.org/10.1039/C4CC03060E.
[88] W.-J. Ong, L.-L. Tan, S.-P. Chai, S.-T. Yong, A.R. Mohamed, Surface charge modification via protonation of graphitic carbon nitride (g-C3N4) for electrostatic self-assembly construction of 2D/2D reduced graphene oxide (rGO)/g-C3N4 nanostructures toward enhanced photocatalytic reduction of carbon dioxide to methane, Nano Energy 13 (2015) 757–770, http://dx.doi.org/10.1016/j.nanoen.2015.03.014.
[89] J.-C. Wang, H.-C. Yao, Z.-Y. Fan, L. Zhang, J.-S. Wang, S.-Q. Zang, Z.-J. Li, Indirect Z-scheme BiOI/g-C3N4 photocatalysts with enhanced photoreduction CO2 activity under visible light irradiation, ACS Appl. Mater. Interfaces 8 (2016) 3765–3775, http://dx.doi.org/10.1021/acsami.5b09901.
[90] L. Shi, T. Wang, H. Zhang, K. Chang, J. Ye, Electrostatic self-assembly of nanosized carbon nitride nanosheet onto a zirconium metal–organic framework for enhanced photocatalytic CO2 reduction, Adv. Funct. Mater. 25 (2015) 5360–5367, http://dx.doi.org/10.1002/adfm.201502253.
[91] S. Zhou, Y. Liu, J. Li, Y. Wang, G. Jiang, Z. Zhao, D. Wang, A. Duan, J. Liu, Y. Wei, Facile in situ synthesis of graphitic carbon nitride (g-C3N4)-N-TiO2 heterojunction as an efficient photocatalyst for the selective photoreduction of CO2 to CO, Appl. Catal. B Environ. 158–159 (2014) 20–29, http://dx.doi.org/10.1016/j.apcatb.2014.03.037.
[92] Y. He, Y. Wang, L. Zhang, B. Teng, M. Fan, High-efficiency conversion of CO2 to fuel over ZnO/g-C3N4 photocatalyst, Appl. Catal. B Environ. 168–169 (2015) 1–8, http://dx.doi.org/10.1016/j.apcatb.2014.12.017.
[93] Y. He, L. Zhang, M. Fan, X. Wang, M.L. Walbridge, Q. Nong, Y. Wu, L. Zhao, Z-scheme SnO2-x/g-C3N4 composite as an efficient photocatalyst for dye degradation and photocatalytic CO2 reduction, Sol. Energy Mater. Sol. Cells 137 (2015) 175–184, http://dx.doi.org/10.1016/j.solmat.2015.01.037.
[94] G.N. Schrauzer, T.D. Guth, Photocatalytic reactions. 1. Photolysis of water and photoreduction of nitrogen on titanium dioxide, J. Am. Chem. Soc. 99 (1977) 7189–7193, http://dx.doi.org/10.1021/ja00464a015.
[95] S. Hu, W. Zhang, J. Bai, G. Lu, L. Zhang, G. Wu, Construction of a 2D/2D g-C3N4/rGO hybrid heterojunction catalyst with outstanding charge separation ability and nitrogen photofixation performance via a surface protonation process, RSC Adv. 6 (2016) 25695–25702, http://dx.doi.org/10.1039/C5RA28123G.
[96] S. Hu, Y. Li, F. Li, Z. Fan, H. Ma, W. Li, X. Kang, Construction of g-C3N4/Zn0.11Sn0.12Cd0.88S1.12 hybrid heterojunction catalyst with outstanding nitrogen photofixation performance induced by sulfur vacancies, ACS Sustain. Chem. Eng. 4 (2016) 2269–2278, http://dx.doi.org/10.1021/acssuschemeng.5b01742.
[97] Q. Zhang, S. Hu, Z. Fan, D. Liu, Y. Zhao, H. Ma, F. Li, Preparation of g-C3N4/ZnMoCdS hybrid heterojunction catalyst with outstanding nitrogen photofixation performance under visible light via hydrothermal post-treatment, Dalton Trans. 45 (2016) 3497–3505, http://dx.doi.org/10.1039/C5DT04901F.
[98] F. Su, S.C. Mathew, G. Lipner, X. Fu, M. Antonietti, S. Blechert, X. Wang, mpg-C3N4-catalyzed selective oxidation of alcohols using O2 and visible light, J. Am. Chem. Soc. 132 (2010) 16299–16301, http://dx.doi.org/10.1021/ja102866p.
[99] F. Su, S.C. Mathew, L. Möhlmann, M. Antonietti, X. Wang, S. Blechert, Aerobic oxidative coupling of amines by carbon nitride photocatalysis with visible light, Angew. Chem. Int. Ed. 50 (2011) 657–660, http://dx.doi.org/10.1002/anie.201004365.
[100] Y. Chen, J. Zhang, M. Zhang, X. Wang, Molecular and textural engineering of conjugated carbon nitride catalysts for selective oxidation of alcohols with visible light, Chem. Sci. 4 (2013) 3244–3248, http://dx.doi.org/10.1039/C3SC51203G.
[101] Y. Wang, X. Wang, M. Antonietti, Polymeric graphitic carbon nitride as a heterogeneous organocatalyst: from photochemistry to multipurpose catalysis to sustainable chemistry, Angew. Chem. Int. Ed. 51 (2012) 68–89, http://dx.doi.org/10.1002/anie.201101182.
[102] M.N. Nadagouda, R.B. Nasir Baig, R.S. Varma, S. Verma, Magnetic Fe@g-C3N4. a photoactive catalyst for the hydrogenation of alkenes and alkynes, ACS Sustain. Chem. Eng. (2016), http://dx.doi.org/10.1021/acssuschemeng.5b01610.
[103] L. Song, S. Zhang, X. Wu, H. Tian, Q. Wei, Graphitic C3N4 photocatalyst for esterification of benzaldehyde and alcohol under visible light radiation, Ind. Eng. Chem. Res. 51 (2012) 9510–9514, http://dx.doi.org/10.1021/ie3010226.
[104] L. Zhang, D. Liu, J. Guan, X. Chen, X. Guo, F. Zhao, T. Hou, X. Mu, Metal-free g-C3N4 photocatalyst by sulfuric acid activation for selective aerobic oxidation of benzyl alcohol under visible light, Mater. Res. Bull. 59 (2014) 84–92, http://dx.doi.org/10.1016/j.materresbull.2014.06.021.
[105] G. SHIRAVAND, A. BADIEI, G.M. ZIARANI, M. JAFARABADI, M. HAMZEHLOO, Photocatalytic synthesis of phenol by direct hydroxylation of benzene by a modified nanoporous silica (LUS-1) under sunlight, Chin. J. Catal. 33 (2012) 1347–1353, http://dx.doi.org/10.1016/S1872-2067(11)60422-1.
[106] X. Ye, Y. Cui, X. Qiu, X. Wang, Selective oxidation of benzene to phenol by Fe-CN/TS-1 catalysts under visible light irradiation, Appl. Catal. B Environ. 152–153 (2014) 383–389, http://dx.doi.org/10.1016/j.apcatb.2014.01.050.
[107] X. Dai, M. Xie, S. Meng, X. Fu, S. Chen, Coupled systems for selective oxidation of aromatic alcohols to aldehydes and reduction of nitrobenzene into aniline using CdS/g-C3N4 photocatalyst under visible light irradiation, Appl. Catal. B Environ. 158–159 (2014) 382–390, http://dx.doi.org/10.1016/j.apcatb.2014.04.035.
[108] Y. Zhang, L. Hu, S. Zhao, N. Liu, L. Bai, J. Liu, H. Huang, Y. Liu, Z. Kang, Ag3PW12O40/C3N4 nanocomposites as an efficient photocatalyst for hydrocarbon selective oxidation, RSC Adv. 6 (2016) 60394–60399, http://dx.doi.org/10.1039/C6RA09235G.
[109] M.R. Hoffmann, S.T. Martin, W. Choi, D.W. Bahnemann, Environmental applications of semiconductor photocatalysis, Chem. Rev. 95 (1995) 69–96, http://dx.doi.org/10.1021/cr00033a004.
[110] P. Zhang, X. Li, C. Shao, Y. Liu, Hydrothermal synthesis of carbon-rich graphitic carbon nitride nanosheets for photoredox catalysis, J. Mater. Chem. A 3 (2015) 3281–3284, http://dx.doi.org/10.1039/C5TA00202H.

[111] S. Hu, L. Ma, Y. Xie, F. Li, Z. Fan, F. Wang, Q. Wang, Y. Wang, X. Kang, G. Wu, Hydrothermal synthesis of oxygen functionalized S–P codoped g-C3N4 nanorods with outstanding visible light activity under anoxic conditions, Dalton Trans. 44 (2015) 20889–20897, http://dx.doi.org/10.1039/C5DT04035C.

[112] X. Dang, X. Zhang, W. Zhang, X. Dong, G. Wang, C. Ma, X. Zhang, H. Ma, M. Xue, Ultra-thin C3N4 nanosheets for rapid charge transfer in the core–shell heterojunction of α-sulfur@C3N4 for superior metal-free photocatalysis under visible light, RSC Adv. 5 (2015) 15052–15058, http://dx.doi.org/10.1039/C4RA14623A.

[113] G. Liao, S. Chen, X. Quan, H. Yu, H. Zhao, Graphene oxide modified g-C3N4 hybrid with enhanced photocatalytic capability under visible light irradiation, J. Mater. Chem. 22 (2012) 2721–2726, http://dx.doi.org/10.1039/C1JM13490F.

[114] Y. Xu, H. Xu, L. Wang, J. Yan, H. Li, Y. Song, L. Huang, G. Cai, The CNT modified white C3N4 composite photocatalyst with enhanced visible-light response photoactivity, Dalton Trans. 42 (2013) 7604–7613, http://dx.doi.org/10.1039/C3DT32871F.

[115] X. Bai, L. Wang, Y. Wang, W. Yao, Y. Zhu, Enhanced oxidation ability of g-C3N4 photocatalyst via C60 modification, Appl. Catal. B Environ. 152–153 (2014) 262–270, http://dx.doi.org/10.1016/j.apcatb.2014.01.046.

[116] H. Sun, G. Zhou, Y. Wang, A. Suvorova, S. Wang, A new metal-free carbon hybrid for enhanced photocatalysis, ACS Appl. Mater. Interfaces 6 (2014) 16745–16754, http://dx.doi.org/10.1021/am503820h.

[117] F. Chang, J. Zhang, Y. Xie, J. Chen, C. Li, J. Wang, J. Luo, B. Deng, X. Hu, Fabrication, characterization, and photocatalytic performance of exfoliated g-C3N4–TiO2 hybrids, Appl. Surf. Sci. 311 (2014) 574–581, http://dx.doi.org/10.1016/j.apsusc.2014.05.111.

[118] H. Zhu, D. Chen, D. Yue, Z. Wang, H. Ding, In-situ synthesis of g-C3NTiO2 composite with enhanced visible light photoactivity, J. Nanoparticle Res. 16 (2632) (2014) 4–25, http://dx.doi.org/10.1007/s11051-014-2632-7.

[119] N. Boonprakob, N. Wetchakun, S. Phanichphant, D. Waxler, P. Sherrell, A. Nattestad, J. Chen, B. Inceesungvorn, Enhanced visible-light photocatalytic activity of g-C3N4/TiO2 films, J. Colloid Interface Sci. 417 (2014) 402–409, http://dx.doi.org/10.1016/j.jcis.2013.11.072.

[120] S. Ma, J. Xue, Y. Zhou, Z. Zhang, Z. Cai, D. Zhu, S. Liang, Facile fabrication of a mpg-C3N4/TiO2 heterojunction photocatalyst with enhanced visible light photoactivity toward organic pollutant degradation, RSC Adv. 5 (2015) 64976–64982, http://dx.doi.org/10.1039/C5RA10447E.

[121] J. Zhou, M. Zhang, Y. Zhu, Photocatalytic enhancement of hybrid C3N4/TiO2 prepared via ball milling method, Phys. Chem. Chem. Phys. 17 (2015) 3647–3652, http://dx.doi.org/10.1039/C4CP05173D.

[122] Y. Li, J. Wang, Y. Yang, Y. Zhang, D. He, Q. An, G. Cao, Seed-induced growing various TiO2 nanostructures on g-C3N4 nanosheets with much enhanced photocatalytic activity under visible light, J. Hazard. Mater. 292 (2015) 79–89, http://dx.doi.org/10.1016/j.jhazmat.2015.03.006.

[123] K. Li, S. Gao, Q. Wang, H. Xu, Z. Wang, B. Huang, Y. Dai, J. Lu, In-situ-reduced synthesis of Ti3+ self-doped TiO2/g-C3N4 heterojunctions with high photocatalytic performance under LED light irradiation, ACS Appl. Mater. Interfaces 7 (2015) 9023–9030, http://dx.doi.org/10.1021/am508505n.

[124] D. Lu, G. Zhang, Z. Wan, Visible-light-driven g-C3N4/Ti3+-TiO2 photocatalyst co-exposed {0 0 1} and {1 0 1} facets and its enhanced photocatalytic activities for organic pollutant degradation and Cr(VI) reduction, Appl. Surf. Sci. 358 (Part A) (2015) 223–230, http://dx.doi.org/10.1016/j.apsusc.2015.08.240.

[125] L. Gu, J. Wang, Z. Zou, X. Han, Graphitic-C3N4-hybridized TiO2 nanosheets with reactive {0 0 1} facets to enhance the UV- and visible-light photocatalytic activity, J. Hazard. Mater. 268 (2014) 216–223, http://dx.doi.org/10.1016/j.jhazmat.2014.01.021.

[126] X. Wang, W. Yang, F. Li, Y. Xue, R. Liu, Y. Hao, In situ microwave-assisted synthesis of porous N-TiO2/g-C3N4 heterojunctions with enhanced visible-light photocatalytic properties, Ind. Eng. Chem. Res. 52 (2013) 17140–17150, http://dx.doi.org/10.1021/ie402820v.

[127] W. Li, C. Li, B. Chen, X. Jiao, D. Chen, Facile synthesis of sheet-like N–TiO2/g-C3N4 heterojunctions with highly enhanced and stable visible-light photocatalytic activities, RSC Adv. 5 (2015) 34281–34291, http://dx.doi.org/10.1039/C5RA04100G.

[128] S. Sun, M. Sun, Y. Fang, Y. Wang, H. Wang, One-step in situ calcination synthesis of g-C3N4/N-TiO2 hybrids with enhanced photoactivity, RSC Adv. 6 (2016) 13063–13071, http://dx.doi.org/10.1039/C5RA26700E.

[129] S. Kumar, S. Tonda, A. Baruah, B. Kumar, V. Shanker, Synthesis of novel and stable g-C3N4/N-doped SrTiO3 hybrid nanocomposites with improved photocurrent and photocatalytic activity under visible light irradiation, Dalton Trans. 43 (2014) 16105–16114, http://dx.doi.org/10.1039/C5RA26700E.

[130] Q. Liu, C. Fan, H. Tang, X. Sun, J. Yang, X. Cheng, One-pot synthesis of g-C3N4/V2O5 composites for visible light-driven photocatalytic activity, Appl. Surf. Sci. 358 (Part A) (2015) 188–195, http://dx.doi.org/10.1016/j.apsusc.2015.09.010.

[131] S. Kumar, B. Kumar, T. Surendar, V. Shanker, g-C3N4/NaTaO3 organic–inorganic hybrid nanocomposite: high-performance and recyclable visible light driven photocatalyst, Mater. Res. Bull. 49 (2014) 310–318, http://dx.doi.org/10.1016/j.materresbull.2013.09.013.

[132] Z. Yong, J. Ren, H. Hu, P. Li, S. Ouyang, H. Xu, D. Wang, Synthesis, characterization, and photocatalytic activity of g-C3N4/KTaO3 composites under visible light irradiation, J. Nanomater. 2015 (2015) e821986, http://dx.doi.org/10.1155/2015/821986.

[133] W. Peng, X. Li, Synthesis of MoS2/g-C3N4 as a solar light-responsive photocatalyst for organic degradation, Catal. Commun. 49 (2014) 63–67, http://dx.doi.org/10.1016/j.catcom.2014.02.008.

[134] Q. Li, N. Zhang, Y. Yang, G. Wang, D.H.L. Ng, High efficiency photocatalysis for pollutant degradation with MoS2/C3N4 heterostructures, Langmuir 30 (2014) 8965–8972, http://dx.doi.org/10.1021/la502033t.

[135] H. Li, J. Liu, W. Hou, N. Du, R. Zhang, X. Tao, Synthesis and characterization of g-C3N4/Bi2MoO6 heterojunctions with enhanced visible light photocatalytic activity, Appl. Catal. B Environ. 160–161 (2014) 89–97, http://dx.doi.org/10.1016/j.apcatb.2014.05.019.

[136] Y. Tian, F. Cheng, X. Zhang, F. Yan, B. Zhou, Z. Chen, J. Liu, F. Xi, X. Dong, Solvothermal synthesis and enhanced visible light photocatalytic activity of novel graphitic carbon nitride–Bi2MoO6 heterojunctions, Powder Technol. 267 (2014) 126–133, http://dx.doi.org/10.1016/j.powtec.2014.07.021.

[137] S.W. Hu, L.W. Yang, Y. Tian, X.L. Wei, J.W. Ding, J.X. Zhong, P.K. Chu, Non-covalent doping of graphitic carbon nitride with ultrathin graphene oxide and molybdenum disulfide nanosheets: an effective binary heterojunction photocatalyst under visible light irradiation, J. Colloid Interface Sci. 431 (2014) 42–49, http://dx.doi.org/10.1016/j.jcis.2014.05.023.

[138] L. Huang, H. Xu, Y. Li, H. Li, X. Cheng, J. Xia, Y. Xu, G. Cai, Visible-light-induced WO3/g-C3N4 composites with enhanced photocatalytic activity, Dalton Trans. 42 (2013) 8606–8616, http://dx.doi.org/10.1039/C3DT00115F.

[139] K. Katsumata, R. Motoyoshi, N. Matsushita, K. Okada, Preparation of graphitic carbon nitride (g-C3N4)/WO3 composites and enhanced visible-light-driven photodegradation of acetaldehyde gas, J. Hazard. Mater. 260 (2013) 475–482, http://dx.doi.org/10.1016/j.jhazmat.2013.05.058.

[140] S. Chen, Y. Hu, X. Jiang, S. Meng, X. Fu, Fabrication and characterization of novel Z-scheme photocatalyst WO3/g-C3N4 with high efficient visible light photocatalytic activity, Mater. Chem. Phys. 149–150 (2015) 512–521, http://dx.doi.org/10.1016/j.matchemphys.2014.11.001.

[141] Y. Wang, Z. Wang, S. Muhammad, J. He, Graphite-like C3N4 hybridized ZnWO4 nanorods: synthesis and its enhanced photocatalysis in visible light, CrystEngComm 14 (2012) 5065–5070, http://dx.doi.org/10.1039/C2CE25517K.

[142] S. Zhan, F. Zhou, N. Huang, Y. Yang, Y. Liu, Y. Yin, Y. Fang, g-C3N4/ZnWO4 films: preparation and its enhanced photocatalytic decomposition of phenol in UV, Appl. Surf. Sci. 358 (Part A) (2015) 328–335, http://dx.doi.org/10.1016/j.apsusc.2015.07.180.

[143] N. Tian, H. Huang, Y. Zhang, Mixed-calcination synthesis of CdWO4/g-C3N4 heterojunction with enhanced visible-light-driven photocatalytic activity, Appl. Surf. Sci. 358 (Part A) (2015) 343–349, http://dx.doi.org/10.1016/j.apsusc.2015.07.154.

[144] K. Vignesh, A. Suganthi, B.-K. Min, M. Kang, Photocatalytic activity of magnetically recoverable MnFe2O4/g-C3N4/TiO2 nanocomposite under simulated solar light irradiation, J. Mol. Catal. Chem. 395 (2014) 373–383, http://dx.doi.org/10.1016/j.molcata.2014.08.040.

[145] Z. Zhu, Z. Lu, X. Zhao, Y. Yan, W. Shi, D. Wang, L. Yang, X. Lin, Z. Hua, Y. Liu, Surface imprinting of a g-C3N4 photocatalyst for enhanced photocatalytic activity and selectivity towards photodegradation of 2-mercaptobenzothiazole, RSC Adv. 5 (2015) 40726–40736, http://dx.doi.org/10.1039/C5RA06209H.

[146] Q. Liu, Y. Guo, Z. Chen, Z. Zhang, X. Fang, Constructing a novel ternary Fe(III)/graphene/g-C3N4 composite photocatalyst with enhanced visible-light driven photocatalytic activity via interfacial charge transfer effect, Appl. Catal. B Environ. 183 (2016) 231–241, http://dx.doi.org/10.1016/j.apcatb.2015.10.054.

[147] Y. Yao, F. Lu, Y. Zhu, F. Wei, X. Liu, C. Lian, S. Wang, Magnetic core–shell CuFe2O4@C3N4 hybrids for visible light photocatalysis of Orange II, J. Hazard. Mater. 297 (2015) 224–233, http://dx.doi.org/10.1016/j.jhazmat.2015.04.046.

[148] S. Zhang, J. Li, M. Zeng, G. Zhao, J. Xu, W. Hu, X. Wang, In situ synthesis of water-soluble magnetic graphitic carbon nitride photocatalyst and its synergistic catalytic performance, ACS Appl. Mater. Interfaces 5 (2013) 12735–12743, http://dx.doi.org/10.1021/am404123z.

[149] D. Chen, K. Wang, T. Ren, H. Ding, Y. Zhu, Synthesis and characterization of the ZnO/mpg-C3N4 heterojunction photocatalyst with enhanced visible light photoactivity, Dalton Trans. 43 (2014) 13105–13114, http://dx.doi.org/10.1039/C4DT01347F.

[150] K. Vignesh, S. Kang, B.S. Kwak, M. Kang, Meso-porous ZnO nano-triangles @ graphitic-C3N4 nano-foils: fabrication and Recyclable photocatalytic activity, Sep. Purif. Technol. 147 (2015) 257–265, http://dx.doi.org/10.1016/j.seppur.2015.04.043.

[151] L. Zhang, X. Wang, Q. Nong, H. Lin, B. Teng, Y. Zhang, L. Zhao, T. Wu, Y. He, Enhanced visible-light photoactivity of g-C3N4 via Zn2SnO4 modification, Appl. Surf. Sci. 329 (2015) 143–149, http://dx.doi.org/10.1016/j.apsusc.2014.12.154.

[152] W.-K. Jo, N. Clament Sagaya Selvam, Enhanced visible light-driven photocatalytic performance of ZnO–g-C3N4 coupled with graphene oxide as a novel ternary nanocomposite, J. Hazard. Mater. 299 (2015) 462–470, http://dx.doi.org/10.1016/j.jhazmat.2015.07.042.

[153] J. Fu, B. Chang, Y. Tian, F. Xi, X. Dong, Novel C3N4–CdS composite photocatalysts with organic–inorganic heterojunctions: in situ synthesis, exceptional activity, high stability and photocatalytic mechanism, J. Mater. Chem. A 1 (2013) 3083–3090, http://dx.doi.org/10.1039/C2TA00672C.

[154] X. Cui, Y.F. Zheng, H.Y. Yin, X.C. Song, Novel C3N4/Zn1-xCdxS heterostructures with adjustment of the band gap and their visible light photocatalytic properties, Phys. Chem. Chem. Phys. 17 (2015) 29354–29362, http://dx.doi.org/10.1039/C5CP05464H.
[155] W. Tian, N. Li, J. Zhou, A novel P-doped g-C3N4/Zn0.8Cd0.2S composite photocatalyst for degradation of methylene blue under simulated sunlight, Appl. Surf. Sci. 361 (2016) 251–258, http://dx.doi.org/10.1016/j.apsusc.2015.11.157.
[156] R.C. Pawar, V. Khare, C.S. Lee, Hybrid photocatalysts using graphitic carbon nitride/cadmium sulfide/reduced graphene oxide (g-C3N4/CdS/RGO) for superior photodegradation of organic pollutants under UV and visible light, Dalton Trans. 43 (2014) 12514–12527, http://dx.doi.org/10.1039/C4DT01278J.
[157] L. Ge, C. Han, J. Liu, Novel visible light-induced g-C3N4/Bi2WO6 composite photocatalysts for efficient degradation of methyl orange, Appl. Catal. B Environ. 108–109 (2011) 100–107, http://dx.doi.org/10.1016/j.apcatb.2011.08.014.
[158] L. Liu, Y. Qi, J. Lu, S. Lin, W. An, J. Hu, Y. Liang, W. Cui, Dramatic activity of a Bi2WO6@g-C3N4 photocatalyst with a core@shell structure, RSC Adv. 5 (2015) 99339–99346, http://dx.doi.org/10.1039/C5RA19929H.
[159] C. Pan, J. Xu, Y. Wang, D. Li, Y. Zhu, Dramatic activity of C3N4/BiPO4 photocatalyst with core/shell structure formed by self-assembly, Adv. Funct. Mater. 22 (2012) 1518–1524, http://dx.doi.org/10.1002/adfm.201102306.
[160] S. Obregón, Y. Zhang, G. Colón, Cascade charge separation mechanism by ternary heterostructured BiPO4/TiO2/g-C3N4 photocatalyst, Appl. Catal. B Environ. 184 (2016) 96–103, http://dx.doi.org/10.1016/j.apcatb.2015.11.027.
[161] Z. Yang, J. Li, F. Cheng, Z. Chen, X. Dong, BiOBr/protonated graphitic C3N4 heterojunctions: intimate interfaces by electrostatic interaction and enhanced photocatalytic activity, J. Alloys Compd. 634 (2015) 215–222, http://dx.doi.org/10.1016/j.jallcom.2015.02.103.
[162] J. Xia, M. Ji, J. Di, B. Wang, S. Yin, Q. Zhang, M. He, H. Li, Construction of ultrathin C3N4/Bi4O5I2 layered nanojunctions via ionic liquid with enhanced photocatalytic performance and mechanism insight, Appl. Catal. B Environ. 191 (2016) 235–245, http://dx.doi.org/10.1016/j.apcatb.2016.02.058.
[163] D. Yuan, L. Huang, Y. Li, Y. Xu, H. Xu, S. Huang, J. Yan, M. He, H. Li, Synthesis and photocatalytic activity of g-C3N4/BiOI/BiOBr ternary composites, RSC Adv. 6 (2016) 41204–41213, http://dx.doi.org/10.1039/C6RA05565F.
[164] R. Yin, Q. Luo, D. Wang, H. Sun, Y. Li, X. Li, J. An, SnO2/g-C3N4 photocatalyst with enhanced visible-light photocatalytic activity, J. Mater. Sci. 49 (2014) 6067–6073, http://dx.doi.org/10.1007/s10853-014-8330-0.
[165] X. Chen, B. Zhou, S. Yang, H. Wu, Y. Wu, L. Wu, J. Pan, X. Xiong, In situ construction of an SnO2/g-C3N4 heterojunction for enhanced visible-light photocatalytic activity, RSC Adv. 5 (2015) 68953–68963, http://dx.doi.org/10.1039/C5RA11801H.
[166] C. Xing, Z. Wu, D. Jiang, M. Chen, Hydrothermal synthesis of In2S3/g-C3N4 heterojunctions with enhanced photocatalytic activity, J. Colloid Interface Sci. 433 (2014) 9–15, http://dx.doi.org/10.1016/j.jcis.2014.07.015.
[167] F. Li, Y. Zhao, Q. Wang, X. Wang, Y. Hao, R. Liu, D. Zhao, Enhanced visible-light photocatalytic activity of active Al2O3/g-C3N4 heterojunctions synthesized via surface hydroxyl modification, J. Hazard. Mater. 283 (2015) 371–381, http://dx.doi.org/10.1016/j.jhazmat.2014.09.035.
[168] X. Wang, S. Wang, W. Hu, J. Cai, L. Zhang, L. Dong, L. Zhao, Y. He, Synthesis and photocatalytic activity of SiO2/g-C3N4 composite photocatalyst, Mater. Lett. 115 (2014) 53–56, http://dx.doi.org/10.1016/j.matlet.2013.10.016.
[169] B. Lin, C. Xue, X. Yan, G. Yang, G. Yang, B. Yang, Facile fabrication of novel SiO2/g-C3N4 core–shell nanosphere photocatalysts with enhanced visible light activity, Appl. Surf. Sci. 357 (Part A) (2015) 346–355, http://dx.doi.org/10.1016/j.apsusc.2015.09.041.
[170] C. Wen, H. Zhang, Q. Bo, T. Huang, Z. Lu, J. Lv, Y. Wang, Facile synthesis organic–inorganic heterojunctions of HSbO3/g-C3N4 as efficient visible-light-driven photocatalyst for organic degradation, Chem. Eng. J. 270 (2015) 405–410, http://dx.doi.org/10.1016/j.cej.2015.01.082.
[171] H. Wang, X. Yuan, H. Wang, X. Chen, Z. Wu, L. Jiang, W. Xiong, G. Zeng, Facile synthesis of Sb2S3/ultrathin g-C3N4 sheets heterostructures embedded with g-C3N4 quantum dots with enhanced NIR-light photocatalytic performance, Appl. Catal. B Environ. 193 (2016) 36–46, http://dx.doi.org/10.1016/j.apcatb.2016.03.075.
[172] J. Luo, X. Zhou, L. Ma, X. Xu, Enhancing visible-light photocatalytic activity of g-C3N4 by doping phosphorus and coupling with CeO2 for the degradation of methyl orange under visible light irradiation, RSC Adv. 5 (2015) 68728–68735, http://dx.doi.org/10.1039/C5RA10848A.
[173] L. Wang, J. Ding, Y. Chai, Q. Liu, J. Ren, X. Liu, W.-L. Dai, CeO2 nanorod/g-C3N4/N-rGO composite: enhanced visible-light-driven photocatalytic performance and the role of N-rGO as electronic transfer media, Dalton Trans. 44 (2015) 11223–11234, http://dx.doi.org/10.1039/C5DT01479D.
[174] X. She, H. Xu, H. Wang, J. Xia, Y. Song, J. Yan, Y. Xu, Q. Zhang, D. Du, H. Li, Controllable synthesis of CeO2/g-C3N4 composites and their applications in the environment, Dalton Trans. 44 (2015) 7021–7031, http://dx.doi.org/10.1039/C4DT03793F.
[175] Y. He, J. Cai, T. Li, Y. Wu, Y. Yi, M. Luo, L. Zhao, Synthesis, characterization, and activity evaluation of DyVO4/g-C3N4 composites under visible-light irradiation, Ind. Eng. Chem. Res. 51 (2012) 14729–14737, http://dx.doi.org/10.1021/ie301774e.
[176] T. Li, L. Zhao, Y. He, J. Cai, M. Luo, J. Lin, Synthesis of g-C3N4/SmVO4 composite photocatalyst with improved visible light photocatalytic activities in RhB degradation, Appl. Catal. B Environ. 129 (2013) 255–263, http://dx.doi.org/10.1016/j.apcatb.2012.09.031.
[177] Y. He, J. Cai, L. Zhang, X. Wang, H. Lin, B. Teng, L. Zhao, W. Weng, H. Wan, M. Fan, Comparing two new composite photocatalysts, t-LaVO4/g-C3N4 and m-LaVO4/g-C3N4, for their structures and performances, Ind. Eng. Chem. Res. 53 (2014) 5905–5915, http://dx.doi.org/10.1021/ie4043856.
[178] Y. He, J. Cai, T. Li, Y. Wu, H. Lin, L. Zhao, M. Luo, Efficient degradation of RhB over GdVO4/g-C3N4 composites under visible-light irradiation, Chem. Eng. J. 215–216 (2013) 721–730, http://dx.doi.org/10.1016/j.cej.2012.11.074.
[179] W. Wang, J.C. Yu, D. Xia, P.K. Wong, Y. Li, Graphene and g-C3N4 nanosheets cowrapped elemental α-sulfur as a novel metal-free heterojunction photocatalyst for bacterial inactivation under visible-light, Environ. Sci. Technol. 47 (2013) 8724–8732, http://dx.doi.org/10.1021/es4013504.
[180] H. Zhao, S. Chen, X. Quan, H. Yu, H. Zhao, Integration of microfiltration and visible-light-driven photocatalysis on g-C3N4 nanosheet/reduced graphene oxide membrane for enhanced water treatment, Appl. Catal. B Environ. 194 (2016) 134–140, http://dx.doi.org/10.1016/j.apcatb.2016.04.042.
[181] J.H. Thurston, N.M. Hunter, K.A. Cornell, Preparation and characterization of photoactive antimicrobial graphitic carbon nitride (g-C3N4) films, RSC Adv. 6 (2016) 42240–42248, http://dx.doi.org/10.1039/C6RA05613J.
[182] F. Dong, Z. Wang, Y. Sun, W.-K. Ho, H. Zhang, Engineering the nanoarchitecture and texture of polymeric carbon nitride semiconductor for enhanced visible light photocatalytic activity, J. Colloid Interface Sci. 401 (2013) 70–79, http://dx.doi.org/10.1016/j.jcis.2013.03.034.
[183] F. Dong, Z. Ni, P. Li, Z. Wu, A general method for type I and type II g-C3N4/g-C3N4 metal-free isotype heterostructures with enhanced visible light photocatalysis, New J. Chem. 39 (2015) 4737–4744, http://dx.doi.org/10.1039/C5NJ00351B.
[184] F. Dong, M. Ou, Y. Jiang, S. Guo, Z. Wu, Efficient and durable visible light photocatalytic performance of porous carbon nitride nanosheets for air purification, Ind. Eng. Chem. Res. 53 (2014) 2318–2330, http://dx.doi.org/10.1021/ie4038104.
[185] F. Dong, Y. Li, Z. Wang, W.-K. Ho, Enhanced visible light photocatalytic activity and oxidation ability of porous graphene-like g-C3N4 nanosheets via thermal exfoliation, Appl. Surf. Sci. 358 (Part A) (2015) 393–403, http://dx.doi.org/10.1016/j.apsusc.2015.04.034.
[186] Z. Zhao, Y. Sun, Q. Luo, F. Dong, H. Li, W.-K. Ho, Mass-controlled direct synthesis of graphene-like carbon nitride nanosheets with exceptional high visible light activity. less is better, Sci. Rep. 5 (2015) 14643, http://dx.doi.org/10.1038/srep14643.
[187] Z. Wang, W. Guan, Y. Sun, F. Dong, Y. Zhou, W.-K. Ho, Water-assisted production of honeycomb-like g-C3N4 with ultralong carrier lifetime and outstanding photocatalytic activity, Nanoscale 7 (2015) 2471–2479, http://dx.doi.org/10.1039/C4NR05732E.
[188] W. Ho, Z. Zhang, W. Lin, S. Huang, X. Zhang, X. Wang, Y. Huang, Copolymerization with 2,4 6-triaminopyrimidine for the rolling-up the layer structure, tunable electronic properties, and photocatalysis of g-C3N4, ACS Appl. Mater. Interfaces 7 (2015) 5497–5505, http://dx.doi.org/10.1021/am509213x.
[189] Z. Zhao, Y. Sun, F. Dong, Y. Zhang, H. Zhao, Template synthesis of carbon self-doped g-C3N4 with enhanced visible to near-infrared absorption and photocatalytic performance, RSC Adv. 5 (2015) 39549–39556, http://dx.doi.org/10.1039/C5RA03433G.
[190] F. Dong, Z. Wang, Y. Li, W.-K. Ho, S.C. Lee, Immobilization of polymeric g-C3N4 on structured ceramic foam for efficient visible light photocatalytic air purification with real indoor illumination, Environ. Sci. Technol. 48 (2014) 10345–10353, http://dx.doi.org/10.1021/es502290f.
[191] F. Dong, Z. Zhao, T. Xiong, Z. Ni, W. Zhang, Y. Sun, W.-K. Ho, In situ construction of g-C3N4/g-C3N4 metal-free heterojunction for enhanced visible-light photocatalysis, ACS Appl. Mater. Interfaces. 5 (2013) 11392–11401, http://dx.doi.org/10.1021/am403653a.
[192] W. Liu, M. Wang, C. Xu, S. Chen, Facile synthesis of g-C3N4/ZnO composite with enhanced visible light photooxidation and photoreduction properties, Chem. Eng. J. 209 (2012) 386–393, http://dx.doi.org/10.1016/j.cej.2012.08.033.
[193] M. Sun, Q. Yan, T. Yan, M. Li, D. Wei, Z. Wang, Q. Wei, B. Du, Facile fabrication of 3D flower-like heterostructured g-C3N4/SnS2 composite with efficient photocatalytic activity under visible light, RSC Adv. 4 (2014) 31019–31027, http://dx.doi.org/10.1039/C4RA03843F.
[194] M. Sun, T. Yan, Q. Yan, H. Liu, L. Yan, Y. Zhang, B. Du, Novel visible-light driven g-C3N4/Zn0.25Cd0.75S composite photocatalyst for efficient degradation of dyes and reduction of Cr(VI) in water, RSC Adv. 4 (2014) 19980–19986, http://dx.doi.org/10.1039/C4RA01439A.
[195] Y. Zang, L. Li, Y. Xu, Y. Zuo, G. Li, Hybridization of brookite TiO2 with g-C3N4: a visible-light-driven photocatalyst for As3+ oxidation, MO degradation and water splitting for hydrogen evolution, J. Mater. Chem. A 2 (2014) 15774–15780, http://dx.doi.org/10.1039/C4TA02082K.
[196] C. Lu, R. Chen, X. Wu, M. Fan, Y. Liu, Z. Le, S. Jiang, S. Song, Boron doped g-C3N4 with enhanced photocatalytic UO22+ reduction performance, Appl. Surf. Sci. 360 (Part B) (2016) 1016–1022, http://dx.doi.org/10.1016/j.apsusc.2015.11.112.
[197] D. Wang, Y. Zhang, W. Chen, A novel nickel–thiourea–triethylamine complex adsorbed on graphitic C_3N_4 for low-cost solar hydrogen production, Chem. Commun. 50 (2014) 1754–1756, http://dx.doi.org/10.1039/c3cc48141g.